



UNIVERSIDAD DE INVESTIGACIÓN DE TECNOLOGÍA EXPERIMENTAL YACHAY

Escuela de Ciencias Químicas e Ingeniería

ENHANCING ROBOTIC ARTIFICIAL MUSCLE FUNCTIONALITY: EXPLORING PIEZOELECTRIC PROPERTIES OF COORDINATION POLYMERS

Trabajo de integración curricular presentado como requisito para la obtención del título de Magister en Ciencias Químicas con mención en Ciencia e Ingeniería de los Materiales.

Autor:

Alvarez Romero Jeffrey Ludovic

Tutor:

Ávila Sosa Edward Ebner, PhD.

Co-Tutor:

Saucedo Juan Pablo, PhD.

Urcuquí, Septiembre 2024

Anexo 2 – Autoría

AUTORÍA

Yo, **Jeffrey Ludovic Alvarez Romero**, con cédula de identidad **0402037808**, declaro que las ideas, juicios, valoraciones, interpretaciones, consultas bibliográficas, definiciones y conceptualizaciones expuestas en el presente trabajo; así cómo, los procedimientos y herramientas utilizadas en la investigación, son de absoluta responsabilidad de el/la autora (a) del trabajo de integración curricular. Así mismo, me acojo a los reglamentos internos de la Universidad de Investigación de Tecnología Experimental Yachay.

Urququí, Julio 2024.

Jeffrey Ludovic Alvarez Romero
CI: 0402037808

Anexo 3 – Autorización de Publicación

AUTORIZACIÓN DE PUBLICACIÓN

Yo, **Jeffrey Ludovic Alvarez Romero**, con cédula de identidad **0402037808**, cedo a la Universidad de Investigación de Tecnología Experimental Yachay, los derechos de publicación de la presente obra, sin que deba haber un reconocimiento económico por este concepto. Declaro además que el texto del presente trabajo de titulación no podrá ser cedido a ninguna empresa editorial para su publicación u otros fines, sin contar previamente con la autorización escrita de la Universidad.

Asimismo, autorizo a la Universidad que realice la digitalización y publicación de este trabajo de integración curricular en el repositorio virtual, de conformidad a lo dispuesto en el Art. 144 de la Ley Orgánica de Educación Superior

Urcuquí, Julio 2024.

Jeffrey Ludovic Alvarez Romero
CI: 0402037808

Acknowledgments

I would like to express my deepest gratitude to my tutors, Dr. Edward E. Avila and Dr. Juan Pablo Saucedo, for their unwavering support and guidance throughout my studies. Their mentorship has been pivotal in my academic development.

Additionally, I am especially thankful to Yachay Tech University for awarding me a scholarship in recognition of my academic excellence. This scholarship has been instrumental in supporting my studies and enabling me to focus on my research and academic pursuits without financial burden.

Jeffrey L. Alvarez

Resumen

Los avances en las tecnologías prostéticas han llevado a mejoras significativas en la funcionalidad, pero aún persisten desafíos en términos de resistencia, adaptabilidad y mecanismos de actuación. Los enfoques tradicionales, a menudo dependientes de circuitos electrónicos y motores, luchan por replicar la flexibilidad y eficiencia de los sistemas biológicos. En respuesta, los investigadores se han dirigido a sistemas musculoesqueléticos inspirados biológicamente que incorporan materiales avanzados como polímeros con memoria de forma, aleaciones y materiales piezoeléctricos. Los materiales piezoeléctricos son especialmente prometedores debido a su alta eficiencia y ancho de banda, pero su aplicación ha estado limitada por bajas deformaciones de actuación. Mientras que se ha prestado mucha atención a las piezocerámicas bien establecidas, otras clases de materiales piezoeléctricos, como los polímeros, están ganando reconocimiento por su mayor flexibilidad mecánica y su potencial para un rendimiento mejorado en la actuación. Entre estos, los polímeros de coordinación representan una categoría nueva y prometedora. Este estudio investiga el potencial de los polímeros de coordinación como una solución, que combinan coeficientes piezoeléctricos mejorados con flexibilidad mecánica. Estos polímeros se sintetizaron utilizando nitrato de zinc, 2-metilimidazol y ácido cinámico, seguido de la integración en una matriz de ácido poliláctico. La caracterización estructural confirmó la coordinación bidentada del ácido cinámico, con la difracción de rayos X indexando las muestras en los grupos espaciales no centro simétricos C2 y P2₁, esenciales para el comportamiento piezoeléctrico. Se evaluó el sistema de medición piezoeléctrica, encontrando un valor de referencia de 15.70 μCN^{-1} para una muestra de PZT, lo que subrayó la importancia de la calibración del sistema. A pesar de las prometedoras propiedades estructurales, los compuestos que contenían un 0.5 % en peso de los polímeros de coordinación sintetizados no mostraron ningún efecto piezoeléctrico medible bajo fuerzas aplicadas de hasta 200 N. Estos hallazgos destacan la necesidad de investigar más a fondo el comportamiento piezoeléctrico del material y los factores que pueden estar inhibiendo su rendimiento en aplicaciones prácticas.

Palabras clave: sistemas musculoesqueléticos robóticos, músculos artificiales robóticos, material piezoeléctrico, polímero de coordinación, materiales biomiméticos, ingeniería de materiales.

Abstract

Advancements in prosthetic technologies have led to significant improvements in functionality, but challenges in strength, adaptability, and actuation mechanisms still persist. Traditional approaches, often reliant on electronic circuits and motors, struggle to replicate the flexibility and efficiency of biological systems. In response, researchers have turned to biologically inspired musculoskeletal systems that incorporate advanced materials such as shape memory polymers, alloys, and piezoelectric materials. Piezoelectric materials are particularly promising due to their high efficiency and bandwidth, but their application has been limited by low actuation strains. While much attention has been given to well-established piezoceramics, other classes of piezoelectric materials, like polymers, are gaining recognition for their improved mechanical flexibility and potential for enhanced actuation performance. Among these, coordination polymers represent a new and promising category. This study investigates the potential of coordination polymers as a solution, which combine enhanced piezoelectric coefficients with mechanical flexibility. These polymers were synthesized using zinc nitrate, 2-methylimidazole, and cinnamic acid, followed by integration into a polylactic acid matrix. Structural characterization confirmed the bidentate coordination of cinnamic acid, with X-ray diffraction indexing the samples in the non-centrosymmetric $C2$ and $P2_1$ space groups, essential for piezoelectric behavior. The piezoelectric measurement system was evaluated, finding a reference value of $15.70 \mu\text{CN}^{-1}$ for a PZT sample, which underscored the importance of system calibration. Despite the promising structural properties, composites containing 0.5 wt.% of the synthesized coordination polymers showed no measurable piezoelectric effect under applied forces up to 200 N. These findings highlight the need for further investigation into the material's piezoelectric behavior and the factors that may be inhibiting their performance in practical applications.

Key words: robotic musculoskeletal systems, robotic artificial muscles, piezoelectric material, coordination polymer, biomimetic materials, material engineering.

Table of Contents

Chapter 1: Introduction	12
1.1 Background.....	12
1.2 Problem Statement.....	13
1.3 General Objective	14
1.4 Specific Objectives	15
Chapter 2: Literature Review	16
2.1 Robotic Artificial Muscles	16
2.2 Piezoelectric <i>Materials</i>	19
2.2.1 Piezoelectric Ceramics.....	19
2.2.2 Piezoelectric Polymers.....	22
2.2.3 Piezoelectric Composites	25
2.2.4 Piezoelectric Coordination Polymers	29
2.3 Comparative Analysis	30
Chapter 3: Materials and Methodology	34
3.1 Coordination Polymer Synthesis	34
3.1.1 Reagents and Materials	34
3.1.2 Synthesis Procedure.....	35
3.1.3 Characterization.....	36
3.2 Composite Formation.....	38
3.2.1 Composite Samples	38
3.2.2 Characterization.....	40
Chapter 4: Results and Discussion	43
4.1 Coordination Polymer Synthesis	43
4.1.1 Initial Synthesis and Characterization of Coordination Polymers	43
4.1.2 Individual Coordination of Cinnamic Acid and 2-Methylimidazole	44
4.1.3 pH Effects on Ligand Coordination	48
4.1.4 Infrared Spectroscopic Analysis of CP-020	49
4.1.5 Crystallographic Analysis of Sample CP-020 & CP-028	51
4.2 Composite Formation.....	54
4.2.1 Evaluation of Piezoelectric Measurement System	54
4.2.2 Piezoelectric Property Measurement of Composite Samples	57
Chapter 5: Conclusion.....	58
5.1 Findings Summary	58
5.2 Limitations	58
5.3 Future Research Directions	59
References.....	60

List of Figures

Figure 1. Various types of prosthetic hands. (a) The latest advanced prosthetic hand, capable of replicating complex arm movements using electromagnetic actuators and sophisticated mechanisms. Despite technological advancements, it lacks the adaptability of natural limbs. (b) A conceptual future perspective of a prosthetic hand equipped with robotic artificial muscles that aim to emulate the flexibility and contraction strength of real skeletal muscles, potentially replicating the intricate motions of natural limbs.13

Figure 2. Categories of piezoelectric materials. This image illustrates three distinct categories of piezoelectric materials. (a) Ceramics feature a crystalline structure composed of metallic and non-metallic elements bonded through strong ionic or covalent interactions. (b) Polymers consist of large molecules formed from repeating monomeric units linked by covalent bonds, creating chains or networks. (c) Composites merge organic polymers with ceramics, combining the structural benefits of both materials.20

Figure 3. One-dimensional coordination polymer based on zinc and phthalic acid⁵². This diagram illustrates a one-dimensional coordination polymer formed by zinc ions and phthalic acid ligands. The Zinc ions (shown as blue spheres) are coordinated by the carboxylate groups of the phthalic acid molecules (depicted as red and grey sticks for oxygen and carbon, respectively), resulting in a chain-like structure. This polymer exemplifies the assembly of metal-organic frameworks through coordination bonds, highlighting the potential for creating extended networks with diverse functionalities.29

Figure 4. Comparative analysis of Young's modulus (MPa) and piezoelectric coefficient (pC/N) for ceramic (red), polymer (green), and composite (blue) piezoelectric materials, with density plots illustrating distribution trends.31

Figure 5. Logarithmic scale comparison of actuation strain, tensile strain, elastic compliance, tensile strength, piezoelectric coefficient, and dielectric constant for ceramic (red), polymer (green), and composite (blue) piezoelectric materials.32

Figure 6. Chemical structures of the ligands (a) cinnamic acid, an organic compound with a phenyl group attached to a three-carbon chain terminating in a carboxylic acid, (b) 2-methylimidazole, a heterocyclic aromatic organic compound with a methyl group at the second position of the imidazole ring, and (c) imidazole, a simple heterocycle with two nitrogen atoms. (d) The proposed coordination polymer, which possesses a non-centrosymmetric structure.35

Figure 7. Chemical structures and coordination polymers involving zinc ions with various ligands: (a) Coordination complex featuring 2-methylimidazole ligands and zinc ions, including uncoordinated 2-methylimidazole molecules, adapted from Chen et al.⁵⁷ (b) Coordination compound with 2-methylimidazole ligands bridging zinc ions, adapted from Fujie et al.⁵⁸ (c) Coordination structure involving imidazole and zinc ions, adapted from Demir et al.⁵⁹, and (d) Coordination structure incorporating cinnamic acid ligands and zinc ions, adapted from Zelenak et al.⁶⁰.36

Figure 8. The basic protocol for synthesizing the coordination polymer involves the following steps: (1) Dissolving each reagent in the solvent in separate beakers, (2) Combining the solutions into a single beaker, (3) Mixing and stirring the combined solution for approximately 30 minutes on a magnetic stirrer, and (4) Using vacuum filtration to collect the resulting precipitate.37

Figure 9. Sequential stages of solvent evaporation: (a) Solution before evaporation, (b) Solution with solvent partially evaporated, and (c) Completely evaporated solvent, resulting in the final solid product.....38

Figure 10. These steps illustrate the process sequence: polymer pellets are added initially, followed by dissolution of the polymer. Subsequently, coordination polymer is introduced, and finally, solvent evaporation completes the processing.39

Figure 11. Overview of the experimental setup: (a) A press with heating plates used for the composite material processing. (b) The system employed to measure piezoelectric properties, comprising a data acquisition system, a charge amplifier, and a universal testing machine. (c) A close-up view of the piezoelectric material within the setup.39

Figure 12. Comparison of materials: (a) The processed PLA blank sample. (b) The composite material containing 5 wt.% of the coordination polymer.40

Figure 13. Overview of the setup: (a) NI MyDAQ data acquisition system by National Instruments. (b) MyDAQ Express interface used for controlling the DAQ.....40

Figure 14. Illustration of the experimental setup: (a) Schematic representation of the electronic circuit used for measurements, illustrating the actual circuit configuration. (b) Representation of the charge amplifier circuit used in the measurements.41

Figure 15. Overview of the experimental process: (a) Graphical representation of the electrode setup. (b) Application of Mechanic brand silver conductive paint. (c) PLA blank sample with applied electrodes. (d) Composite film with applied electrodes.42

Figure 16. Molecular structure of *cis*-diaqua-bis(*trans*-cinnamato-O,O')-zinc(II)⁶⁵43

Figure 17. X-ray diffraction pattern of samples CP-005 (red) and CP-003 (black), showing similar peak patterns.44

Figure 18. Fourier transform infrared spectroscopy of samples CP-005 (red) and CP-003 (black), showing similar peak patterns.45

Figure 19. Fourier transform infrared spectroscopy of samples CP-009 (red) and CP-006 (black), compared to cinnamic acid (blue), showing identical patterns.46

Figure 21. Fourier transform infrared spectroscopy of samples CP-013 (red) and CP-012 (black), compared to 2-methylimidazole (blue), showing some similarities among the three.	47
Figure 20. X-ray diffraction pattern of samples CP-009 (red) and CP-006 (black), showing similar peaks with an increase in intensity.	47
Figure 22. X-ray diffraction pattern of samples CP-013 (red) and CP-012 (black), showing similar peaks, with sample CP-012 displaying more noise due to higher impurity levels.	48
Figure 23. Influence of pH on the type of compound identified for samples CP-021, CP-022, CP-018, CP-028, and CP-020.....	49
Figure 24. Fourier transform infrared spectroscopy of samples CP-020 (red) and CP-028 (black), showing similar peak patterns.	50
Figure 25. Fourier transform infrared spectroscopy of sodium cinnamate (red) and sample CP-020 (black), showing similar peak patterns at higher wavenumbers than 1400 cm^{-1} and lower than 1100 cm^{-1}	51
Figure 26. Fourier transform infrared spectroscopy of samples CP-20 (red) and CP-013 (black), showing similar peaks at 1309 , 1179 , and 1145 cm^{-1}	52
Figure 27. Fourier transform infrared spectroscopy of 2-methylimidazole (red) and sample CP-020 (black), showing similar peaks at 1310 , 1180 , and 1147 cm^{-1} , but displaced to the right (lower wavenumber values).....	53
Figure 28. X-ray diffraction pattern of samples CP-013 (red) and CP-012 (black), showing similar peaks, with a change in intensity for peak at $7.28\ 2\theta$	53
Figure 30. The electric charge difference from multiple tests under various forces is plotted, with a linear regression fitted to assess the linearity of the piezoelectric reference material (PZT)....	54
Figure 29. Electric charge change measured for the piezoelectric reference element PZT under different applied forces: 11, 23, 42, and 60N. The data shows an increase in charge difference between the upper and lower peak with higher applied forces. The charge difference is indicated by red arrows; larger arrows denote greater changes. The corresponding value changes are also shown in red.....	55
Figure 31. Electric charge change measured for the blank polymer (top) under different applied forces: 100 and 200 N. The data shows no change in electric charge regardless of the applied force. Additionally, the charge change measured for the composite material (bottom) indicates no change in electric charge regardless of the applied force.....	56

List of Tables

Table 1. Comparative Parameters of Robotic Artificial Muscles ^{2,3,8,14}	17
Table 2. Comparative Analysis of Piezoceramic Materials.....	21
Table 3. Comparative Analysis of Piezoelectric Polymer Materials	24
Table 4. Comparative Analysis of Piezoelectric Composite Materials	26
Table 5. Stoichiometric data, synthesis methodologies, and outcomes from the crystallographic analysis of initial explorations.....	44
Table 6. Stoichiometric data, synthesis methodologies, and outcomes from the crystallographic analysis of the coordination of cinnamic acid.....	45
Table 7. Stoichiometric data, synthesis methodologies, and outcomes from the crystallographic analysis of the coordination of 2-methylimidazole.....	46
Table 8. Stoichiometric data, synthesis methodologies, and outcomes from the crystallographic analysis of the subsequent synthesis.....	49
Table 9. Identification of key FTIR peaks in sample CP-020 and their correlation with sodium cinnamate.....	50
Table 10. Analyzing and contrasting FTIR peaks in sample CP-020 with those of sodium cinnamate.....	50
Table 11. Identification of key FTIR peaks in sample CP-020 and their correlation with sample CP-013.....	51
Table 12. Analyzing and contrasting FTIR peaks in sample CP-020 with those of 2-methylimidazole.....	51
Table 13. Initial lattice indexing parameters and space groups for CP-020 and CP-028.....	52
Table 14. Le Bail refinement parameters for CP-020 and CP-028.....	52

Chapter 1: Introduction

1.1 Background

The field of prosthetics has significantly advanced with bionic prosthetics that use electronic circuits and motors to mimic limb movements (see **Figure 1a**), yet they still face challenges in strength, flexibility, and adaptability. Current prosthetics struggle to replicate the natural appearance and functionality of human limbs due to actuation limitations, often relying on heavy actuators that do not fit anthropomorphic sizes or operational characteristics¹. These spatial constraints restrict the number of actuators that can be included without increasing bulkiness or weight, resulting in limited and less natural movement. Conversely, the human arm's 24 skeletal muscles offer a diverse range of motion and flexibility, deforming naturally during movement.

To address these limitations, research has focused on developing robotic musculoskeletal systems (see **Figure 1b**). These systems are created using robotic artificial muscles, which are a subset of artificial muscles designed to emulate biological counterparts by generating work in biologically inspired ways². These artificial muscles aim to replicate properties such as flexibility, contraction force, deformation strain, efficiency, and power density when activated by stimuli like heat, electricity, or light³. The potential applications of robotic artificial muscles extend to various domains, including soft robotics⁴, biomedical devices^{5,6}, and wearable electronics^{4,7}. These innovations hold promise for creating more natural, adaptable, and functional prosthetic limbs, overcoming the current limitations of strength, flexibility, and adaptability.

The landscape of robotic artificial muscle technologies is vast, with numerous reviews highlighting the diversity of methods and materials employed. Prominent technologies in this field include shape memory polymers (SMPs), shape memory alloys (SMAs), pneumatic actuators, dielectric elastomers (DEAs), ionic polymer-metal composites (IPMCs), soft magnetic actuators, twisted-coiled actuators, electroactive polymers, and piezoelectric materials^{2,3,8}. Each of these technologies brings unique properties and mechanisms to the table, striving to emulate the complex functionalities of biological muscles.

Traditional materials used in crafting these artificial muscles, such as shape memory actuators, twisted coil actuators, soft fluidic actuators, and electroactive polymer actuators, encounter limitations in terms of performance and durability⁶. For instance, while SMAs can provide significant force and deformation, their efficiency and speed can be limited². Twisted coil actuators, although capable of producing large strokes, may suffer from wear and fatigue over time. Similarly, soft fluidic actuators and electroactive polymer actuators offer flexibility but can be hindered by issues related to response time and control precision².

In contrast, piezoelectric materials present a distinct advantage over traditional counterparts due to their superior attributes, including high bandwidth, efficiency, and linearity². These materials can convert electrical energy into mechanical movement with high precision and speed, making them particularly suitable for applications requiring fine control and rapid actuation. The high efficiency of piezoelectric materials also means that they can operate with lower power consumption, which is a critical factor in the design of portable and wearable prosthetic devices. However, many reviews highlight the main disadvantages of piezoelectric actuators, such as their low actuation strain, lack of flexibility, and fragility^{2,3,8}. These reviews primarily reference parameters from well-known piezoceramics, overlooking other classes like polymers and composites.

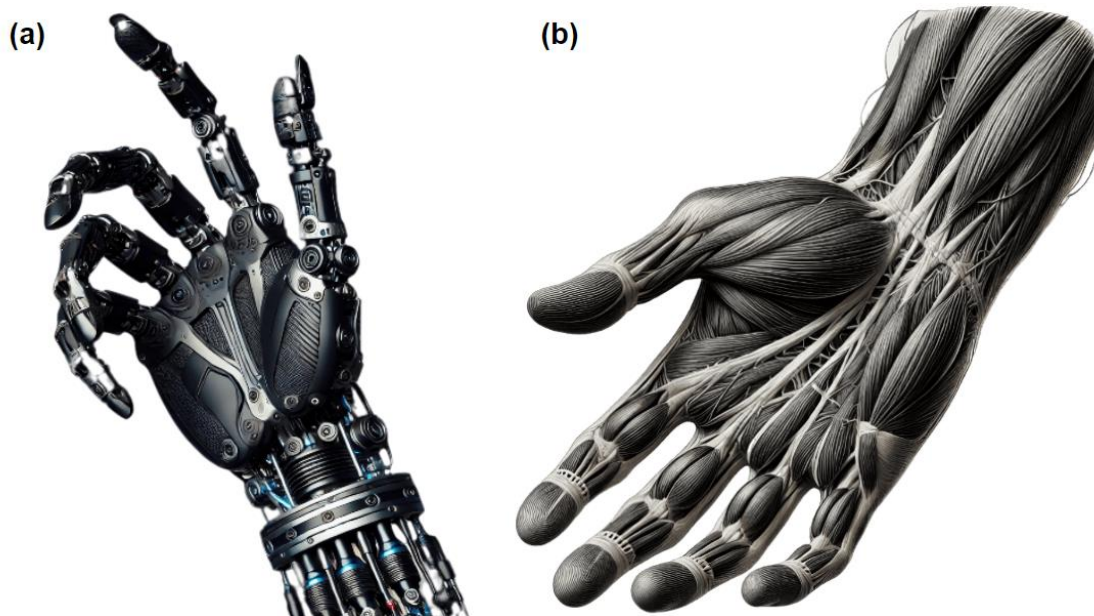


Figure 1. Various types of prosthetic hands. **(a)** The latest advanced prosthetic hand, capable of replicating complex arm movements using electromagnetic actuators and sophisticated mechanisms. Despite technological advancements, it lacks the adaptability of natural limbs. **(b)** A conceptual future perspective of a prosthetic hand equipped with robotic artificial muscles that aim to emulate the flexibility and contraction strength of real skeletal muscles, potentially replicating the intricate motions of natural limbs.

1.2 Problem Statement

Piezoelectric materials can be classified into three well-known categories: ceramics, polymers, and composites. In 1880, Jacques and Pierre Curie made the pioneering description of piezoelectric materials⁹. These materials are characterized by the piezoelectric effect, a phenomenon observed in non-centrosymmetric materials, where an electric field is generated when subjected to mechanical stress, and conversely, mechanical strain is generated when an electric field is applied. Although ceramics boast high piezoelectric coefficients, they are brittle and susceptible to fracture when subjected to an electric field¹⁰. Piezoelectric polymers offer enhanced flexibility, ease of processing, and biocompatibility¹¹, albeit with slightly lower piezoelectric coefficients compared to ceramics¹². Composite materials intend to combine the strengths of ceramics and organic polymers, aiming to preserve flexibility while showcasing high piezoelectric properties. In theory, this combination should result in materials that leverage the best attributes of both components: the high piezoelectric coefficients of ceramics and the flexibility and ease of processing of organic polymers. However, a comprehensive review of the literature reveals a different reality. Despite the theoretical advantages, composite materials often fall short in practice, failing to significantly improve both mechanical and piezoelectric properties.

However, a new category of piezoelectric materials has recently emerged in the literature: coordination polymers (CPs), which combine the advantages of piezoceramics and piezoelectric polymers. These CPs, comprising polydentate ligands linked to metal ions, exhibit a wide range of structural diversity and chemical versatility, enabling the possibility of achieving high piezoelectric coefficients while maintaining flexibility, particularly in the case of one-dimensional CPs¹³. This unique combination makes CPs promising candidates for achieving better elastic compliance (s), the inverse of E ¹², and enhanced piezoelectric coefficients.

The structural diversity of CPs allows for fine-tuning their properties through careful selection of metal ions and organic ligands. This versatility means that CPs can be engineered to exhibit

specific mechanical and piezoelectric properties, potentially overcoming the limitations seen in traditional piezoelectric materials. For instance, one-dimensional CPs can offer high degrees of flexibility and mechanical robustness while also providing substantial piezoelectric responses, which are crucial for the development of advanced robotic artificial muscles.

Advances in robotic artificial muscles have significant implications for both biomedical and industrial applications. In biomedical fields, piezoelectric-based robotic muscles could lead to highly responsive and adaptive prosthetics^{5,6}, offering patients improved control and natural movement. This technology has the potential to revolutionize prosthetic design, enhancing the quality of life for individuals requiring limb replacements. In industrial settings, soft robotics^{4,5}, powered by piezoelectric materials, could provide solutions for tasks that require delicate handling or manipulation in confined spaces, such as in the assembly of microelectronics or in environments hazardous to humans. These applications underscore the practical relevance of further advancing piezoelectric materials like CPs in solving real-world challenges.

Despite their potential, research on CPs has primarily focused on their chemical synthesis and structural characterization, with relatively few studies specifically targeting their piezoelectric and mechanical properties. Most existing studies have been exploratory, aiming to establish basic understanding and proof-of-concept demonstrations¹³. As a result, there is a significant gap in the literature regarding the optimization of CPs for this specific application that requires both high piezoelectric coefficients and superior s .

To fully realize the potential of CPs, more targeted research is needed. This includes systematic studies to understand the relationship between the chemical structure of CPs and their piezoelectric properties, as well as efforts to enhance their mechanical performance without compromising their piezoelectric efficiency. Advanced characterization techniques and computational modeling could play crucial roles in guiding the design of new CPs with tailored properties.

1.3 General Objective

The general objective of this research is to develop and optimize materials based on CPs that demonstrate high piezoelectric coefficients and superior mechanical flexibility, specifically for use in advanced robotic artificial muscles. A key part of this objective is to conduct a comprehensive review of artificial muscle types, focusing on various piezoelectric materials—ceramics, polymers, CPs, and composites—and their limitations. By evaluating these materials based on key parameters, the goal is to identify the most suitable category for this application and explore the potential to engineer CPs that not only match but potentially surpass traditional materials in terms of piezoelectric performance and flexibility. These conventional materials often lack the necessary mechanical flexibility or fail to achieve desired piezoelectric properties, making it essential to explore alternative solutions. CPs, with their unique ability to combine the advantageous properties of both ceramics and polymers, offer a promising pathway toward achieving the dual objectives of high piezoelectricity and flexibility, which are critical for mimicking the complex functions of natural skeletal muscles. This review also aims to deepen understanding of how existing artificial muscle technologies address the intricate challenges posed by natural muscle mechanics. Establishing benchmarks based on the performance parameters of natural muscles will be crucial to rigorously evaluate the developed artificial muscles, ensuring their efficacy as equal or superior alternatives in terms of actuation technology compared to natural counterparts.

1.4 Specific Objectives

The first objective aims to pioneer a novel category of piezoelectric materials through the synthesis of CPs designed to exhibit superior piezoelectric properties. This endeavor involves a meticulous exploration of optimal ligands and metals to enhance both piezoelectricity and mechanical flexibility. Special attention is directed towards developing non-centrosymmetric one-dimensional structures, with a specific focus on incorporating zinc (Zn) and chiral ligands to maximize non-centrosymmetry. By focusing on these structural characteristics, the objective is to achieve a delicate balance that enhances both s and piezoelectric performance simultaneously. This approach not only seeks to advance the fundamental understanding of CPs but also aims to pave the way for practical applications in the field of robotic musculoskeletal systems.

The second objective addresses the inherent challenge of CPs, which typically form in crystal or powder form. To advance their suitability for applications in robotic artificial muscles, a critical strategy involves integrating these CPs into polymeric matrices. This integration is essential for enhancing the materials' mechanical flexibility. Building on the concept of developing new composite materials, this approach utilizes organic polymers as a matrix, leveraging their advantageous mechanical properties. By embedding CPs within these matrices, the objective is to overcome limitations observed in current composites that combine polymeric matrices with ceramic components. This innovative composite material aims to significantly improve both s and piezoelectric coefficients simultaneously, fulfilling the original intent of actual composite materials.

Chapter 2: Literature Review

2.1 Robotic Artificial Muscles

The landscape of robotic artificial muscle technologies is vast, with numerous reviews highlighting the diversity of methods and materials employed. Some prominent technologies include SMPs, SMAs, pneumatic actuators, DEAs, IPMCs, soft magnetic actuators, twisted-coiled actuators, electroactive polymers, and piezoelectric materials^{2,3,8}. Key parameters for comparing these technologies include linearity, bandwidth, actuation strain, actuation stress, efficiency, work density, and Young's modulus (E)².

Linearity, which measures the accuracy of a linear model in predicting an artificial muscle's performance, is a crucial parameter when evaluating these technologies. Skeletal muscles exhibit a linearity of approximately 70% (**Table 1**), serving as a reference point for artificial muscle technologies. Piezoelectric materials stand out with the highest linearity, around 90% (**Table 1**), making them highly precise for applications requiring consistent performance. Twisted-coiled actuators also show notable linearity at approximately 85%, followed by SMPs, pneumatic actuators, and DEAs, all around 70%, closely mimicking the linearity of skeletal muscles. SMA and IPMCs display lower linearity at about 55 and 65%, respectively (**Table 1**). The high linearity of piezoelectric materials and twisted-coiled actuators highlights their reliability in applications where predictability and precision are paramount, whereas the relatively lower linearity of SMA and IPMCs indicates potential variability in performance.

The actuation strain of skeletal muscles, which ranges from 1 to 100%, serves as a benchmark for evaluating artificial muscle technologies. SMPs, pneumatic actuators, DEAs, and soft magnetic actuators match or even exceed this range, with SMPs achieving strains below 100%, pneumatic actuators ranging from 10 to 100%, DEAs achieving up to 1000%, and soft magnetic actuators also covering the 1 to 100% range. In contrast, SMAs and piezoelectric materials fall short, with SMAs achieving less than 8% and piezoelectric materials less than 2% actuation strain (**Table 1**). IPMCs and twisted-coiled actuators also have limited strain capabilities, with IPMCs between 0.5 to 10% and twisted-coiled actuators under 50%. Conductive polymers offer actuation strains below 40%, positioning them below the upper threshold of skeletal muscle capabilities. Piezoelectric materials, despite their high linearity of approximately 90%, exhibit the least actuation strain, highlighting a significant limitation compared to natural skeletal muscles and other artificial muscle technologies.

Table 1. Comparative Parameters of Robotic Artificial Muscles^{2,3,8,14}.

Technology	Linearity [%]	Actuation Strain [%]	Actuation Stress [MPa]	Efficiency [%]	Bandwidth [Hz]	Work Density [kJ/m ³]	Young's Modulus [MPa]
Skeletal Muscle	~ 70	1 – 100	0.007 – 0.8	35	2 – 173	35	10 – 60
SMP	~ 70	< 100	< 3	< 10	< 1	< 2000	1 – 1000
SMA	~ 55	< 8	< 700	< 10	< 35	10 ⁴ – 10 ⁵	10 ³ – 10 ⁵
Pneumatic	~ 70	10 – 100	< 10	< 40	~ 100	1 – 200	0.1 – 100
DEA	~ 70	1 – 1000	< 7.2	60 – 90	< 1000	10 – 5000	0.1 – 10
IPMC	~ 65	0.5 – 10	< 30	< 10	< 100	1 – 10	25 – 2500
Soft Magnetic	-	1 – 100	-	-	-	< 300	0.1 – 10
Twisted Coiled	~ 85	< 50	< 40	< 1	< 7.5	-	-
Conductive Polymers	-	< 40	< 34	< 18	< 1000	< 100	-
Piezoelectric	~ 90	< 2	110	> 90	< 10 ⁸	100 – 1000	10 ³ – 10 ⁵

Actuation stress, the maximum mechanical force an artificial muscle can exert, is a vital metric for comparing different technologies. Skeletal muscles exhibit actuation stresses from 0.007 to 0.8 MPa. SMAs stand out with stresses up to 700 MPa, significantly surpassing natural muscles. Piezoelectric materials also offer high actuation stress up to 110 MPa, combining this with high efficiency and bandwidth, though they have limited actuation strain. Pneumatic actuators provide stresses below 10 MPa, sufficient for many applications and exceeding skeletal muscle capabilities. DEAs and IPMCs offer stresses up to 7.2 and 30 MPa, respectively, making them competitive in mechanical force, with DEAs excelling in strain and efficiency. Twisted-coiled actuators and conductive polymers achieve moderate stresses, up to 40 and 34 MPa, respectively, higher than skeletal muscle but with varying efficiency. SMPs have lower actuation stress, less than 3 MPa, but compensate with high strain. Most artificial muscle technologies surpass the actuation stress of skeletal muscles, with SMAs and piezoelectric materials being particularly strong, suitable for applications demanding high mechanical force.

Efficiency, representing the ratio of output power to input power, is a crucial parameter for assessing the performance and sustainability of artificial muscle technologies. Skeletal muscles typically achieve efficiencies up to 35% (**Table 1**), varying depending on muscle type and activity. Notably, pneumatic actuators, DEAs, and piezoelectric actuators stand out among artificial muscle technologies for matching or surpassing this efficiency benchmark. Pneumatic actuators offer efficiencies exceeding 40% (**Table 1**), making them highly energy-efficient options, too. DEAs demonstrate impressive efficiency ranging from 60 to 90% (**Table 1**), showcasing their ability to convert input energy into mechanical work effectively. Piezoelectric actuators exhibit efficiencies exceeding 90% (**Table 1**), making them one of the most efficient technologies

available. However, it's essential to consider the trade-offs between efficiency and other performance parameters such as actuation strain and stress.

Bandwidth, which denotes the range of frequencies at which an actuator can operate effectively, is a key consideration for many applications requiring dynamic movements or responses. Skeletal muscles have a bandwidth ranging up to 173 Hz (**Table 1**), reflecting their ability to swiftly adapt to varying stimuli. Several artificial muscle technologies demonstrate comparable or even superior bandwidths. Notably, DEAs, conductive polymers, and piezoelectric materials stand out for surpassing the bandwidth of skeletal muscles significantly. Dielectric elastomers and conductive polymers operate at frequencies up to 1000 Hz (**Table 1**), enabling rapid and precise responses suitable for various applications. Piezoelectric materials exhibit the highest bandwidths, reaching up to 100 MHz (**Table 1**), making them exceptionally well-suited for high-frequency applications such as ultrasonic actuators and vibration control systems. While some technologies, such as pneumatic actuators and IPMCs, operate at lower bandwidths compared to skeletal muscles, they still offer sufficient performance for many practical applications. Overall, the diverse range of bandwidths among artificial muscle technologies highlights the importance of selecting the appropriate technology based on the specific requirements of the intended application.

Work density, a measure of the work generated by an artificial muscle normalized by its volume, provides insight into the energy efficiency and compactness of these technologies. Skeletal muscles typically exhibit a work density around 35 kJm⁻³ (**Table 1**). Among artificial muscle technologies, several surpass this benchmark, indicating their potential for compact and efficient actuation. DEAs and twisted-coiled actuators, for instance, offer work densities ranging from 10 to 5000 kJm⁻³ and up to 7.5 kJm⁻³ (**Table 1**), respectively, showcasing their ability to generate significant mechanical work relative to their volume. Pneumatic actuators and piezoelectric materials also demonstrate competitive work densities, with pneumatic actuators ranging from 1 to 200 kJm⁻³ and piezoelectric materials reaching up to 1000 kJm⁻³ (**Table 1**). While some technologies, such as IPMCs and conductive polymers, lack specific work density data, their other performance parameters can provide insight into their potential efficiency and compactness. Overall, the range of work densities among artificial muscle technologies underscores the importance of considering energy efficiency and space constraints when selecting the most suitable technology for a given application.

E , representing the stiffness of a material, is a critical parameter for assessing the flexibility and mechanical properties of artificial muscle technologies. Skeletal muscles typically exhibit E ranging from 10 to 60 MPa, reflecting their inherent flexibility and ability to deform under load. Among artificial muscle technologies, there is considerable variability in E values, with some materials exhibiting stiffness comparable to or even lower than skeletal muscles. SMPs and pneumatic actuators, for example, offer relatively low E , making them more flexible and compliant compared to other technologies. DEAs and soft magnetic actuators also demonstrate low E , further highlighting their suitability for applications requiring flexibility and adaptability. In contrast, materials such as piezoelectric actuators tend to have significantly higher E , often exceeding 1 GPa, indicating greater stiffness and less flexibility. While high E can offer advantages in terms of stability and precision, they may also limit the range of motion and adaptability of the artificial muscle. Thus, the selection of a suitable technology should consider the specific mechanical requirements and constraints of the intended application.

However, these reviews often fail to acknowledge the diversity within piezoelectric materials. There are various polymeric forms available with significantly lower E , without compromising the high efficiency, bandwidth, and work density advantages typically associated with piezoelectric materials. This oversight underscores the importance of thoroughly considering the

full spectrum of piezoelectric options, ensuring that the chosen material aligns optimally with the specific requirements and constraints of the intended application.

2.2 Piezoelectric *Materials*

Piezoelectric materials constitute a distinct class renowned for their unique ability to generate electric charge in response to mechanical stress or deformation, and conversely, to deform under an applied electric field—a phenomenon known as the piezoelectric effect. While naturally occurring in specific crystals like quartz, Rochelle salt, and tourmaline, synthetic counterparts have emerged to serve diverse applications. These materials can be categorized into four main groups: ceramics, polymers, and composites (as can be seen Error! Reference source not found.), with a recent addition being CPs (**Figure 3**). Ceramics feature a crystalline structure composed of metallic and non-metallic elements bonded through strong ionic or covalent interactions, imparting them with high hardness and stiffness. Polymers consist of large molecules formed from repeating monomeric units linked by covalent bonds, creating long chains or networks that can be either natural or synthetic. Composites combine organic polymers with ceramics, leveraging the strengths of both materials. CPs are compounds where metal ions are linked by organic ligands through coordination bonds, forming porous frameworks.

In the realm of developing robotic artificial muscles, the dual requirements of flexibility and efficient mechanical force generation are paramount. Thus, the comparison of materials for such applications hinges on meticulously evaluating these two crucial aspects. Firstly, the mechanical properties, including tensile strain, tensile stress, and the E , are scrutinized to ascertain the material's flexibility and resilience, essential for mimicking natural muscle movements in robots. Simultaneously, the investigation delves into piezoelectric properties such as the piezoelectric coefficient and dielectric constant, crucial for the effective conversion of electrical energy into mechanical force. Moreover, assessing the maximum strain or deformation achievable under an electric field provides valuable insights into the material's biomimetic potential, particularly in replicating the contractile behavior observed in real skeletal muscles. By meticulously considering these parameters, researchers can discern the most suitable materials for crafting robotic artificial muscles capable of seamlessly blending flexibility with robust mechanical performance.

2.2.1 Piezoelectric Ceramics

Piezoceramics represents a well-established field of research characterized by high electromechanical coupling factors and piezoelectric coefficients. Lead zirconate titanate (PZT) stands as a benchmark composition, renowned for its exceptional electrical properties and stability, making it a dominant material in this realm for years. The morphotropic phase boundary (MPB), which delineates rhombohedral and tetrahedral phases, serves as a crucial structural feature driving the electromechanical properties of piezoceramics¹⁵. Through strategic doping and synthesis design, PZT and its derivatives exhibit impressive properties, including large

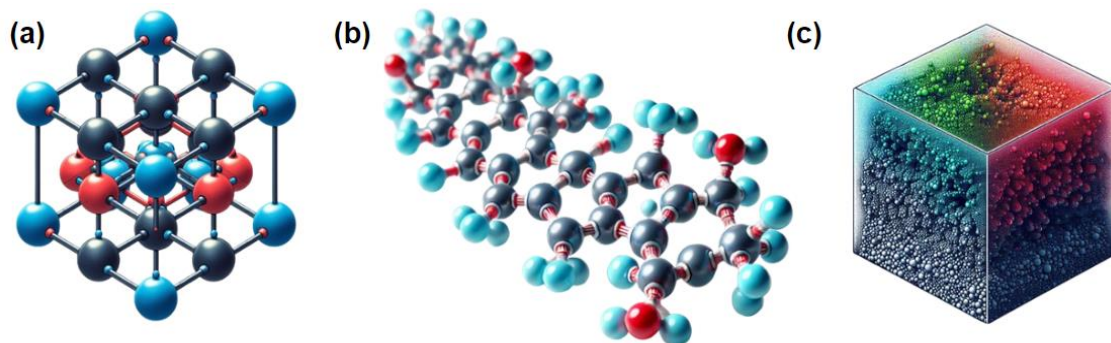


Figure 2. Categories of piezoelectric materials. This image illustrates three distinct categories of piezoelectric materials. **(a)** Ceramics feature a crystalline structure composed of metallic and non-metallic elements bonded through strong ionic or covalent interactions. **(b)** Polymers consist of large molecules formed from repeating monomeric units linked by covalent bonds, creating chains or networks. **(c)** Composites merge organic polymers with ceramics, combining the structural benefits of both materials.

piezoelectric coefficients, electromechanical coupling factors, and low mechanical quality factors, enabling diverse applications such as positioning elements in photolithography, medical diagnostics, sensors, and actuators¹⁶. Despite these advantages, the mechanical properties of piezoceramics are often overlooked or compromised to enhance their electrical properties. Therefore, it is imperative to consider E when selecting materials for applications like artificial muscles, which require endurance under numerous mechanical cycles and stress shocks.

The polycrystalline ceramic composed of sodium bismuth titanate and potassium bismuth titanate (NBT-KBT) has been reported to have the highest E , with values ranging from 146,650 to 203,610 MPa (**Table 2**). This material is fabricated using a metal-organic decomposition (MOD) method, varying the sodium and potassium mole fractions $(\text{Na}_{1-x}\text{K}_x)_{0.5}\text{Bi}_{0.5}\text{TiO}_3$ where x is 0.15, 0.18, 0.20, and 0.25. As the potassium content increased, the material became more flexible, reducing the E to 146,650 MPa. This change indicates that substituting Na with K disrupts the perovskite lattice, weakening the inner bonds and causing a more flexible structure. Thin films of NBT-KBT depend heavily on their crystallographic orientation to maximize piezoelectricity near the MPB. The NBT-KBT films with a (100) orientation enhance the MPB but exhibit low piezoelectric coefficient d_{33} values between 73 and 95 pmV^{-1} . Consequently, while NBT-KBT has some flexibility, its piezoelectric properties are relatively low.

PZT boasts several electromechanical benefits, but there are variations that offer even better performance, such as lead bismuth zirconate titanate (PBiZT), lead sodium niobate zirconate titanate (PNNZT)¹⁷, and the polycrystalline ceramic combining lead manganese antimony oxide and PNNZT (PMS-PNNZT)¹⁷. Among these, PBiZT has the lowest E , reported at 10,300 MPa (**Table 2**), which is fourteen times lower than the minimum value for NBT-KBT¹⁸, indicating much higher flexibility. However, PBiZT's d_{33} value of 130 pCN^{-1} , while within the typical PZT range (from 56 to 400 pCN^{-1} , **Table 2**), is still lower than those of certain sintered ceramics, which achieve d_{33} of 900 pmV^{-1} and 1058 pmV^{-1} for PNNZT and PMS-PNNZT (**Table 2**), respectively. PNNZT displays a coexistence of rhombohedral and tetragonal symmetries, which shifts towards a predominantly rhombohedral phase with the addition of $\text{Pb}(\text{Mn}_{1/3}\text{Sb}_{2/3})\text{O}_3$ (PMS), affecting the MPB. This shift increases the mechanical quality factor, hardening the material but also reducing its d_{33} within a certain molar percentage range due to the predominance of Mn^{2+} over Sb^{2+} in the compound¹⁷.

Table 2. Comparative Analysis of Piezoceramic Materials

Material Acronym	Strain Amplitude [%]	Young's Modulus [MPa]	Piezoelectric Coefficient [pC/N-1 pm/V-1]	Dielectric Constant [-]	Ref
PZT	-	64000 – 120000	33 – 750	424 – 1200	19-25
PBiZT	-	10,300	130	-	26
PMS-PNNZT	0.083 – 0.115	101000 – 135400	746.7 – 1058	-	17
PNNZT	0.09	98,700	900	-	17
NBT-KBT	-	146650 – 203610	73 – 95	180 – 240	18
KNNS-BNZ-CT	-	74,500	350	2,545	27
KNNS-LNNS-BNZ-CT	-	84900 – 142600	45 – 215	233 – 1407	27
FASnI3	-	120,000	13	-	28
BNKT-BTONb	-	93000 – 114000	157 – 198	4731 – 5439	29
BNT-BTO-BNMN	-	114,000	110	520	23
ZnO	-	16800 – 40000	3.27 – 31.4	-	19,27
BTO	-	67000 – 119047	191 – 330	1,550	19,25
LKNNT	-	13,000	150	-	30

Both the electrical and mechanical properties of BTO- and KNN-based materials have been studied as promising alternatives to PZT. As a standalone material, BTO exhibits E values ranging from 67,000 to 119,047 MPa (**Table 2**). When doped, BTO reveals new properties; for instance, BNKT-BTNb (bismuth sodium potassium titanate and BTO-niobium)²⁹ and BNT-BTO-BNMN (bismuth sodium titanate -BTO- barium sodium niobate magnesium) show intermediate increases in E , with values of 93,000 up to 114,000 MPa and 114,000 MPa, respectively. These dopants, however, appear to limit BTO's flexibility, aligning it with PZT variations, which range from 98,700 to 135,400 MPa (**Table 2**). A significant drawback of BTO-based materials is their relatively low d_{33} values: 110 pC/N⁻¹ for BNT-BTO-BNMN and 157 to 198 pC/N⁻¹ for BNKT-BTNb. BNKT naturally exhibits a ferroelectric order with a d_{33} value that does not heavily depend on the MPB³¹. Doping BNKT with BTNb disrupts this natural order, increasing hardness but disturbing electrical dipole arrangements, thus reducing piezoelectricity²⁹. BTO materials are also known for their significant dielectric constant values, a trait shared with other ceramics³². Notably, BNKT-BTNb features a dielectric constant of 4731 to 5439, the highest in this review. This high

dielectric constant, driven by crystallinity phase structure, requires attention due to potential electrostriction effects that could impact material shape.

KNN-based piezoceramics present a promising alternative to PZT materials, offering better flexibility supported by lower E values while maintaining acceptable piezoelectric behavior. The most representative KNN-based material is lithium potassium sodium niobium tantalate (LKNNT), which has an E value similar to that of PBiZT at around 13,000 MPa (**Table 2**). A LKNNT thick film was spin-coated on a *Pt/Ti/Si* substrate and subjected to rapid thermal annealing to optimize grain size and reduce defects. This process resulted in a material with lower hardness and higher flexibility, although it faced challenges in restoring its initial shape due to higher internal residual stress. The d_{33} value of LKNNT is comparable to that of PBiZT, reinforcing its potential as a lead-free alternative for piezoceramics.

Other KNN variations, such as KNNS-BNZ-CT and KNNS-LNNS-BNZ-CT, also exhibit promising properties despite their intermediate results. KNNS-BNZ-CT has an E value of 74,500 MPa, while KNNS-LNNS-BNZ-CT shows a range of 84,900 to 142,600 MPa (**Table 2**) depending on the LNNS content²⁷. These materials demonstrate significant charge storage capabilities, with dielectric constants of about 2,545 and 233 to 1,407, respectively (**Table 2**). Additionally, KNNS-BNZ-CT boasts a superior d_{33} of 350 pC·N⁻¹, while KNNS-LNNS-BNZ-CT exhibits a d_{33} ranging from 45 to 215 pC·N⁻¹ (**Table 2**). These properties make KNN-based piezoceramics a viable and flexible alternative to traditional PZT materials, suitable for various applications.

Among the materials listed, lead bismuth zirconate titanate (PBiZT) has the lowest E at 10,300 MPa (**Table 2**), indicating higher flexibility compared to other materials. However, this value is still relatively high for materials intended for artificial muscles, which typically require much lower stiffness to facilitate efficient and responsive movement. PBiZT also has a moderate d_{33} of 130 pC·N⁻¹ (**Table 2**). On the other hand, the polycrystalline ceramic combining lead manganese antimony oxide and lead sodium niobate zirconate titanate (PMS-PNNZT) exhibits the highest d_{33} , ranging from 746.7 to 1058 pmV⁻¹ (**Table 2**), which is significantly higher than other materials. Despite its excellent piezoelectric performance, PMS-PNNZT has a very high E , ranging from 101,000 to 135,400 MPa (**Table 2**), making it unsuitable for applications requiring significant mechanical flexibility. While PBiZT offers better flexibility, its E is still too high for optimal use in artificial muscles. PMS-PNNZT, with its superior piezoelectric properties, lacks the necessary flexibility. Therefore, despite their individual strengths, neither PBiZT nor PMS-PNNZT fully meets the requirements for robotic artificial muscles.

2.2.2 Piezoelectric Polymers

Piezoelectric polymers represent a burgeoning frontier in research, showcasing materials with substantial electromechanical coupling and impressive piezoelectric coefficients, offering distinct advantages such as flexibility and lightweight properties over conventional piezoceramics. However, piezoelectric polymers typically exhibit low piezoelectricity, prompting the utilization of various treatments like annealing for higher crystallinity via heat treatment, drawing for polymer alignment through elongation, and poling for aligning dipoles via electric fields³³. These methodologies serve to enhance the material's inherent properties.

Piezoelectric polymers offer several advantages for constructing robotic artificial muscles. Their exceptional flexibility enables them to bend, twist, and stretch, making them ideal for mimicking the movements of natural muscles. Moreover, their piezoelectric properties remain strong despite the tradeoff between flexibility and piezoelectricity. This unique combination of flexibility and

piezoelectricity not only allows for precise and adaptable motion but also enhances energy efficiency by converting mechanical strain into electrical energy, thereby potentially prolonging the operational lifespan of robotic systems.

Among the discussed materials, chitosan (CS) stands out with the highest E , boasting a value of 1700 MPa (**Table 3**). CS exhibits a relatively low d_{33} of 12.4 pC/N (**Table 3**), positioning it among the materials with lower piezoelectricity within the category of polymeric piezoelectric materials considered in this review. Additionally, CS possesses a dielectric constant of 28 (**Table 3**), marking it as one of the highest among polymeric materials but notably smaller when compared to the values typically observed in ceramic materials.

Polypropylene (PP) stands out as the third stiffest among the piezoelectric polymers considered in this review, boasting a E of 1000 MPa (**Table 3**). With a d_{33} of 140 pC/N (**Table 3**), PP demonstrates moderate piezoelectricity within the spectrum of piezoelectric polymers. Another noteworthy variant, isostatic polypropylene (i-PP), shares similar E values with conventional PP, standing at 1064 MPa (**Table 3**). This unique material processed using an isostatic compression technique³⁴, showcases exceptional tensile strain, reaching up to 626%, indicating remarkable deformability before fracture. Moreover, i-PP exhibits impressive tensile strength, withstanding high stresses up to 31 MPa (**Table 3**), marking it as the most resilient among piezoelectric polymeric materials. Despite its mechanical robustness, i-PP presents a relatively low d_{33} of 14 pC/N (**Table 3**) which dampens its noteworthy application for artificial muscles. In contrast, electronic irradiated polypropylene (IXPP), treated with electron irradiation to enhance its mechanical properties^{35,36}, demonstrates significantly lower E values ranging between 0.7 and 6.3 MPa (**Table 3**). These lower modulus values make IXPP more desirable for applications requiring flexibility and deformability. Additionally, despite its decreased stiffness, IXPP exhibits a remarkable d_{33} ranging between 400 to 650 pC/N (**Table 3**), surpassing PLA as one of the highest values among piezoelectric polymers. This impressive piezoelectricity is attributed to the aligned β -phase crystalline structure and molecular orientation of IXPP's polymer chains³⁵. However, IXPP's dielectric constant remains low at 1.6 (**Table 3**), underscoring that a high piezoelectric coefficient does not necessarily correlate with a high dielectric constant.

Poly(lactic acid) (PLA) emerges with the lowest reported E , ranging from 0.15 kPa to 10 MPa (**Table 3**), signifying its high ductility even at the upper end of the scale. Despite its remarkable flexibility, PLA exhibits one of the highest piezoelectric coefficients d_{33} among the piezoelectric polymers, ranging between 500 to 600 pC/N (**Table 3**). However, PLA's dielectric constant remains relatively low at 1.4 (**Table 3**). To harness its piezoelectric properties, various processing techniques are employed, including additive manufacturing and hot pressing to fabricate PLA samples into film shapes. Additionally, aluminum electrodes are deposited onto the surface of the sample through techniques such as evaporation deposition and physical vapor deposition (PVD)^{36,37}. These methods enhance the piezoelectric performance of PLA, making it a promising candidate for diverse applications requiring flexible and highly responsive materials.

Polydimethylsiloxane (PDMS) exhibits a notably low E , with reported values around 0.5 MPa (**Table 3**), indicating its high flexibility and deformability. Despite its low modulus, PDMS demonstrates promising piezoelectric properties, with a d_{33} coefficient ranging from 32.8 to 341 pC/N (**Table 3**), placing it among the top performers alongside PLA and IXPP within the category of piezoelectric polymers. PDMS samples are predominantly fabricated in film form using techniques such as multilayer casting or spin coating^{38,39}. These methods enable the production of thin, uniform films, optimizing PDMS's piezoelectric characteristics and rendering it suitable for various applications requiring flexible and responsive materials.

Table 3. Comparative Analysis of Piezoelectric Polymer Materials

Material Acronym	Tensile Strain [%]	Young's Modulus [MPa]	Tensile Strength [MPa]	Piezoelectric Coefficient [pC/N pm/V]	Dielectric Constant [-]	Ref
PVDF-TrFE	179.4 – 354.1	8.7 – 20.8	9.2 – 28.9	14.6 – 108	4.7	40
PP	-	1,000	-	140	1.2	36
IXPP	-	0.7 – 6.3	-	400 – 650	1.6	35,36
PLA	-	0.00015 – 10	-	500 – 600	1.4	36,37
i-PP	626	1,064	31	14	-	34
PVDF	80.4 – 697	2.5 – 136.5	0.7 – 13	3.27 – 15.2	-	41,42
PDMS	-	0.5 – 0.51	-	32.8 – 341	-	38,39
TrFE-CTFE	487.2	27	25	51	5.5	40
PVDF-TrFE-CTFE	97.1 – 389.3	3.1 – 9.8	2.7 – 23.9	30.2	5.5	40
CTFE-TrFE	194 – 350	11 – 18	8 – 21	15	4.9	40
PAN	175.4	1.24	1.18	8	-	43
CS	-	1,700	-	12	28	44

Polyvinylidene fluoride (PVDF) exhibits a wide range of mechanical and piezoelectric properties, making it a versatile material for various applications. PVDF displays E ranging from 2.5 to 136.5 MPa (**Table 3**), indicating considerable flexibility and ductility. Additionally, PVDF possesses a relatively high tensile strain at break, ranging from 80.4 to 697% (**Table 3**), underscoring its resilient and flexible nature. Despite its flexibility, PVDF also demonstrates a tensile strength ranging between 0.7 and 13 MPa (**Table 3**), indicating its ability to withstand stress. However, the reported d_{33} for PVDF falls between 3.27 pmV⁻¹ and 15.2 pCN⁻¹ (**Table 3**), which is comparatively low. To enhance PVDF's piezoelectric properties, methods such as electrospinning and non-solvent induced phase separation (NIPS) are employed to produce films^{41,42}. Furthermore, variations like polyvinylidene fluoride trifluoroethylene (PVDF-TrFE) and polyvinylidene fluoride trifluoroethylene chlorotrifluoroethylene (PVDF-TrFE-CTFE) exhibit similar E values to PVDF but with varied mechanical and piezoelectric properties as seen in **Table 3**. PVDF-TrFE, for instance, demonstrates a E of 8.7 to 20.8 MPa and a tensile strain at break ranging from 179.4 to 354.1%, albeit with a lower piezoelectric coefficient (**Table 3**). Similarly, PVDF-TrFE-CTFE shows a E between 3.1 and 9.8 MPa, a tensile strain at break between 97.1 and 389.3%, and a d_{33} of 30.2 pCN⁻¹ (**Table 3**). These variations are synthesized into membranes using methods such as uniaxial electrospinning and coaxial electrospinning to tailor their

properties for specific applications⁴⁰. Additionally, materials solely comprising trifluoroethylene and chlorotrifluoroethylene units in different orders exhibit distinct mechanical and piezoelectric properties. For instance, TrFE-CTFE and CTFE-TrFE demonstrate E values closer to PVDF but with varying tensile strength, elongation at break, and piezoelectric coefficient.

Polyacrylonitrile (PAN) exhibits a E of 1.24 MPa (**Table 3**), reflecting its notably low stiffness, akin to that of PLA and PDMS. Despite its low modulus, PAN displays a tensile strain at break of 175.4%, which, while smaller, is comparable to the lower range provided for PVDF-TrFE (**Table 3**). However, PAN's tensile strength of 1.18 MPa (**Table 3**) is relatively low, indicating its limited resistance to stress. Furthermore, PAN demonstrates a d_{33} of 8 pC/N (**Table 3**), positioning it as one of the least piezoelectric polymers in this review, although falling within the range reported for pure PVDF. Samples of PAN with these characteristics were formed into small cylinders using a solution casting method⁴³. Overall, PAN's mechanical and piezoelectric properties make it suitable for specific applications where low stiffness and modest piezoelectricity are desired.

Among the materials listed, PLA stands out as the material with the lowest E , boasting a value of 0.15 kPa (**Table 3**), which is significantly lower than other values within piezoelectric polymers. PLA demonstrates remarkable piezoelectric properties, with a maximum coefficient d_{33} of 600 pC/N (**Table 3**), ranking it as the second highest among the piezoelectric polymers considered in this review. However, the material with the highest piezoelectric coefficient is IXPP, with the highest reported d_{33} value of 650 pC/N (**Table 3**), showcasing superior piezoelectric properties compared to other listed materials. IXPP also exhibits a very low E of 0.7 MPa (**Table 3**), further highlighting its exceptional flexibility and piezoelectric performance. Similarly, PDMS presents high piezoelectric coefficients, with the highest reported value being 341 pC/N (**Table 3**), along with good mechanical flexibility indicated by its lowest E of 0.5 MPa (**Table 3**). These materials demonstrate promising potential for applications in robotic artificial muscles, where the combination of high piezoelectricity and mechanical flexibility is crucial for mimicking natural muscle movements with precision and efficiency.

2.2.3 Piezoelectric Composites

Composite piezoelectric materials, integrating flexible matrices or substrates like polymers or elastomers, present enhanced flexibility while preserving piezoelectric characteristics, rendering them ideal for conforming to curved or irregular surfaces in various applications¹⁹. Through adjustments in composition or microstructure, it becomes feasible to tailor the piezoelectric properties of the composite to fulfill precise application requirements, such as operating frequency, voltage output, or sensitivity¹⁹. In the realm of robotic artificial muscles, integrating piezoelectric ceramics into flexible substrates and elastomeric matrices enables the development of innovative artificial muscle systems that mimic natural movements. Additionally, incorporating nanomaterials like nanowires, nanoparticles, or nanotubes enhances the mechanical strength and sensitivity of piezoelectric composites, crucial for efficient robotic muscle operation.

PDMS, renowned for its favorable piezoelectric and mechanical properties, has become a key component in numerous composite materials. One such composite, PDMS-CN, integrates carbon nanotubes into PDMS through solution casting⁴⁵, resulting in a composite with an E of 0.5 MPa (**Table 4**), equivalent to pure PDMS. While PDMS-CN exhibits a tensile strain at break of 71% and a tensile strength of 0.26 MPa, its d_{33} of 47.6 pmV⁻¹ (**Table 4**) falls within the lower range of reported values for PDMS. Notably, its dielectric constant of 175 (**Table 4**) surpasses that of conventional piezoelectric polymers. Another composite, PDMS-BTO-MWCNT, combines barium titanate (BTO) and multiwalled carbon nanotubes with PDMS via solution casting⁴⁶, yielding a E ranging between 0.45 and 1.72 MPa (**Table 4**). Despite the variability in modulus

depending on the crosslinker-to-monomer ratio, PDMS-BTO-MWCNT retains values similar to PDMS while exhibiting a d_{33} ranging from 60 to 125 pC/N⁻¹ (**Table 4**). By contrast, BTO, when not integrated into any matrix, exhibits a notably higher E . Similarly, a composite incorporating iron oxide into PDMS matrix (PDMS-Fe₃O₄) via foam forming⁴⁷ exhibits a E of 0.37 MPa (**Table 4**), akin to pure PDMS. However, PDMS-Fe₃O₄ showcases a d_{33} of 82 pC/N⁻¹ (**Table 4**), falling within the lower range of PDMS coefficients.

Table 4. Comparative Analysis of Piezoelectric Composite Materials

Material Acronym	Actuation Strain [%]	Tensile Strain [%]	Young's Modulus [MPa]	Tensile Strength [MPa]	Piezoelectric Coefficient [pC/N pm/V]	Dielectric Constant [-]	Ref
PDMS-CN	-	71	0.5	0.26	47.6	175	45
PDMS-BTO-MWCNT	-	-	0.45 – 1.72	-	60 – 125	-	46
PDMS-Fe ₃ O ₄	-	-	0.37	-	82	-	47
PDMS-PTFE	-	-	0.37	-	106	-	47
PDMS-PSF	6.7	325	0.11	0.16	19	4	48
PDMS-PSF-Ag	3.6 – 22.6	381 – 555	0.12 – 0.28	0.26 – 0.31	15 – 17.7	3.5 – 4.1	48
PDMS-Ag	17.5	460	0.48	0.51	6	5	48
PDMS-Cl	-	240	0.21	0.2	14	24	45
PVDF-TrFE-MWCNT	-	-	986	-	50	-	49
PVDF-BTO	-	660 – 1000	120.1 – 206.7	13.1 – 19.4	3.81 – 5.62	-	41
PVDF-PAN	-	90.7 – 135	2.56 – 4.24	1.58 – 1.86	14 – 30	-	43
i-PP-SiO ₄	-	543 – 644	1068 – 1259	28.5 – 31	80 – 200	-	34
CS-ZnO	-	-	4500 – 9090	-	60.6 – 65.9	43 – 46.5	44

Another composite material, PDMS-PTFE, combines polytetrafluoroethylene (PTFE) and PDMS through foam forming and micro plasma discharge⁴⁷. This composite exhibits a E of 0.37 MPa (**Table 4**), similar to that of PDMS, indicating its flexibility and suitability for applications

requiring soft and pliable materials. Remarkably, PDMS-PTFE also demonstrates a d_{33} of 106 pCn⁻¹ (**Table 4**), falling within the range of coefficients reported for PDMS. Similarly, another composite, PDMS-PSF, integrates PDMS and polysulfone (PSF) through solution casting⁴⁸. While PDMS-PSF presents a lower E of 0.11 MPa (**Table 4**) compared to PDMS, it boasts a high tensile strain of 325% and a tensile strength of 0.16 MPa, highlighting its remarkable flexibility and mechanical properties. However, PDMS-PSF exhibits a relatively low d_{33} of 19 pCn⁻¹ (**Table 4**), indicating its limited piezoelectric responsiveness compared to pure PDMS.

Additionally, PDMS-PSF-Ag, incorporating silver nanoparticles into the PDMS-PSF matrix⁴⁸, demonstrates a varied E between 0.12 to 0.28 MPa (**Table 4**), indicating that the addition of silver nanoparticles influences the material's stiffness. Moreover, PDMS-PSF-Ag displays an enhanced tensile strain ranging between 381 to 555% and a tensile strength of 0.28 to 0.31 MPa (**Table 4**), signifying improved mechanical properties with the addition of silver nanoparticles. Nonetheless, the piezoelectric coefficient of PDMS-PSF-Ag remains relatively low at 15 pmV⁻¹ to 17.7 pCn⁻¹ (**Table 4**), albeit showing some improvement compared to PDMS-PSF. Overall, these composite materials offer a blend of mechanical flexibility and piezoelectric functionality, making them promising candidates for applications in robotic artificial muscles.

Another composite, PDMS-Ag, solely incorporates silver nanoparticles into the PDMS matrix⁴⁸. This composite exhibits a E of 0.48 MPa (**Table 4**), closely resembling that of pure PDMS, indicating minimal influence on material stiffness due to the addition of silver nanoparticles. PDMS-Ag also demonstrates a tensile strain of 460% and a tensile strength of 0.51 MPa (**Table 4**), comparable to PDMS-PSF-Ag, albeit with a higher tensile strength. However, PDMS-Ag showcases a notably low d_{33} of 6 pmV⁻¹ and a dielectric constant of 5 (**Table 4**), suggesting limited piezoelectric responsiveness and dielectric properties. Furthermore, the strain amplitude is measured at 17.5% (**Table 4**), indicating the poor material's ability to deform under applied stress. Additionally, PDMS-Cl incorporates chloride ions into the PDMS matrix through solution casting⁴⁵. This composite displays a E of 0.21 MPa (**Table 4**), lower than when silver nanoparticles are added. Furthermore, PDMS-Cl exhibits a tensile strain and strength of 240% and 0.2 MPa (**Table 4**), respectively, which are lower compared to the addition of silver nanoparticles. Interestingly, the d_{33} of PDMS-Cl is 14 pmV⁻¹ (**Table 4**), more than twice that of PDMS-Ag, suggesting that the addition of chloride ions enhances piezoelectric responsiveness. Moreover, the dielectric constant increases to 24, indicating improved dielectric properties compared to PDMS-Ag. Overall, these findings suggest that while the addition of chloride ions may enhance piezoelectric and dielectric characteristics compared to the addition of silver nanoparticles in PDMS composites, neither PDMS-Ag nor PDMS-Cl exhibit properties robust enough for optimal performance in robotic artificial muscles.

PVDF stands out as the most renowned piezoelectric polymer, widely utilized in the fabrication of composite piezoelectric materials not only for its remarkable piezoelectric properties but also for its mechanical robustness. One such composite, PVDF-CN, incorporates carbon nanotubes within the PVDF matrix through electrospinning⁴², boasting a E of 17.2 MPa (**Table 4**), falling within the lower range of PVDF's modulus. However, PVDF-CN exhibits a lower tensile strain of 49.2% and a tensile strength of 4.20 MPa (**Table 4**) compared to pure PVDF, indicating reduced flexibility and stress resistance. Nevertheless, PVDF-CN demonstrates an enhanced d_{33} of 19 pCn⁻¹ (**Table 4**), surpassing that of pure PVDF. Another composite, PVDF-TrFE-MWCNT, integrates multiwalled carbon nanotubes and trifluoroethylene within the PVDF matrix, fabricated through electrospinning with additional methods such as annealing and drawing⁴⁹. This composite exhibits a significantly higher E of 986 MPa (**Table 4**) compared to PVDF alone, indicating increased stiffness. Moreover, PVDF-TrFE-MWCNT discloses an improved d_{33} of 50 pmV⁻¹ (**Table 4**), highlighting superior piezoelectric properties compared to pure PVDF. Furthermore, PVDF-BTO incorporates BTO into the PVDF matrix through non-solvent induced

phase separation⁴¹. This composite demonstrates an E between 120.1 to 206.7 MPa (**Table 4**), almost twice the highest value reported for pure PVDF. PVDF-BTO also exhibits impressive mechanical properties, including a tensile strain of 660 to 1000% and a tensile strength of 13.1 to 19.4 MPa (**Table 4**), indicating excellent flexibility and fracture resistance. However, its d_{33} ranges from 3.81 to 5.62 pmV⁻¹ (**Table 4**), falling within the lower range of PVDF coefficients. These findings underscore the potential of composite materials to enhance the mechanical and piezoelectric properties of PVDF for various applications, including robotic artificial muscles.

Additionally, PVDF has been combined with materials such as carbon fiber and Kevlar to enhance its mechanical resilience. The composite, PVDF-CF-Kevlar, was created by stacking different layers and melting the resultant structure for complete integration⁵⁰. Consequently, the material exhibits a remarkably high E of 16400 MPa, indicating significant stiffness. Nonetheless, its piezoelectric properties are notably poor⁵⁰, with a d_{33} of just 1.3 pCm⁻¹. Due to these inadequate piezoelectric properties, this composite material is not suitable for applications requiring robotic artificial muscles.

Moreover, two polymeric materials, PAN and PVDF, have been merged to improve both mechanical and piezoelectric properties. The resulting composite, PVDF-PAN, was fabricated using a solution casting approach with varying weight percentages of PVDF⁴³. PVDF-PAN demonstrates an E ranging from 2.56 to 4.24 MPa (**Table 4**), falling within the lower range of PVDF but slightly higher than that of PAN alone. Furthermore, PVDF-PAN exhibits a tensile strain of 90.7 to 135% and a tensile strength of 1.58 to 1.86 MPa (**Table 4**), comparable to PVDF but slightly lower. Notably, the piezoelectric coefficient of PVDF-PAN ranges from 14 to 30 pCm⁻¹ (**Table 4**), surpassing the values of PAN and PVDF alone, thus indicating improved piezoelectric properties. These findings highlight that the integration of multiple piezoelectric polymeric materials holds promise for enhancing both mechanical strength and piezoelectric performance. This approach demonstrates the potential of composite materials to achieve synergistic improvements in mechanical resilience and piezoelectric efficiency, particularly in applications such as robotic artificial muscles.

i-PP has also been utilized in the development of new piezoelectric composites. In this instance, particles of silicon oxide have been incorporated to enhance the piezoelectric properties using a cast extrusion method³⁴. The E of i-PP-SiO₄ is reported to range between 1068 and 1259 MPa (**Table 4**), a value similar to the E of the i-PP matrix, which is 1064 MPa. Other mechanical properties such as tensile strain (543 to 644%) and tensile strength (28.5 to 31 MPa) also closely resemble those of the matrix. Interestingly, the d_{33} has seen a significant improvement, increasing from the 14 pCm⁻¹ of pure i-PP to values around 80 to 200 pCm⁻¹ (**Table 4**) in the composite.

CS is another piezoelectric polymeric matrix that has been utilized in the fabrication of composite materials. In this particular case, zinc oxide nanoparticles have been incorporated to augment the piezoelectric properties. The CS-ZnO composite exhibits an E ranging from 4500 to 9090 MPa (**Table 4**), surpassing the 1700 MPa of chitosan alone (**Table 3**). Moreover, the d_{33} of CS-ZnO is notably higher, measuring between 60.6 and 65.9 pCm⁻¹ (**Table 4**), compared to the 12 pCm⁻¹ of pure CS. Additionally, the dielectric constant of the composite is elevated, with values ranging from 43 to 46.5 (**Table 4**), exceeding the value of 28 for chitosan alone.

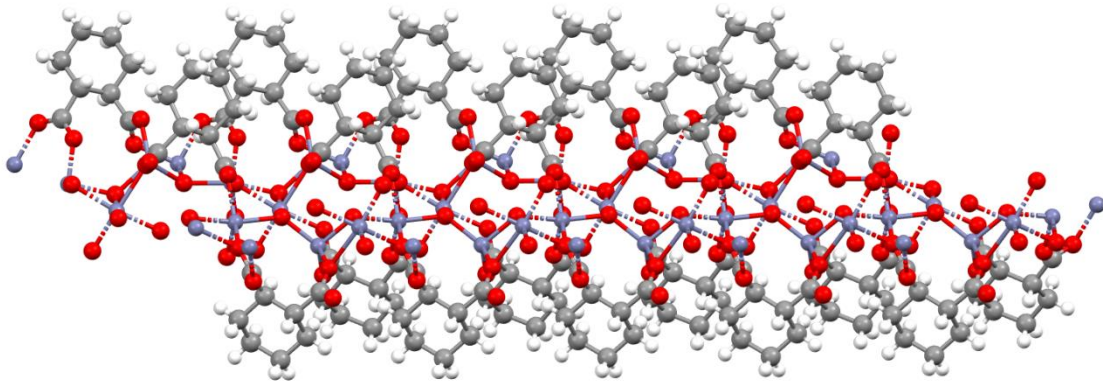


Figure 3. One-dimensional coordination polymer based on zinc and phthalic acid⁵². This diagram illustrates a one-dimensional coordination polymer formed by zinc ions and phthalic acid ligands. The Zinc ions (shown as blue spheres) are coordinated by the carboxylate groups of the phthalic acid molecules (depicted as red and grey sticks for oxygen and carbon, respectively), resulting in a chain-like structure. This polymer exemplifies the assembly of metal-organic frameworks through coordination bonds, highlighting the potential for creating extended networks with diverse functionalities.

Among the composites examined in this review, PDMS-PSF stands out with the lowest E of 0.11 MPa, although its piezoelectric coefficient is modest at $19 \text{ pC}\cdot\text{N}^{-1}$ (**Table 4**). The family of composites employing PDMS as the polymeric matrix collectively offers high piezoelectricity and flexibility, owing to its elevated piezoelectric coefficient and low E . Within this family, PDMS-BTO-MWCNT emerges as a notable candidate, maintaining a piezoelectric coefficient of $125 \text{ pC}\cdot\text{N}^{-1}$ (Table 4) while retaining a similar E of around 0.45 MPa (**Table 4**). Following closely is the PDMS-PTFE composite, exhibiting a piezoelectric coefficient of $106 \text{ pC}\cdot\text{N}^{-1}$ and a slightly lower E of approximately 0.37 MPa (**Table 4**).

2.2.4 Piezoelectric Coordination Polymers

CPs and metal-organic frameworks (MOFs) represent a new category of piezoelectric materials that hold significant promise for outperforming conventional ceramic piezoelectric materials. CPs are crystalline hybrid inorganic-organic materials composed of metal nodes and bridging organic linkers. They exhibit an unprecedented degree of structural diversity and chemical variability, allowing for substantial opportunities to tailor and tune their structures and properties to specific demands⁵¹.

The mechanical flexibility and piezoelectric properties of CPs and MOFs offer a mixed bag of advantages and disadvantages. The average E values of reported CPs and MOFs range from 500 to $57,700 \text{ MPa}$ ⁵¹, which is notably smaller than those of conventional oxides such as PZT ($64,000 \text{ MPa}$, **Table 2**) and BaTiO₃ ($67,000 \text{ MPa}$, **Table 2**). This reduction in modulus can be primarily attributed to the robust network connectivity within CPs, enhancing their ability to withstand uniaxial stress. However, when comparing the E values reported for CPs and MOFs to those of organic polymers, it becomes apparent that most organic polymers have inferior E values, with a few exceptions like PP and CS.

In terms of mechanical behavior, three-dimensional CPs and MOFs tend to exhibit low elastic anisotropy, meaning their mechanical properties are relatively uniform in all directions. However, this changes in low-dimensional CPs and MOFs, where high elastic anisotropy is observed. This arises from the weaker interactions between neighboring chains or layers, resulting in significantly lower elastic modulus values perpendicular to these structures compared to other orientations⁵¹.

Piezoelectric CPs and MOFs have shown piezoelectric coefficients ranging from 2.52 pCN⁻¹ for QMOF-2 to 60.1 pCN⁻¹ for Cd(Imazethapyr)₂⁵¹. Cd(Imazethapyr)₂, which crystallizes in a non-centrosymmetric space group Fdd2, displays a diamond-like three-dimensional structure. The piezoelectric coefficient of Cd(Imazethapyr)₂ is smaller than those of piezoceramics like BaTiO₃ (191 to 330 pCN⁻¹, **Table 2**) but higher than that of organic polymers such as PVDF (3.27 to 15.2 pCN⁻¹, **Table 3**). However, other organic polymers like PMDS, PLA, PP, XPP, and PVDF-TrFE can present piezoelectric coefficients up to ten times higher.

Another noteworthy example is the homochiral coordination polymer [Mn₂(D-cam)₂(2-Hpao)₄]_n, which not only presents a substantial piezoelectric coefficient of 6.9 pCN⁻¹⁵², but also showcases temperature-independent piezoelectric and dielectric characteristics, with its piezoelectric coefficient remaining almost constant even at temperatures up to 100°C.

Despite their promising potential, piezoelectric CPs often fall short in terms of *s* required for effective functioning as robotic artificial muscles. Skeletal muscles, for instance, boast an *E* reaching up to 60 MPa (**Table 1**), while even the lowest reported value for CPs stands at 500 MPa⁵¹, approximately eight times higher. This brittleness and rigidity inherent in CPs significantly restrict their ability to undergo substantial deformations. To address this limitation, embedding CPs within flexible organic polymeric matrices emerges as a viable solution. This hybrid approach serves to bolster their mechanical properties, providing the necessary flexibility and resilience for improved performance.

An exemplary instance of a composite material utilizing CPs involves the creation of a flexible composite device comprising thermoplastic polyurethane (TPU) integrated with varying weight percentages of a Zn(II)-based ferroelectric one-dimensional coordination network⁵³. This coordination network is derived from a flexible dicarboxylate ligand [PhPO(NH-(C₆H₄COOH))₂] (L1H₂) and 2,2'-bipyridine as a co-ligand. This specific one-dimensional coordination polymer exhibits a noteworthy converse *d*₃₃ value of 19.4 pmV⁻¹⁵³, as determined by piezoresponse force microscopy (PFM). The composite material was meticulously evaluated for its potential application as a piezoelectric nanogenerator. Particularly noteworthy is the performance of the champion device, which consists of a poled 5 wt.% 1-TPU composite. This device showcases an impressive open-circuit voltage of 5.6 V and a power density output of 14.6 μWcm⁻²⁵³. This groundbreaking research highlights the promising capabilities of such composite materials, bridging the gap between CPs and practical applications in energy harvesting and sensor technologies.

CPs and MOFs represent a burgeoning field of piezoelectric materials with unique advantages in structural diversity, chemical variability, and mechanical flexibility. While they face challenges in terms of *s* and mechanical robustness, ongoing research and hybrid material approaches continue to push the boundaries of their applications and capabilities.

2.3 Comparative Analysis

The comparative analysis of piezoelectric materials, illustrated in **Figure 4**, reveals distinct differences in the mechanical and piezoelectric properties of ceramics, polymers, and composites. Ceramics exhibit a broad range of *E* values, primarily spanning from 25,000 MPa to 150,000 MPa, and a corresponding piezoelectric coefficient mostly between 0 and 600 pCN⁻¹. This indicates that ceramics generally possess high stiffness and moderate piezoelectric response. In contrast, polymers show a significantly lower *E*, typically below 10,000 MPa, but their piezoelectric coefficients are concentrated around 0 to 300 pCN⁻¹, suggesting that polymers are more flexible but lower piezoelectric response compared to piezoceramics. Composites, which

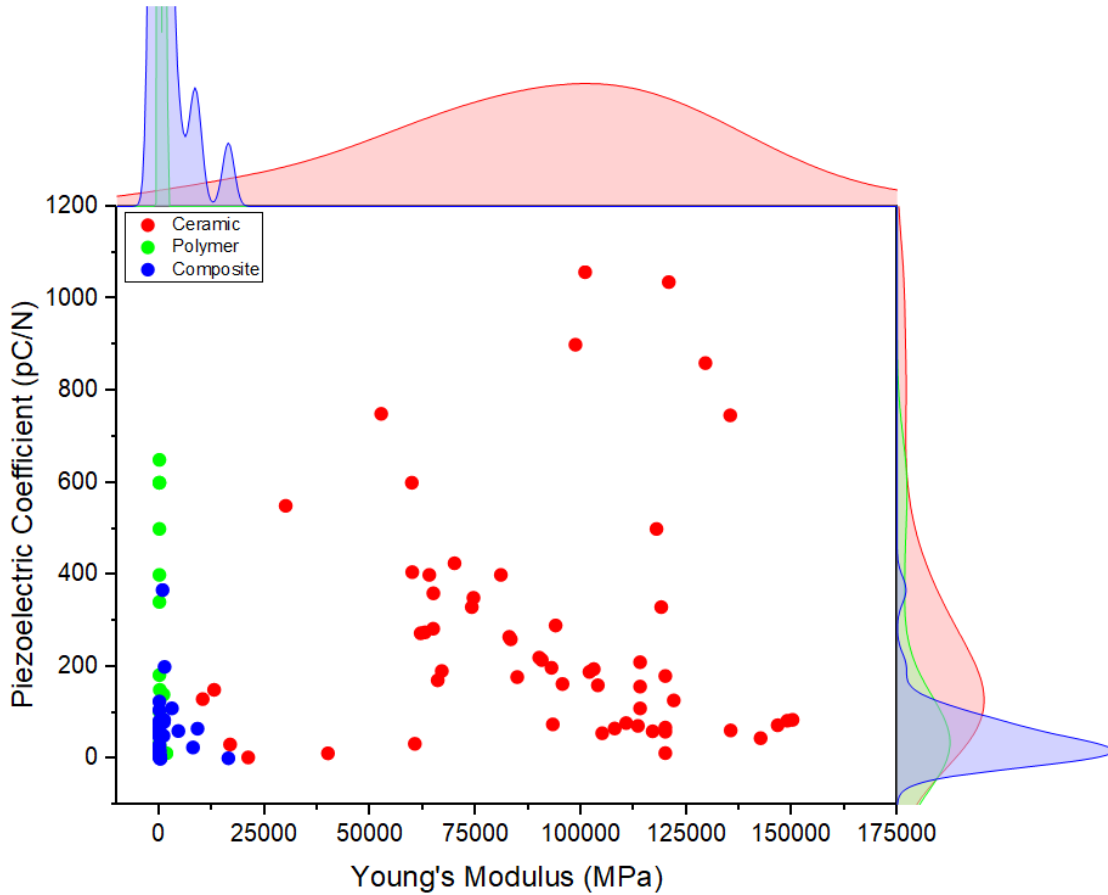


Figure 4. Comparative analysis of Young's modulus (MPa) and piezoelectric coefficient (pC/N^{-1}) for ceramic (red), polymer (green), and composite (blue) piezoelectric materials, with density plots illustrating distribution trends.

display similar ranges for both parameters to polymers, have E values mostly below 25,000 MPa and piezoelectric coefficients ranging from 0 to 180 pC/N^{-1} . The density plots further highlight the concentration trends, with ceramics predominantly in the higher modulus range and polymers in the lower modulus range, while composites exhibit a more similar distribution to polymers than to ceramics for both parameters. These findings underscore the distinct mechanical and piezoelectric characteristics of each material type, providing valuable insights for their potential applications in various technological fields.

Materials with the highest desirability in terms of E are found within the polymer category, where values go as low as 0.15 kPa (**Table 3**). This corresponds to an s value of 6667 MPa^{-1} (**Figure 5**) indicating their flexibility and adaptability. However, certain composite materials also present high s , but there are others that present much lower values, which are less favorable for applications requiring flexibility. Composite materials can also have high values as high as 9 MPa^{-1} (**Figure 5**), highlighting also their possible use. Conversely, ceramic materials, while possessing remarkable piezoelectric constants as high as 1058 pmV^{-1} (**Figure 5, Table 2**), are burdened with inherently stiff properties. Bulk ceramic materials, characterized by a minimum reported E of 10300 MPa (**Table 2**), are less desirable due to their lack of flexibility. Therefore, when prioritizing materials for the creation of robotic artificial muscles where suppleness is key, piezoelectric polymeric materials become the preferred choice. These materials offer the sought-after combination of low E values, alongside commendable piezoelectric coefficients of up to 650 pC/N^{-1} (**Table 1**), facilitating natural and fluid motion in artificial muscle systems. Furthermore, while the actuation strain values for polymers are not explicitly stated, they are expected to be comparable to those of composites due to the dominance of polymeric matrices in composite

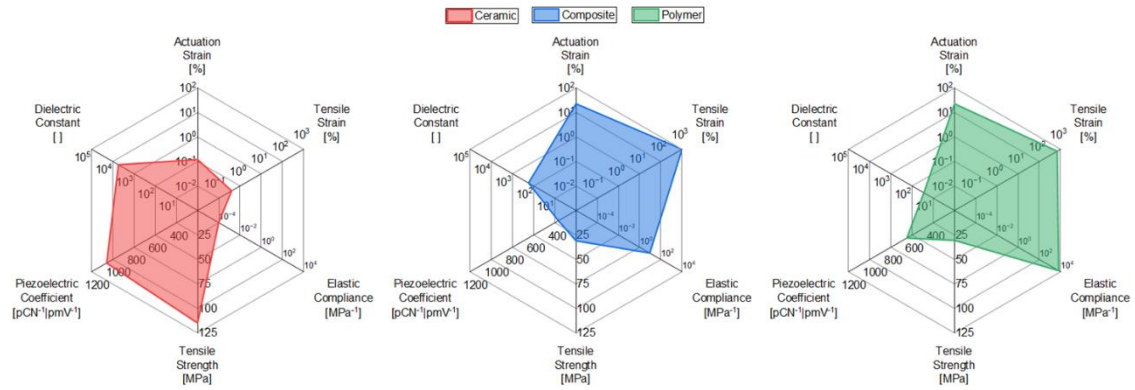


Figure 5. Logarithmic scale comparison of actuation strain, tensile strain, elastic compliance, tensile strength, piezoelectric coefficient, and dielectric constant for ceramic (red), polymer (green), and composite (blue) piezoelectric materials.

materials. Additionally, in terms of tensile strength, polymers and composites exhibit similar values, with a maximum tensile strength of about 31 MPa (**Figure 5**). Actuators made from high tensile strength materials offer robustness and resilience but often lack flexibility, while those with lower tensile strength provide greater adaptability and broader actuation ranges, crucial for effective robotic motion. However, piezoceramics, such as PZT, present significantly higher tensile strengths, reaching around 114.8 MPa⁵⁴, making them almost four times stronger than polymers and composites. In terms of tensile strain, PZT exhibits a value around 0.4%⁵⁴, whereas polymers and composites can reach up to 697 and 1000%, respectively. Actuators made from materials with high tensile strain at break values offer extended actuation ranges and robust performance, making higher tensile strain values preferable. Moreover, the dielectric constant of piezoceramics greatly exceeds that of polymers and composites, with values exceeding 5000, while polymers typically have dielectric constants around 28. With higher dielectric constants, these materials can store more electrical charge per unit volume at fixed voltages, leading to increased work densities; therefore, higher dielectric constants are desired. These comparisons highlight the multifaceted considerations involved in material selection for artificial muscle applications, with piezoelectric polymeric materials emerging as the optimal choice for balancing flexibility, strength, and piezoelectric performance.

In considering materials for mimicking the mechanical properties of natural skeletal muscles, it is crucial to focus on E , which typically ranges from 10 to 60 MPa (**Table 1**). Among the various material categories, polymeric and composite materials emerge as suitable candidates due to their comparable or lower E values. Notably, within the polymeric category, eight materials meet this criterion, including PVDF and its copolymers such as PVDF-TrFE, PVDF-TrFE-CTFE, as well as variants like CTFE-TrFE and TrFE-CTFE, alongside polymers like PDMS, IXPP, PLA, and PAN. Similarly, there are eleven composite materials identified, with ten out of the eleven incorporating a PDMS matrix, while the remaining composite employs PVDF as the matrix material. Given that over 90% of composites is conformed by the polymeric matrix¹⁹, it follows that the mechanical properties of the composite predominantly reflect those of the matrix material. However, the introduction of piezoceramics into the matrix can increase the E , resulting in increased stiffness. Additionally, considering the efficiency aspect, which is approximately 35% for natural skeletal muscles (**Table 1**), materials with higher piezoelectric coefficients are preferred for creating robotic artificial muscles. Among the polymeric materials, three exhibit notably high coefficients (**Table 3**): IXPP, PLA, and PDMS, with piezoelectric coefficients exceeding 300 pC/N⁻¹, albeit with some exceptions for PDMS. Furthermore, among the composite materials, two display relatively high values, albeit exceeding 100 pC/N⁻¹, namely PDMS-BTO-MWCNT and PDMS-PTFE (**Table 3**). These findings underscore the importance of carefully

selecting materials with suitable mechanical and piezoelectric properties for the development of biomimetic actuators and artificial muscles.

The values reported in reviews of robotic artificial muscles predominantly concern piezoceramics due to their widespread applications and notably high piezoelectric coefficients^{2,3,8}. High piezoelectric coefficients indicate the material's capability to efficiently convert electrical energy into mechanical energy³³. Consequently, **Table 1** demonstrates that piezoelectric actuators exhibit E values ranging from 10^3 to 10^5 MPa, which align closely with the values presented in **Table 2** for piezoelectric ceramics. Given their high piezoelectric coefficients, it is unsurprising that these actuators achieve efficiencies exceeding 90%. Conversely, while piezoelectric polymers are more flexible and exhibit lower E values, their piezoelectric coefficients (**Figure 5**), though lower, still facilitate efficient energy conversion, enabling them to attain high levels of efficiency as well. Moreover, the significantly lower dielectric constants of piezoelectric polymers compared to piezoceramics influence the work density of these materials. Additionally, some composite piezoelectric materials can achieve actuation strain values up to 22%, whereas piezoelectric actuators generally exhibit actuation strains of less than 2% as indicated in reviews (**Table 1**). This underscores the importance of considering piezoelectric polymer materials over piezoceramics when comparing different artificial muscle technologies. Consequently, the use of piezoelectric polymers can offer significantly more advantages than those highlighted in current reviews.

However, the use of piezoelectric polymer materials as robotic artificial muscles also brings some limitations. The piezo mechanism's efficiency is hindered by the requirement of high electric fields, typically around 1 kVmm^{-1} , which are often substantial⁵⁵. While piezoceramics rely on electric fields for charge polarization, polymeric types often exhibit natural polarization, obviating the need for polarization processes. Nonetheless, achieving significant actuation necessitates high voltages, raising safety concerns and demanding complex electrical systems⁵⁵. Despite their potential for efficient conversion of electrical to mechanical energy, piezoelectric materials can incur high energy consumption due to their reliance on elevated operating voltages and continuous energy input for displacement maintenance. Actuation strains in piezoelectric materials tend to be modest, typically below 2% (**Table 1**), with limited evidence supporting substantial actuation strains in some piezoelectric composites. This restricted deformation capacity stands in contrast to other actuator materials like SMAs or DEAs. While piezoelectric ceramics are susceptible to brittleness and fracture under mechanical stress or cyclic loading, piezoelectric polymers mitigate this risk at the expense of reduced piezoelectric coefficients. Additionally, their performance can be sensitive to temperature variations, which can adversely affect their piezoelectric properties and mechanical integrity⁵⁶.

Chapter 3: Materials and Methodology

3.1 Coordination Polymer Synthesis

3.1.1 Reagents and Materials

The coordination polymer synthesis utilized zinc nitrate as the source of Zn metal ions due to its availability and minimal health risks. Zinc nitrate is a commonly used Zn source because it is easily obtainable and poses fewer health hazards compared to other Zn compounds. Two ligands, 2-methylimidazole (2-MI) (see **Figure 6a**) and cinnamic acid (CA) (see **Figure 6b**), were selected based on their previous successful use in forming non-centrosymmetric CPs and their availability.

2-MI was chosen for its well-documented ability to form CPs. Specifically, it has been used to create structures such as catena-(pentakis(μ -2-methylimidazolato)-(2-methylimidazole)-triazinchemikis(2-methylimidazole)hydrate)⁵⁷ (code name IWOZOL) (see **Figure 7a**) and catena-(bis(μ -2-methylimidazolato)-zinc)⁵⁸ (code name YUDWEB) (see **Figure 7b**). In these polymers, 2-MI acts as a bridging ligand, coordinating through both nitrogen atoms. This dual coordination ability enhances the stability and complexity of the resulting polymer structures. Additionally, imidazole (see **Figure 6c**), a structurally similar compound, contributes to the chirality in CPs, such as catena-((μ -2-Succinato)-bis(1H-imidazole-N₃)-zinc(ii))⁵⁹ (see **Figure 7c**). These examples demonstrate the versatility and effectiveness of imidazole-based ligands in forming diverse coordination polymer frameworks.

CA was also employed as a ligand due to its proven efficacy in forming CPs. An example of this is the polymer catena-((μ -2-cinnamato-O,O')-(cinnamato-O)-(methyl 3-pyridylcarbamate)-zinc(ii))⁶⁰ (see **Figure 7d**). CA contributes to the coordination environment by offering oxygen donor sites that can coordinate with metal ions, thereby forming stable polymeric chains. The selection of CA is further justified by its availability and its ability to introduce additional functional groups into the polymer structure, potentially enhancing the material's properties.

To dissolve CA, which is not very soluble in water, ethanol at a concentration of 70 wt.% was used as the solvent. Ethanol is an effective solvent for CA and helps in achieving a homogeneous solution necessary for the synthesis of the coordination polymer. Additionally, ethanol is highly effective at dissolving the other ligand, 2-MI. The use of ethanol also ensures that the coordination polymer synthesis occurs under relatively mild and non-toxic conditions.

The anticipated structure of the coordination polymer, as depicted in **Figure 6d**, presents a detailed illustration of the spatial arrangement and interactions between Zn ions and various ligands within the polymer matrix. In this design, each Zn ion is coordinated by a single 2-MI ligand. This specific ligand is chosen due to its ability to induce chirality within the polymer. Chirality is a critical feature as it ensures that the resulting polymer is non-centrosymmetric. A non-centrosymmetric structure is essential for the manifestation of piezoelectric properties. Furthermore, CA serves a dual role in this coordination polymer. It acts as a bridging ligand, linking two Zn ions together. The structural design intends for CA to facilitate a one-dimensional coordination polymer, where the polymer chain extends linearly in a single direction. This unidirectional extension is significant because it can influence the mechanical properties of the polymer, potentially enhancing its *s*.

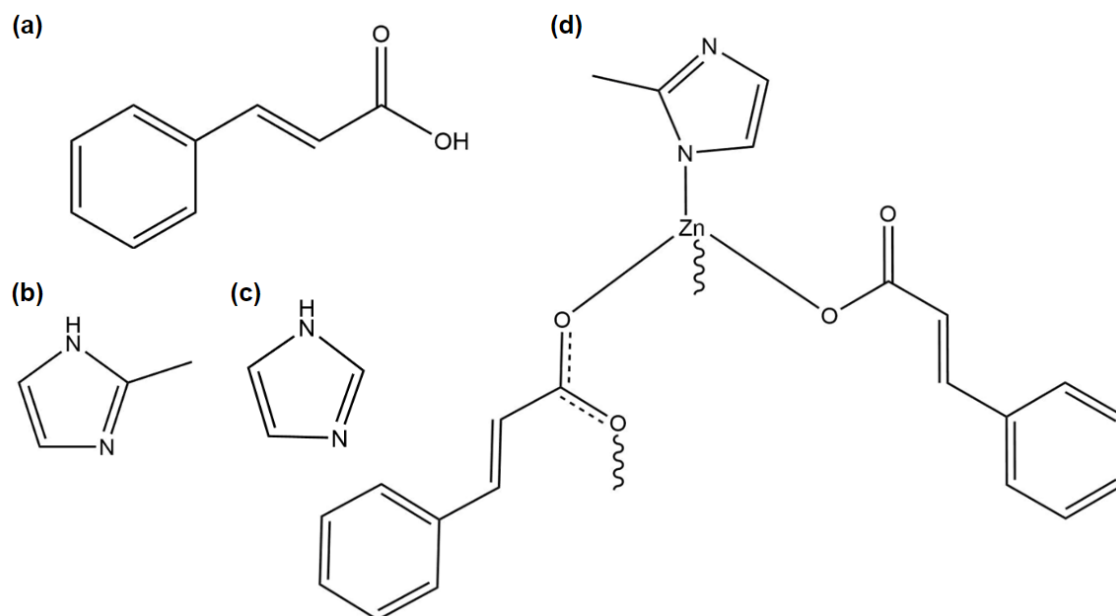


Figure 6. Chemical structures of the ligands **(a)** cinnamic acid, an organic compound with a phenyl group attached to a three-carbon chain terminating in a carboxylic acid, **(b)** 2-methylimidazole, a heterocyclic aromatic organic compound with a methyl group at the second position of the imidazole ring, and **(c)** imidazole, a simple heterocycle with two nitrogen atoms. **(d)** The proposed coordination polymer, which possesses a non-centrosymmetric structure.

The careful selection and arrangement of these ligands—2-MI for chirality, and CA for one-dimensional polymer growth—reflect a deliberate strategy to optimize the functional properties of the coordination polymer. This design not only contributes to the fundamental understanding of coordination chemistry but also opens avenues for developing advanced materials with tailored properties for actuation applications.

3.1.2 Synthesis Procedure

Initial synthesis attempts employed equal stoichiometry of the ligands using both one-pot solution and hydrothermal methods. Due to solubility issues with CA, the one-pot method, which provides a faster and more efficient route, was selected for subsequent synthesis. This method also allowed better control over reaction parameters, such as pH and coordination time, which are critical for ligand coordination. The reaction was carried out at ambient temperature to simplify the experimental setup and maintain a constant, non-variable temperature. This decision was made to ensure consistency across experiments and avoid introducing additional variables. The reaction time was set to 30 minutes to provide sufficient time for thorough mixing and interaction between the reagents, ensuring complete coordination while minimizing the formation of byproducts.

In the individual ligand coordination stage, we analyzed the impact of specific parameters, such as pH, temperature, and coordination time, to optimize the process. NaOH was introduced to adjust the pH of the solution, as maintaining an optimal pH was critical for effective ligand coordination. Previous studies have shown that a basic environment enhances the deprotonation of carboxyl groups⁶¹, which is essential for successful coordination with metal ions.

After optimizing the parameters for individual ligand coordination, simultaneous coordination of both ligands was performed. Various stoichiometries and NaOH concentrations were tested to achieve different pH levels, based on literature suggesting that controlling the pH allows for fine-tuning of coordination geometry and crystal structure⁶². The basic protocol involved dissolving

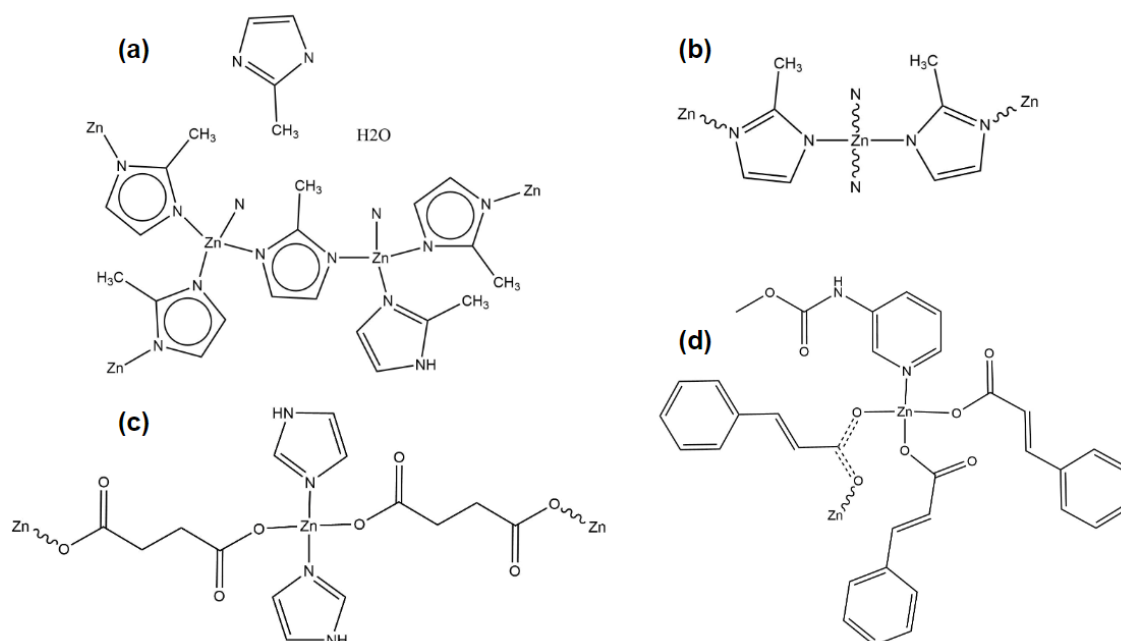


Figure 7. Chemical structures and coordination polymers involving zinc ions with various ligands: **(a)** Coordination complex featuring 2-methylimidazole ligands and zinc ions, including uncoordinated 2-methylimidazole molecules, adapted from Chen et al.⁵⁷ **(b)** Coordination compound with 2-methylimidazole ligands bridging zinc ions, adapted from Fujie et al.⁵⁸ **(c)** Coordination structure involving imidazole and zinc ions, adapted from Demir et al.⁵⁹, and **(d)** Coordination structure incorporating cinnamic acid ligands and zinc ions, adapted from Zelenak et al.⁶⁰.

each reagent in the solvent, mixing, and stirring for approximately 30 minutes. This time frame was selected based on empirical tests and previous reports indicating it was sufficient for complete dissolution and reaction progress⁶³. After stirring, vacuum filtration was employed to collect the precipitate, which was then washed and dried.

Additionally, NaCIN was synthesized by reacting CA with NaOH to control the pH of the solution. A pH of 9.34 was achieved to ensure complete deprotonation of carboxylic acid groups, which is necessary for the subsequent coordination steps. The resulting NaCIN was lyophilized and characterized using infrared spectrograph analysis, confirming the success of the reaction and its suitability for further use in the synthesis process.

A graphical representation of the synthesis protocol can be seen in **Figure 8**.

3.1.3 Characterization

The first method to characterize the samples was powder X-ray diffraction (XRD). This technique compared the characteristic peaks of the sample to a wide library of diffraction patterns, including those in the crystallography open database (COD) and the Cambridge structural database (CSD). Data collection was performed using a Rigaku Miniflex-600 powder diffractometer equipped with a D/tex Ultra2 detector. The X-ray generator was operated at 40 kV and 15 mA with a sealed tube CuK α radiation source. Data collection utilized a $\theta/2\theta$ configuration in the scan axis, with a 0.02° step and a scan velocity of $20.0^\circ/\text{min}$ over a range of $5-90^\circ$ in 2θ . The D/tex Ultra2 detector was used in one-dimensional scan mode. Additionally, the setup included a Soller slit at 1.25° for receive and incident scattering, and high length receiving and incident slits of 10.0 mm, 8.0 mm, and 13.0 mm, respectively.

To analyze the diffraction patterns, Match! software was employed for phase analysis. This user-friendly software compares the diffraction pattern of the sample to a database of reference patterns, facilitating the identification of the present phases. Additionally, it was used to compare different samples, providing insights into the synthesized materials.

For indexing powder diffraction data, the auto-indexing program DICVOL was employed, as detailed in the reference by Boulton and Louër⁶⁴. The efficacy of this program is evaluated using figure of merit (*FoM*) M20, a standard measure in crystallography for assessing the quality of the indexing, as described by de Wolff⁶⁵. Following the initial indexing, the lattice parameters were further refined using the Le Bail method, a robust technique for extracting accurate unit cell parameters from powder diffraction data, as explained by Le Bail et al.⁶⁶. This comprehensive approach ensures precise and reliable determination of the crystal structure.

Fourier transform infrared spectroscopy (FTIR) was also used to identify functional groups in the ligands and to compare them to those in the samples to determine any changes due to coordination with the metal ion. The FTIR spectra were obtained using a Perkin Elmer Spectrum two infrared spectrometer. This instrument features a medium-range Fourier transform and a standard MIR lithium tantalate (LiTaO₃) detector, along with a deuterated triglycine sulfate (DTGS) MIR detector. It has a standard optical system with KBr windows for data collection in a spectral range of 8,300 to 350 cm⁻¹, with an optimal resolution of 0.5 cm⁻¹. Additional specifications include ZnSe windows for data collection in a spectral range of 6000 to 550 cm⁻¹, and a diamond ATR accessory covering a range from 4000 to 650 cm⁻¹. The spectrometer operates over a pH range of 1 to 14 and includes automatic recognition and safety screw features. Atmospheric steam compensation (AVC) standard with automatic performance verification absolute virtual tool (APV/AVI) configuration was also employed, all controlled via Spectrum 10 software.

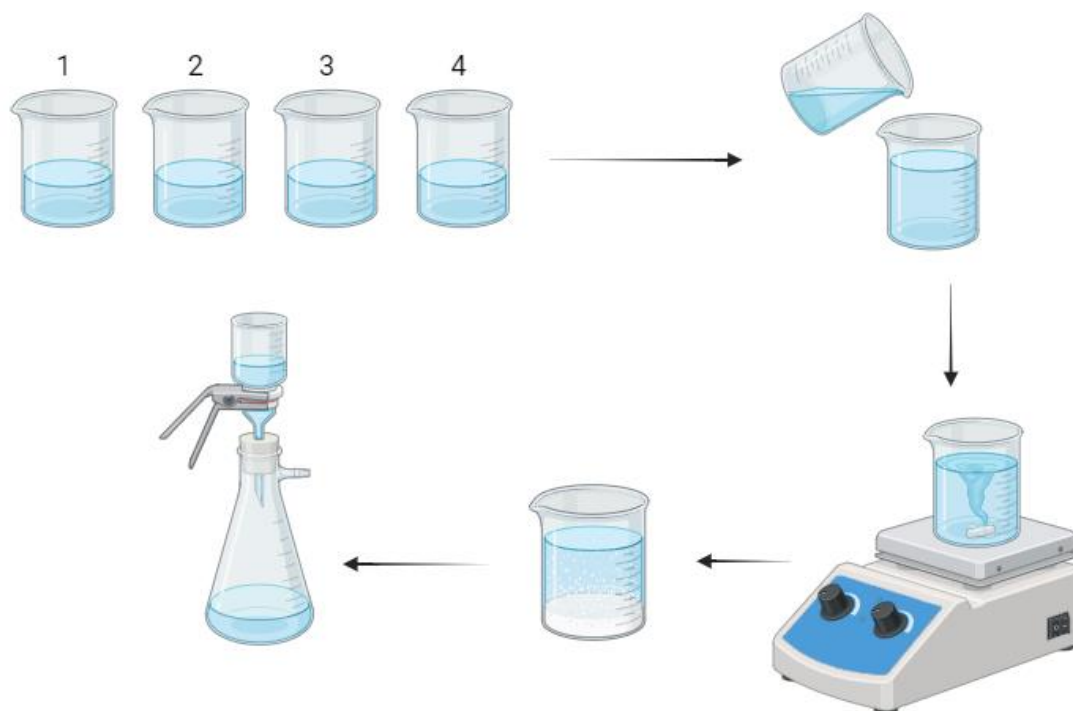


Figure 8. The basic protocol for synthesizing the coordination polymer involves the following steps: (1) Dissolving each reagent in the solvent in separate beakers, (2) Combining the solutions into a single beaker, (3) Mixing and stirring the combined solution for approximately 30 minutes on a magnetic stirrer, and (4) Using vacuum filtration to collect the resulting precipitate.

3.2 Composite Formation

3.2.1 Composite Samples

PLA was selected as the polymeric matrix for the composite due to its known piezoelectric properties and favorable mechanical characteristics, particularly its s value. PLA's proven piezoelectric properties make it an ideal candidate for this study. Additionally, its mechanical properties, including flexibility and strength, further support its suitability for creating a durable composite material.

The PLA used in this study was obtained in the form of filament typically used in 3D printing. It is important to note that this form of PLA is not pure; it includes pigments for color and other additives to enhance its printing performance. These additives can potentially influence the material's properties, making it essential to carefully consider their impact during the preparation and analysis of the composite.

To prepare the composite, the PLA filament was dissolved in tetrahydrofuran (THF). The choice of THF was based on its ability to effectively dissolve PLA, creating a homogeneous solution (as seen in **Figure 9a**) necessary for the subsequent steps in the composite preparation process. The dissolution process was conducted at a temperature of 100°C, which is close to PLA's melting temperature of approximately 150°C. Conducting the dissolution near this temperature ensures that the PLA dissolves more efficiently and thoroughly, resulting in a uniform solution that can be used to form the composite material.

Furthermore, the weight ratio of the polymer to the solvent was maintained at 10 wt.% to ensure proper solvation of the polymer. This specific ratio was chosen to balance the viscosity of the solution, facilitating better handling and casting, while ensuring complete dissolution of the PLA. **Figure 9a** shows that the solution is homogeneous and an ideal film. This meticulous approach to the dissolution process is crucial for achieving a consistent and high-quality composite material.

After dissolving the coordination polymer in powder form, it was added to the solution at a concentration of 0.5 wt.%. This solution preparation step is crucial for ensuring an even distribution of the coordination polymer throughout the polymer matrix. The solvent, used to dissolve both the polymer and the coordination polymer, was then evaporated (see **Figure 9a** and **Figure 9b**), a technique known as solution casting. Solution casting involves pouring the prepared solution into a mold or onto a flat surface and allowing the solvent to gradually evaporate. This controlled evaporation process leads to the formation of a uniform polymer composite film. The entire process is illustrated in **Figure 10**.

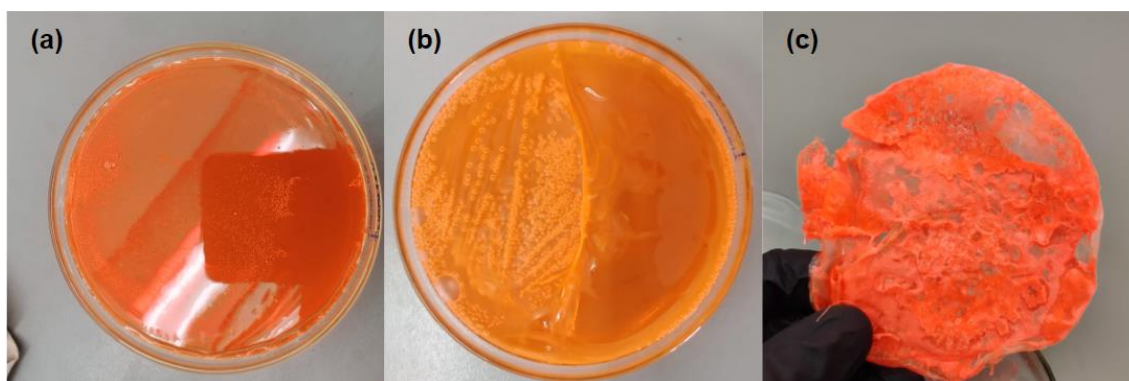


Figure 9. Sequential stages of solvent evaporation: (a) Solution before evaporation, (b) Solution with solvent partially evaporated, and (c) Completely evaporated solvent, resulting in the final solid product.

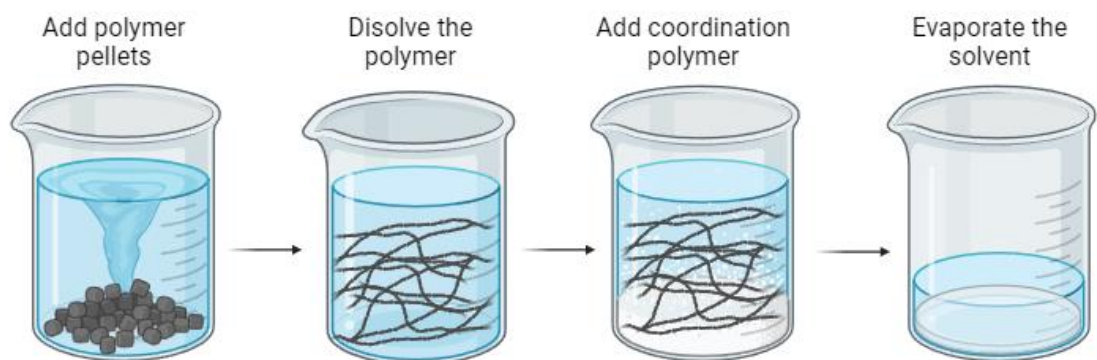


Figure 10. These steps illustrate the process sequence: polymer pellets are added initially, followed by dissolution of the polymer. Subsequently, coordination polymer is introduced, and finally, solvent evaporation completes the processing.

To ensure that the surface of the resulting film was smooth and homogeneous, the film underwent compression molding with a heated plate press. The setup is depicted in **Figure 11a**. The temperature of the heating plates was precisely set to 150°C, the melting temperature of PLA. Heating the film to this temperature ensures that the PLA melts and flows, allowing for the even distribution of the coordination polymer within the matrix.

During the compression molding process, the material was subjected to a pressure of 2 metric tons. This significant pressure, applied for approximately 4 minutes, ensures that the film is properly compressed, eliminating any voids or air bubbles that might have formed during the solution casting phase. The combination of heat and pressure helps to achieve a dense and uniform composite material. After the compression molding step, the material was quickly cooled with cold water. This rapid cooling, also known as quenching, helps to lock the polymer chains in place, preserving the composite structure and preventing any phase separation or crystallization that might occur if the material were cooled slowly.

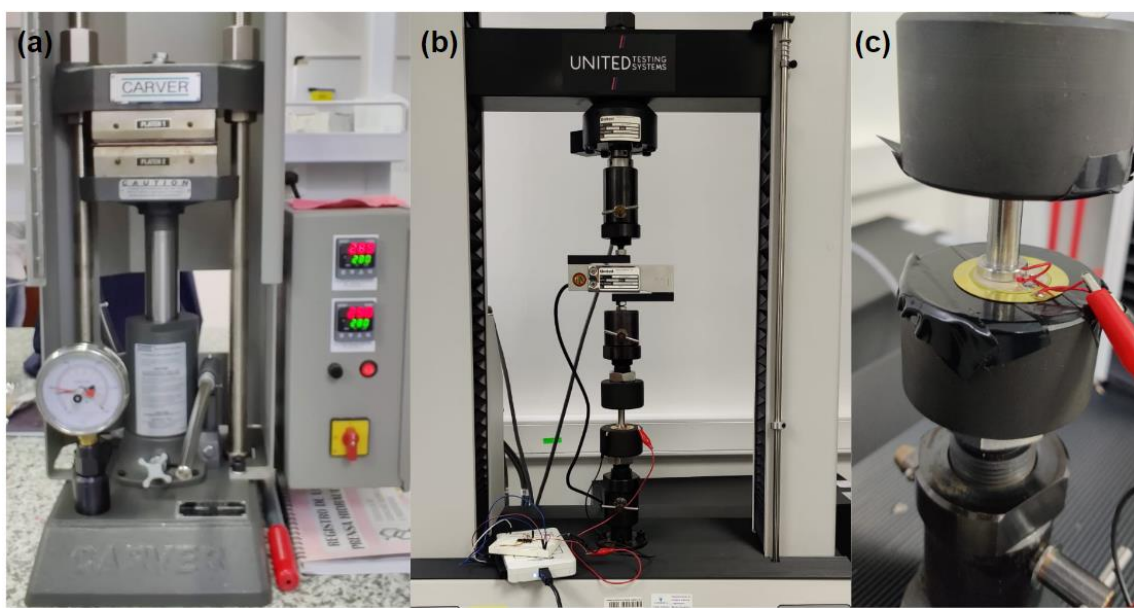


Figure 11. Overview of the experimental setup: (a) A press with heating plates used for the composite material processing. (b) The system employed to measure piezoelectric properties, comprising a data acquisition system, a charge amplifier, and a universal testing machine. (c) A close-up view of the piezoelectric material within the setup.

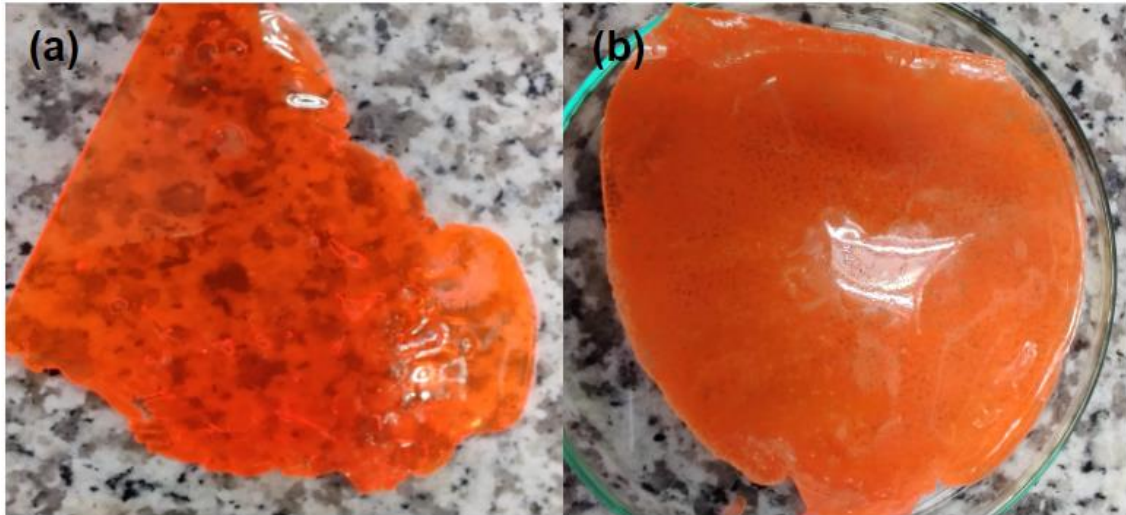


Figure 12. Comparison of materials: **(a)** The processed PLA blank sample. **(b)** The composite material containing 5 wt.% of the coordination polymer.

Additionally, for comparative purposes, blank samples of PLA without the coordination polymer were prepared using the same compression molding technique. This allows for a direct comparison between the piezoelectric properties of the composite material and the pure PLA. An image of both the blank sample and the composite material is provided in **Figure 12**, clearly showing the physical characteristics and surface quality of each sample. The preparation of these blank samples is critical for understanding the impact of the coordination polymer on the material's properties, ensuring that any observed effects can be attributed to the presence of the coordination polymer rather than differences in processing or material handling.

3.2.2 Characterization

The piezoelectric properties of the materials were characterized using a data acquisition system (NI MyDAQ) seen in **Figure 13a** and a custom-made charge amplifier, as described by Tsai et al.⁶⁷. A schematic representation of the electronic circuit used for these measurements can be seen in **Figure 14a**, which illustrates the actual circuit used, alongside **Figure 14b** a representation of the charge amplifier circuit, which employs an operational amplifier (Op-Amp) for signal amplification and conditioning. The data recording and analysis were performed using MyDAQ

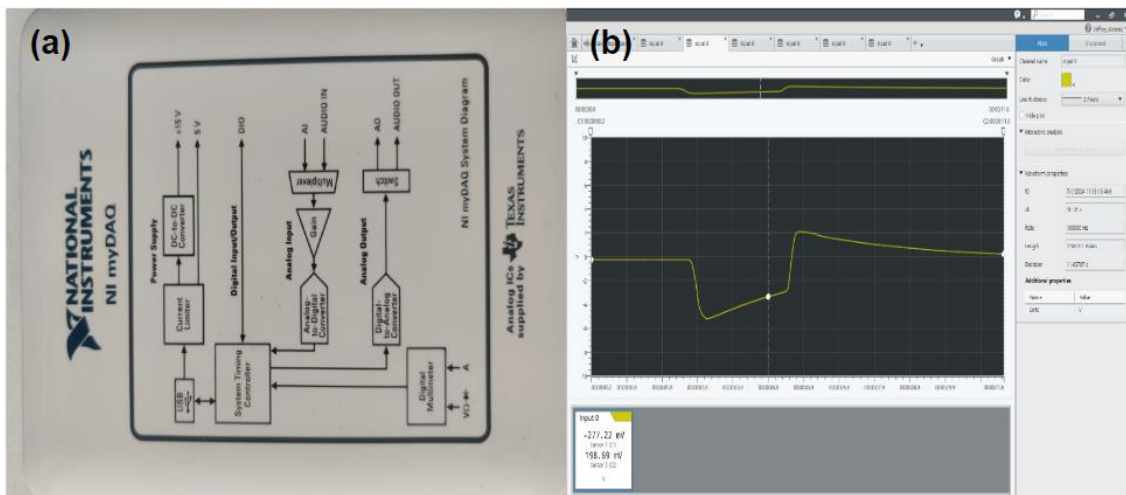


Figure 13. Overview of the setup: **(a)** NI MyDAQ data acquisition system by National Instruments. **(b)** MyDAQ Express interface used for controlling the DAQ.

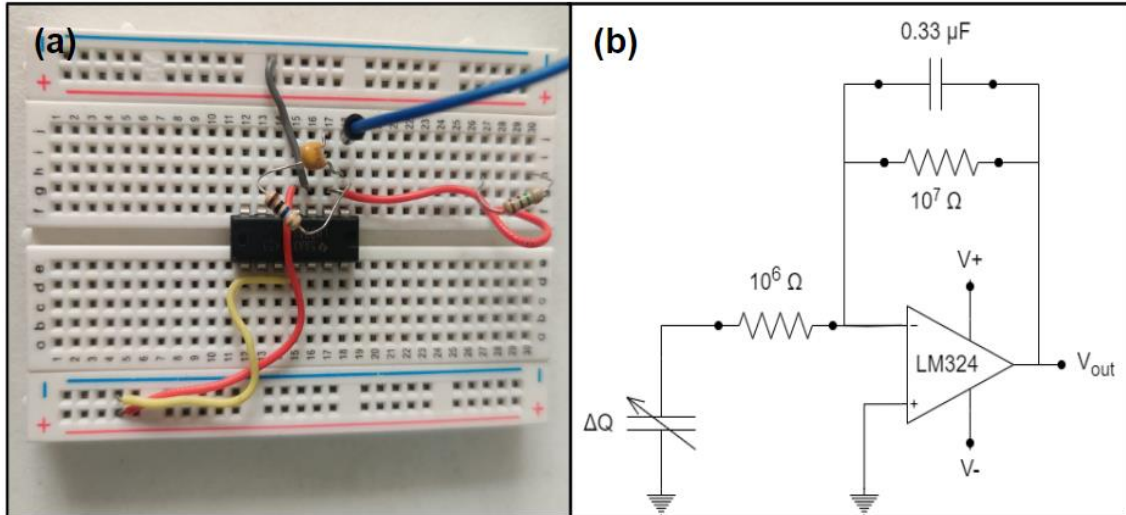


Figure 14. Illustration of the experimental setup: **(a)** Schematic representation of the electronic circuit used for measurements, illustrating the actual circuit configuration. **(b)** Representation of the charge amplifier circuit used in the measurements.

Express software, which is illustrated in **Figure 13b**. To validate the charge amplifier circuit, initial measurements were taken from commercially available PZT materials, such as piezoelectric buzzers (illustrated in **Figure 11c**). These measurements ensured that the charge amplifier circuit was functioning correctly before testing the samples.

For the samples, silver conductive paint (see **Figure 15b**) was applied as the upper and lower electrodes. This paint was acquired from Mechanic, and it has a viscosity of 20000 Mpa, a resistance of less than 15 mΩ, and a Rockwell hardness greater than 2 H. A graphical representation of the electrode setup is shown in **Figure 15a**, with real images of the PLA blank sample shown in **Figure 15c** and composite films in **Figure 15d**, prepared for testing their piezoelectric properties.

The samples were subjected to various loads to simulate different force levels. The electric charge (Q) was obtained from the output voltage (V_{out}) of the charge amplifier, following the relationship of **Equation 1**, where 0.33 μF is the capacitance of the reference capacitor in the charge amplifier circuit. This capacitor, in conjunction with the charge amplifier circuit, serves to isolate the capacitance of the piezoelectric material, the wires, and other parasitic capacitances. Therefore, the reference capacitance is the primary contributor to the resultant voltage, simplifying the calculation of the electric charge.

$$Q = V_{out} \cdot 0.33 \quad (1)$$

The equipment used to apply the controlled forces was a universal testing machine for deformation resistance provided by the United Testing System (see **Figure 11b**). Although this equipment was not suitable for providing small incremental changes in force, it could apply a range of forces that were recorded during testing. This limitation did not hinder the tests, as it was only necessary to record the forces applied by the equipment each time. The primary constraint was that the material could not be tested multiple times with the exact same force.

Despite this limitation, the testing method allowed for the characterization of the piezoelectric properties of the materials under various load conditions. The precise control and measurement of applied forces ensured that the data collected was reliable and could be used to draw meaningful conclusions about the piezoelectric behavior of the samples. This experimental setup, including the use of a universal testing machine and a validated charge amplifier circuit, provided a robust

framework for evaluating the piezoelectric properties of the blank polymer and the composite material.

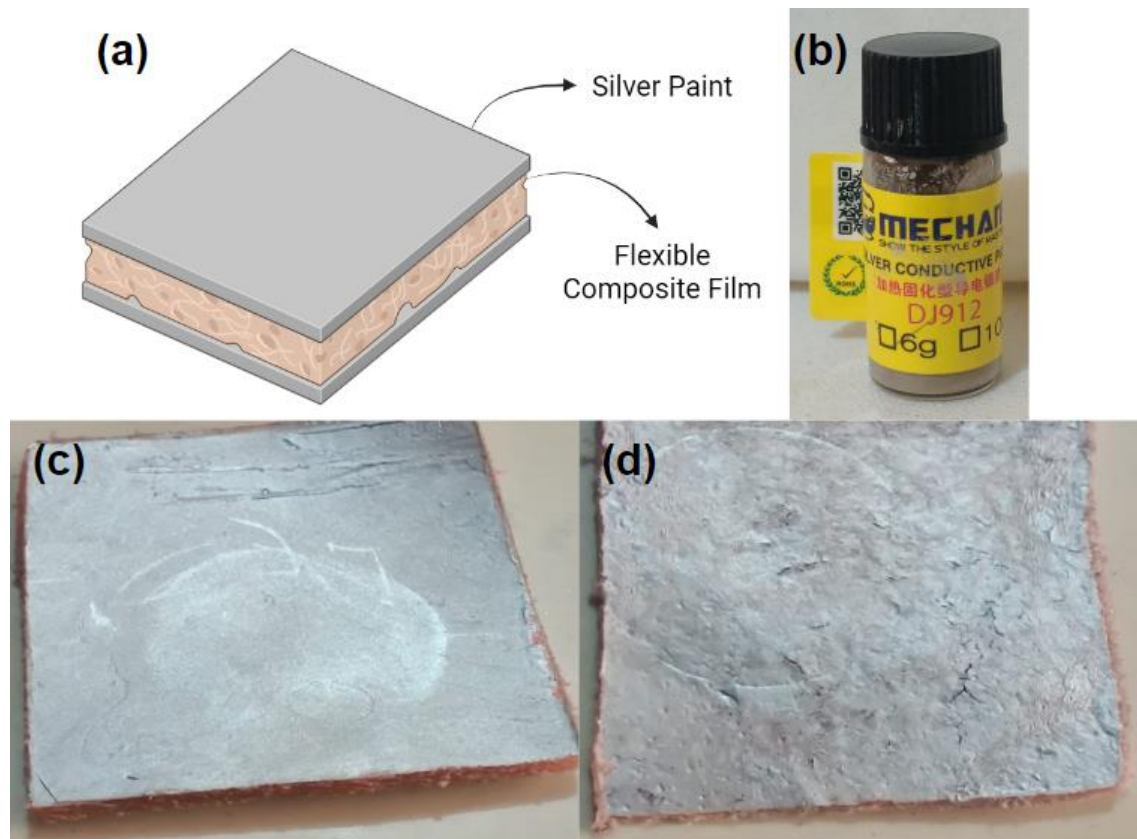


Figure 15. Overview of the experimental process: **(a)** Graphical representation of the electrode setup. **(b)** Application of Mechanic brand silver conductive paint. **(c)** PLA blank sample with applied electrodes. **(d)** Composite film with applied electrodes.

Chapter 4: Results and Discussion

4.1 Coordination Polymer Synthesis

4.1.1 Initial Synthesis and Characterization of Coordination Polymers

Initial explorations for the synthesis of the proposed coordination polymer involved creating samples CP-003 and CP-005 using hydrothermal and one-pot methods, respectively. Both samples maintained the same ligand-to-zinc ion ratio, and crystallographic analysis showed diffraction peaks corresponding to the compound *cis*-diaqua-bis(*trans*-cinnamato-O,O')-zinc(II) (**Figure 16**) as reported by Hosomi et al.⁶⁸. The diffraction patterns of both samples were similar in peak positions and intensities, though CP-005 exhibited a higher intensity peak at 27.66 2 θ (**Figure 17**). This indicates that, despite different synthesis methods (**Table 5**), the final crystallographic structure remained consistent. In both samples, CA coordinated with the zinc ion, while 2-MI did not, with water instead coordinating with zinc (see **Figure 16**). This suggests that the coordination behavior of 2-MI requires further investigation for successful integration into the polymer.

The FTIR analysis, depicted in **Figure 18**, supports these findings by showing that both CP-005 and CP-003 yielded the same molecular structure. The FTIR spectra displays similar peak positions at wavenumbers such as 1646, 1578, 1498, 1447, 1261, 1208, 1070, 1033, 988, 975, 877, 852, 771, 753, 715, and 682 cm⁻¹, indicating the identical molecular structure of both samples. However, differences in peak intensities, with CP-003 generally showing higher transmittance, suggest variations in crystallinity, particle size, or sample purity. These findings confirm that although the synthesis methods varied, the structural outcome was identical, albeit with different physical characteristics.

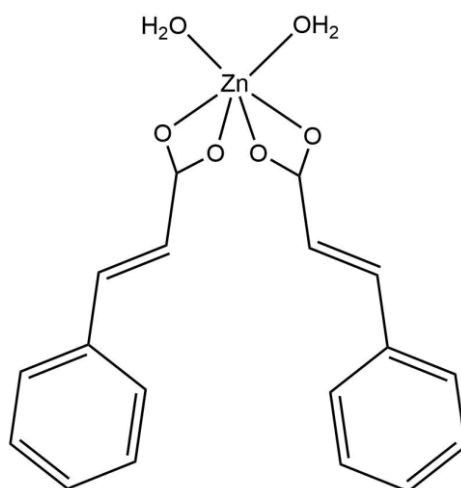


Figure 16. Molecular structure of *cis*-diaqua-bis(*trans*-cinnamato-O,O')-zinc(II)⁶⁵.

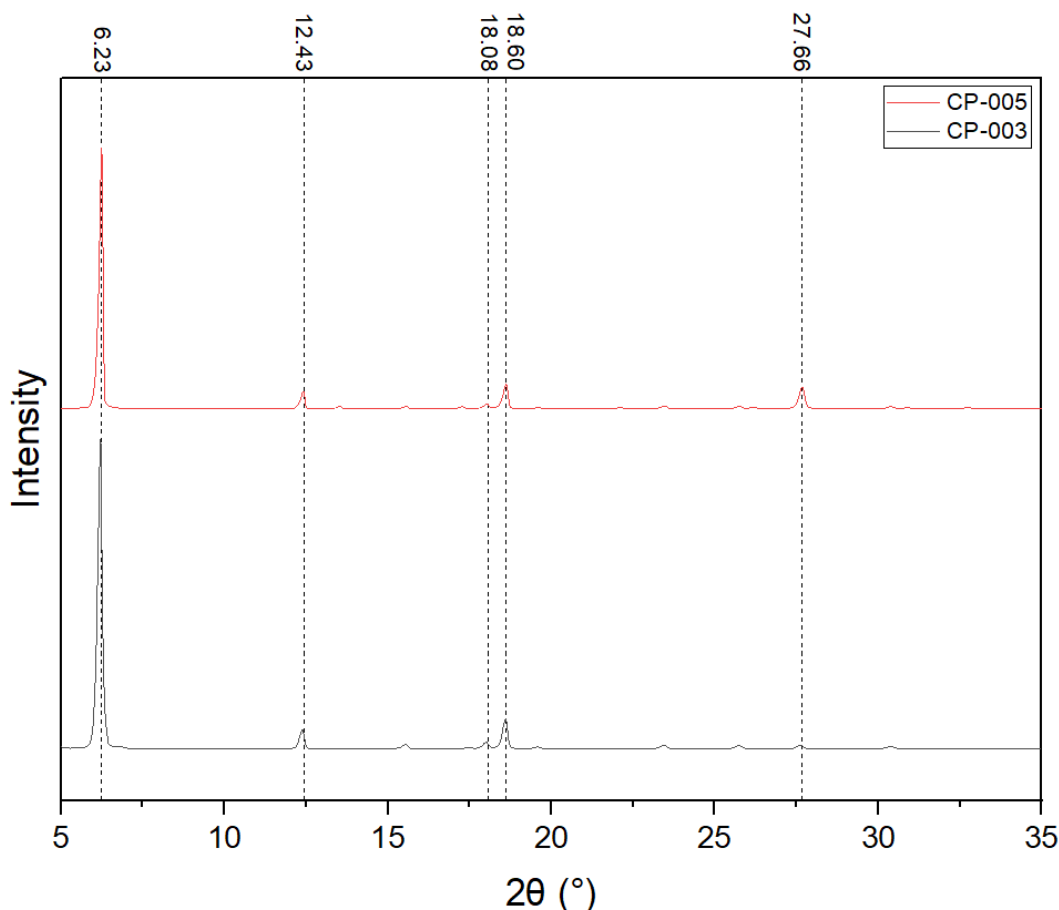


Figure 17. X-ray diffraction pattern of samples CP-005 (red) and CP-003 (black), showing similar peak patterns.

Table 5. Stoichiometric data, synthesis methodologies, and outcomes from the crystallographic analysis of initial explorations.

Sample	Stoichiometry		Synthesis Method	Crystallographic Analysis
	2-MI:Zn	CA:Zn		
CP-003	1.0	1.0	Hydrothermal	cis-Diaqua-bis(trans-cinnamato-O,O')-zinc(ii)
CP-005	1.0	1.0	One-Pot	cis-Diaqua-bis(trans-cinnamato-O,O')-zinc(ii)

4.1.2 Individual Coordination of Cinnamic Acid and 2-Methylimidazole

To determine the necessary parameters for successful ligand coordination, individual coordination of each ligand was attempted. For CA, the one-pot method was used, resulting in samples CP-006 and CP-009 with stoichiometric ratios of 1:1 and 6:1 for CA to zinc, respectively, synthesized at pH levels 3.53 and 3.30 (Table 6). Crystallographic analysis showed that CA dissolved and recrystallized without coordinating with zinc, likely due to the acidic pH. Thus, NaOH was introduced in subsequent synthesis to regulate pH levels. The unsuccessful coordination at acidic

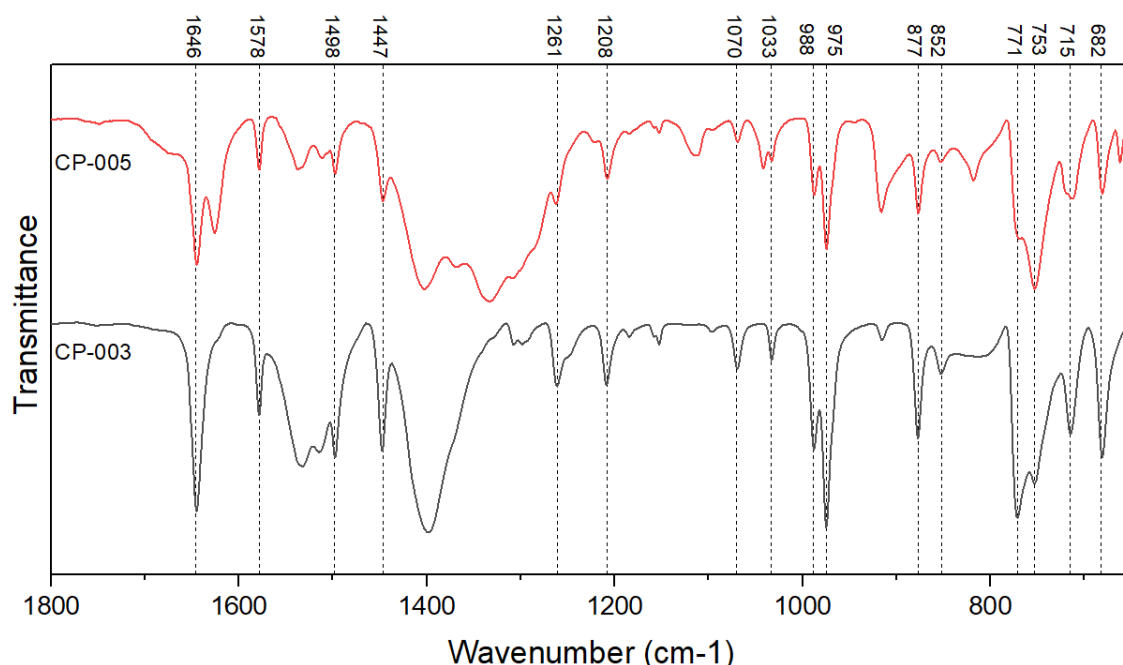


Figure 18. Fourier transform infrared spectroscopy of samples CP-005 (red) and CP-003 (black), showing similar peak patterns.

pH highlighted the need for a basic environment to facilitate effective ligand binding, as the carboxylate groups of CA require deprotonation to interact with zinc ions.

Table 6. Stoichiometric data, synthesis methodologies, and outcomes from the crystallographic analysis of the coordination of cinnamic acid.

Sample	Stoichiometry		pH	Synthesis Method	Crystallographic Analysis
	CA:Zn				
CP-006	1.0		3.53	One-Pot	Cinnamic Acid
CP-009	6.0		3.30	One-Pot	Cinnamic Acid

In **Figure 19**, the FTIR results show identical peaks for CA and samples CP-006 and CP-009, indicating that CA did not coordinate with zinc and retained its original structure. This further supports the crystallographic findings that the acidic conditions were not conducive to coordination. Additionally, in **Figure 21**, the DRX results showed identical peaks for both samples, reinforcing that no new crystalline phase formed involving zinc coordination under these conditions. These findings underscore the importance of pH in the synthesis process and suggest that future experiments should focus on creating a more basic environment to achieve successful ligand coordination with zinc ions.

For the individual coordination of 2-MI, stoichiometric ratios for 2-MI to Zn were kept constant at 2.0 while varying NaOH ratios to 1.0 and 2.0, resulting in pH levels of 7.84 and 13.77, respectively (**Table 7**). Crystallographic analysis identified two different materials: IWOZOL⁵⁷ for sample CP-012, where 2-MI coordinated mostly by one nitrogen, and YUDWEB⁵⁸ for sample CP-013, where 2-MI coordinated by both nitrogen atoms. Higher pH levels facilitated deprotonation of the nitrogen atoms, allowing them to coordinate with zinc. This indicated that

the basic environment provided by NaOH was crucial for achieving the desired coordination, as it enhanced the nucleophilicity of the nitrogen atoms in 2-MI, making them more available for binding to zinc ions.

Table 7. Stoichiometric data, synthesis methodologies, and outcomes from the crystallographic analysis of the coordination of 2-methylimidazole.

Sample	Stoichiometry		pH	Synthesis Method	Crystallographic Analysis
	2-MI:Zn	NaOH:Zn			
CP-012	2.0	1.0	7.84	One-Pot	IWOZOL
CP-013	2.0	2.0	13.77	One-Pot	YUDWEB

The FTIR spectra presented in the **Figure 20** demonstrate the vibrational changes of 2-MI (2-MI) upon coordination with Zn ions in samples CP-012 and CP-013, which have pH levels of 7.84 and 13.77, respectively. The pure 2-MI spectrum shows distinct peaks at 1302, 1153, and 1113 cm^{-1} . In CP-013, the peaks are steeper and more distinct compared to CP-012, though not as sharp as in pure 2-MI, indicating more effective coordination at the higher pH. The peaks for both samples are shifted to higher wavenumbers, reflecting the coordination of the carbon-nitrogen (C-N) bonds to the Zn atoms, which compresses the bonds and alters the energy absorbed. The weaker, broader peaks in CP-012 suggest incomplete coordination and the presence of multiple components, including uncoordinated 2-MI and nitratine, consistent with powder DRX findings. These results highlight the significant influence of pH on the coordination efficiency, with higher pH promoting more complete coordination of 2-MI to Zn ions.

The powder XRD patterns for samples CP-012 and CP-013 (**Figure 22**) reveal significant differences in their crystalline structures. CP-013, with a pH of 13.77, exhibits sharp and intense peaks, indicating a highly crystalline and well-ordered structure. In contrast, CP-012, with a pH

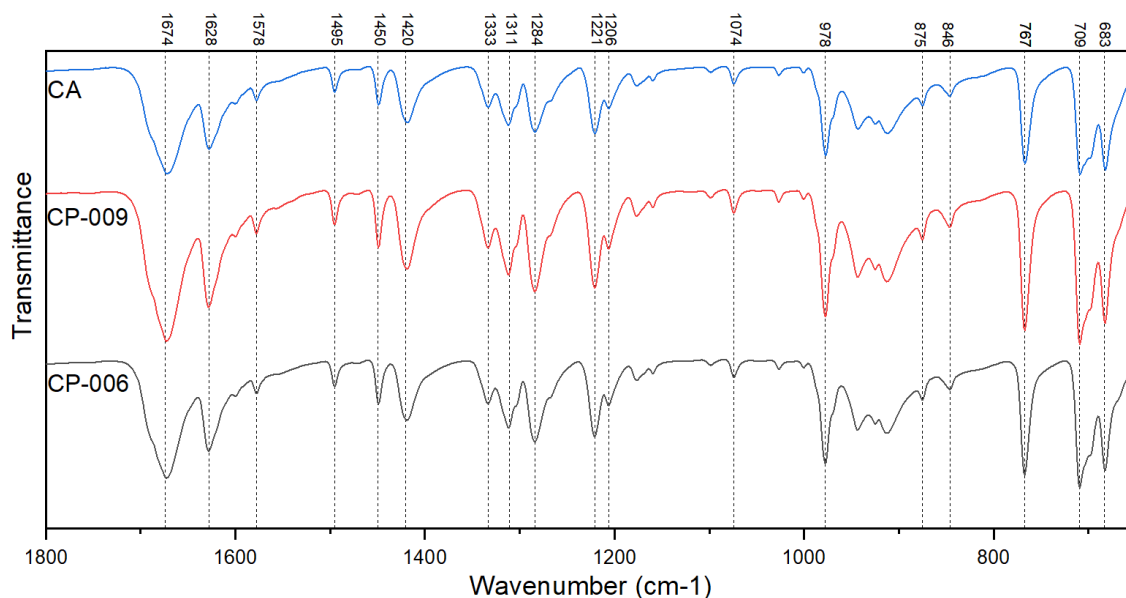


Figure 19. Fourier transform infrared spectroscopy of samples CP-009 (red) and CP-006 (black), compared to cinnamic acid (blue), showing identical patterns.

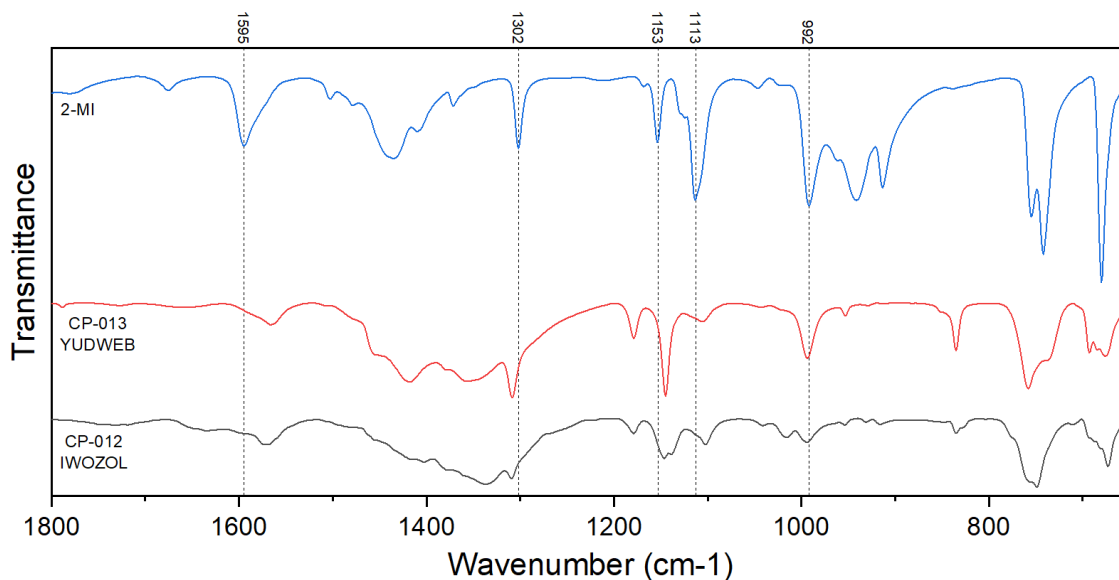


Figure 20. Fourier transform infrared spectroscopy of samples CP-013 (red) and CP-012 (black), compared to 2-methylimidazole (blue), showing some similarities among the three.

of 7.84, shows broader and less intense peaks, suggesting a lower degree of crystallinity and a mixture of phases. Both samples share peaks at similar 2θ values, indicating common crystalline phases resulting from the coordination of 2-MI with Zn ions. The higher crystallinity of CP-013 is likely due to more effective and complete coordination of the 2-MI ligand at the higher pH,

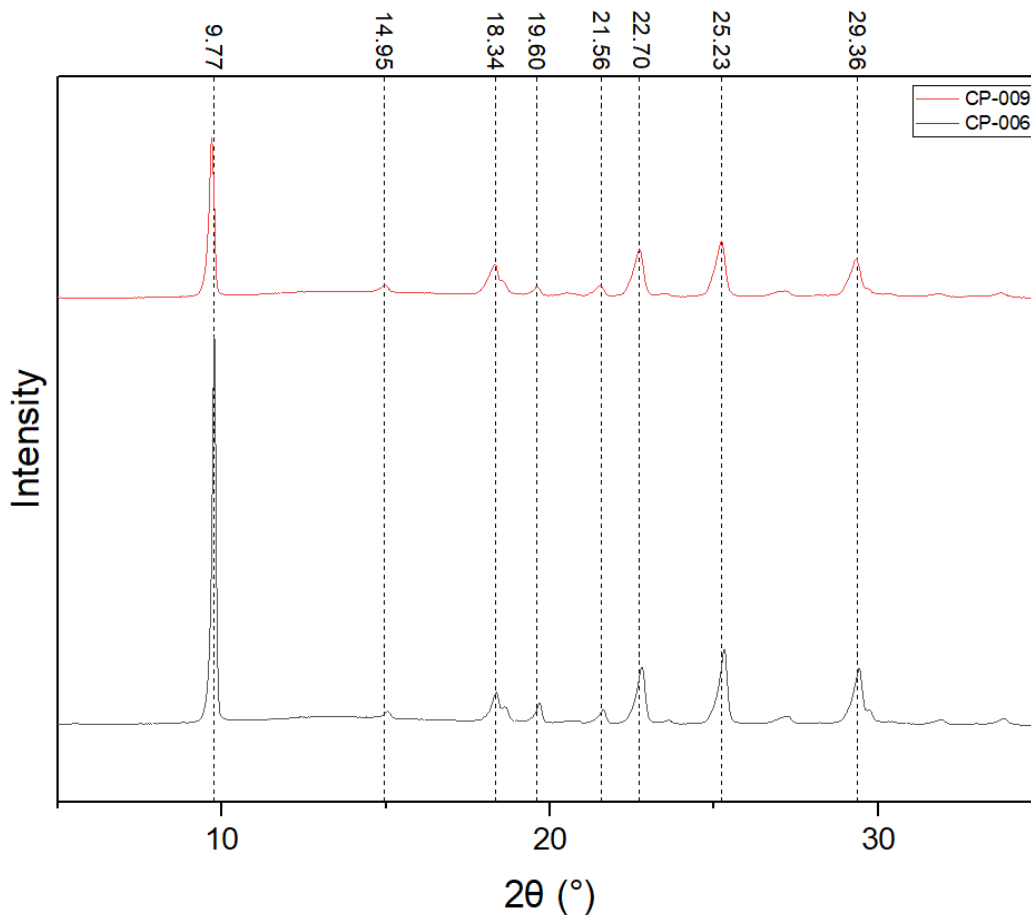


Figure 21. X-ray diffraction pattern of samples CP-009 (red) and CP-006 (black), showing similar peaks with an increase in intensity.

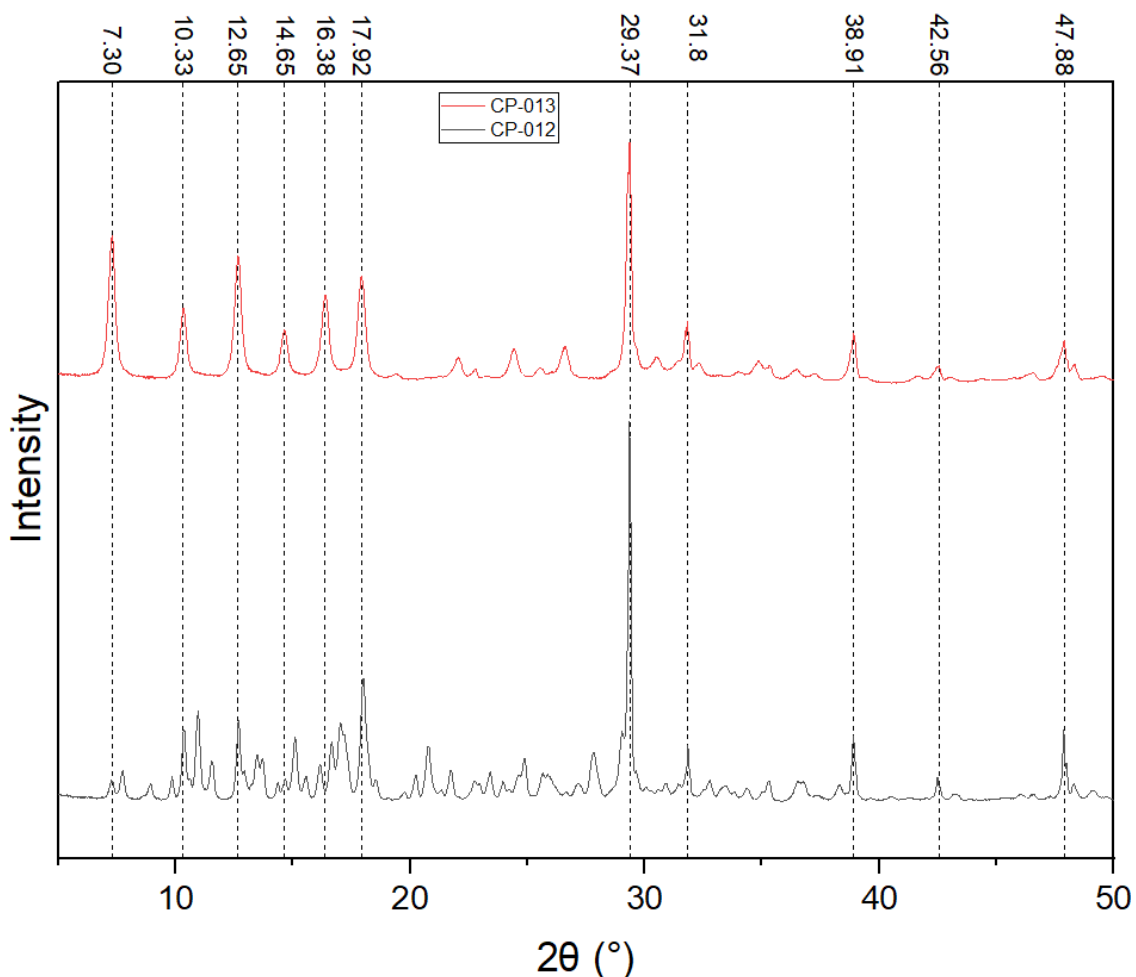


Figure 22. X-ray diffraction pattern of samples CP-013 (red) and CP-012 (black), showing similar peaks, with sample CP-012 displaying more noise due to higher impurity levels.

leading to a more crystalline product. This is consistent with the FTIR analysis, which also highlighted the impact of pH on the coordination and structural properties of the samples.

4.1.3 pH Effects on Ligand Coordination

Subsequent synthesis attempts included coordination of both ligands, with NaOH controlling pH levels. Five samples (CP-018, CP-020, CP-0121, CP-022, CP-028) were synthesized with various stoichiometric ratios (**Table 8**), highlighting the importance of the NaOH-to-zinc ratio in determining pH levels (as shown in **Figure 23**). Crystallographic analysis revealed that pH levels around 8 led to the formation of compound IWOZOL, while higher pH values around 13 led to the formation of YUDWEB. Lower pH levels below 8 produced unidentified compounds, indicating potential new compounds. The variation in crystallographic outcomes based on pH underscored the delicate balance required to achieve successful coordination, with basic conditions favoring 2-MI coordination and neutral to slightly acidic conditions hindering it.

Table 8. Stoichiometric data, synthesis methodologies, and outcomes from the crystallographic analysis of the subsequent synthesis.

Sample	Stoichiometry			pH	Synthesis Method	Crystallographic Analysis
	2-MI:Zn	CA:Zn	NaOH:Zn			
CP-018	2.0	1.0	2.0	8.25	One-Pot	IWOZOL
CP-020	1.1	0.6	1.1	6.94	One-Pot	No Identified
CP-021	2.0	1.0	3.0	13.50	One-Pot	YUDWEB
CP-022	2.0	2.0	3.0	8.40	One-Pot	IWOZOL
CP-028	1.0	0.5	1.0	7.36	One-Pot	No Identified

4.1.4 Infrared Spectroscopic Analysis of CP-020

After conducting the crystallographic analysis of samples CP-020 and CP-028, an additional study using the FTIR results was performed. Since there were no differences in the characteristic peaks between the two samples (**Figure 24**), the subsequent analysis focused solely on sample CP-020.

Therefore, CP-020 was compared to a synthesized sample of NaCIN. The FTIR spectra, shown in **Figure 25**, revealed two characteristic peaks present in both NaCIN and CP-020 at 1521 and 1417 cm^{-1} for CP-020, and at 1546 and 1405 cm^{-1} for NaCIN (**Table 9**). These peaks near 1500

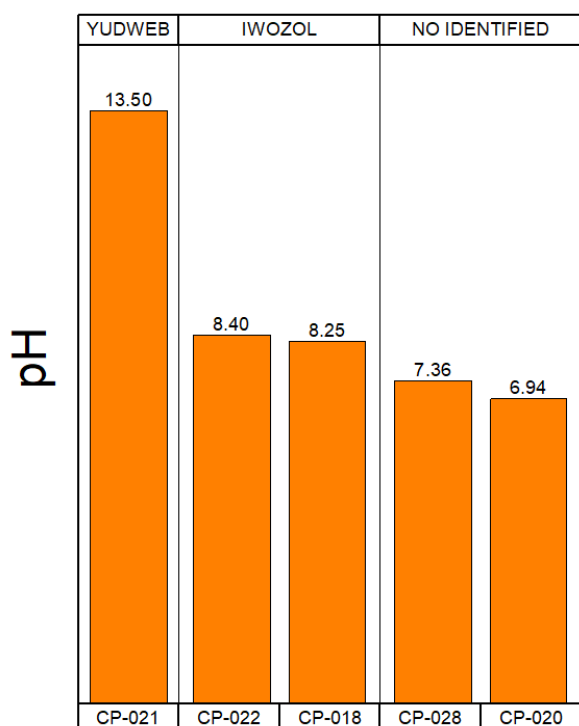


Figure 23. Influence of pH on the type of compound identified for samples CP-021, CP-022, CP-018, CP-028, and CP-020.

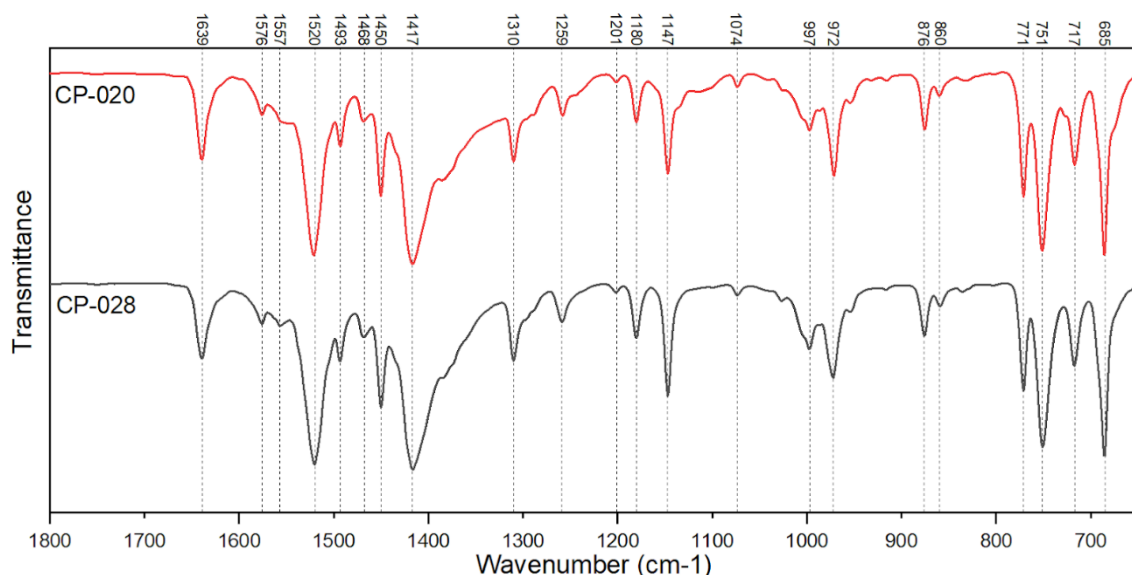


Figure 24. Fourier transform infrared spectroscopy of samples CP-020 (red) and CP-028 (black), showing similar peak patterns.

cm^{-1} are attributed to the asymmetric stretching vibration of the carboxylate anion, while those near 1400 cm^{-1} are due to the symmetric stretching vibration of the carboxylate anion.

It has been reported that the coordination mode of the carboxylate anion can be inferred from the difference between the asymmetric and symmetric stretching vibrations. If this difference is smaller in the sample than in NaCIN, the coordination is bidentate; otherwise, it is monodentate⁶⁰. For CP-020, the difference is 104 cm^{-1} , compared to 141 cm^{-1} for NaCIN (see **Table 10**), indicating that the CA in CP-020 has a bidentate coordination mode.

Table 9. Identification of key FTIR peaks in sample CP-020 and their correlation with sodium cinnamate.

Peak	Vibration	Related From
1521 cm^{-1}	$\nu_{\text{as}}(\text{O-C-O})^-$	NaCIN
1417 cm^{-1}	$\nu_{\text{s}}(\text{O-C-O})^-$	NaCIN

Table 10. Analyzing and contrasting FTIR peaks in sample CP-020 with those of sodium cinnamate.

Sample	$\nu_{\text{as}}(\text{C-O-C})^-$	$\nu_{\text{s}}(\text{C-O-C})^-$	$\Delta\nu = \nu_{\text{as}} - \nu_{\text{s}}$
NaCIN	1546 cm^{-1}	1405 cm^{-1}	141 cm^{-1}
CP-020	1521 cm^{-1}	1417 cm^{-1}	104 cm^{-1}

Further comparisons using FTIR, depicted in **Figure 25**, reveal that NaCIN and CP-020 exhibit several shared peaks, notably at 1639 , 1575 , 1494 , 1450 cm^{-1} , and additional lower wavenumber peaks. This confirms structural similarities between them.

Sample CP-020 was also compared to CP-013, a previously identified compound where 2-MI successfully coordinated with zinc. This comparison served to identify functional groups in CP-020 that corresponded to 2-MI ligands. **Figure 26** shows that CP-020 shares three distinct peaks with CP-013 at 1310 , 1180 , and 1147 cm^{-1} (**Table 11**), correlating with the stretching vibration of an amine group (C-N). This indicates the presence of 2-MI in CP-020.

Further FTIR results comparing CP-020 to pure 2-MI, shown in **Figure 28**, reveal that the peaks in 2-MI are shifted to higher wavenumber values in CP-020. This shift indicates higher energy

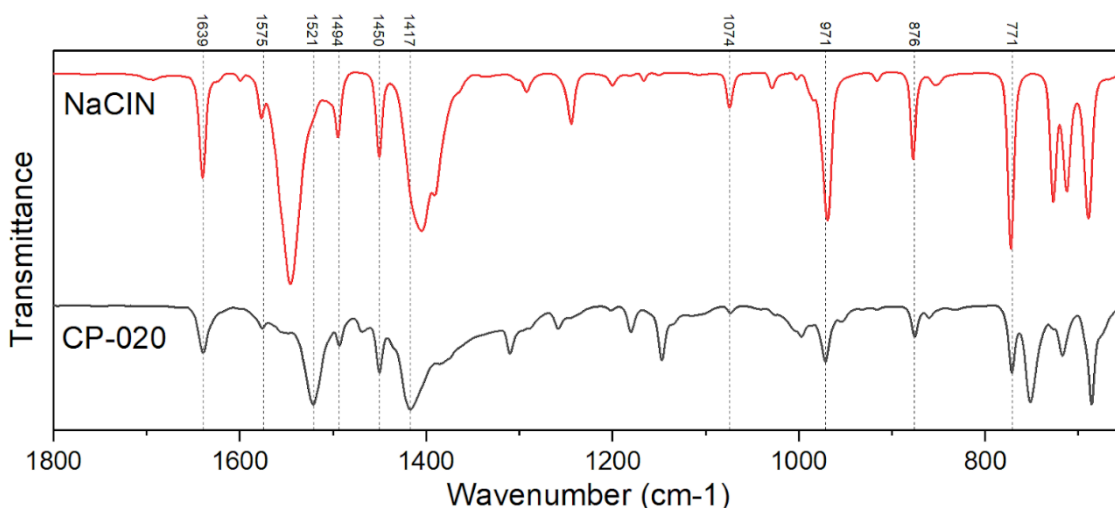


Figure 25. Fourier transform infrared spectroscopy of sodium cinnamate (red) and sample CP-020 (black), showing similar peak patterns at higher wavenumbers than 1400 cm^{-1} and lower than 1100 cm^{-1} .

bonds in CP-020. The energy of chemical bonds is related to the frequency of their associated waves: higher frequencies correspond to higher energy levels. Since frequency is directly proportional to wavenumber, a higher wavenumber also indicates higher energy. **Table 12** provides detailed information about the wavenumber of each peak and its difference when compared to the peaks of 2-MI. The differences range from 8 to 34 cm^{-1} , indicating an increase in bond energy, likely due to stiffening of the carbon-nitrogen (C-N) bonds caused by compression from the Zn atom.

Table 11. Identification of key FTIR peaks in sample CP-020 and their correlation with sample CP-013.

Peak	Vibration	Related From
1310 cm^{-1}	$\nu(\text{C-N})$	CP-013
1180 cm^{-1}	$\nu(\text{C-N})$	CP-013
1147 cm^{-1}	$\nu(\text{C-N})$	CP-013

Table 12. Analyzing and contrasting FTIR peaks in sample CP-020 with those of 2-methylimidazole.

Sample	$\nu(\text{C-N})_1$	$\nu(\text{C-N})_2$	$\nu(\text{C-N})_3$
2-MI	1302 cm^{-1}	1154 cm^{-1}	1113 cm^{-1}
CP-020	1310 cm^{-1}	1180 cm^{-1}	1147 cm^{-1}
Δk	8 cm^{-1}	26 cm^{-1}	34 cm^{-1}

These findings illustrate the coordination environment within CP-020, confirming the presence of both CA and 2-MI ligands. The data underscores the impact of synthesis conditions, such as pH and stoichiometry, on the coordination behavior and structural properties of the resulting CPs.

4.1.5 Crystallographic Analysis of Sample CP-020 & CP-028

Unidentified samples were further analyzed using crystallographic results (**Figure 27**). Both samples exhibited similar crystallographic peaks with minor intensity variations, particularly at 7.28, which was more pronounced in CP-020 than in CP-028.

Furthermore, the indexing results for the powder diffraction patterns of CP-020 and CP-028 reveal that both samples crystallize within the monoclinic system, as detailed in **Table 13**. They belong

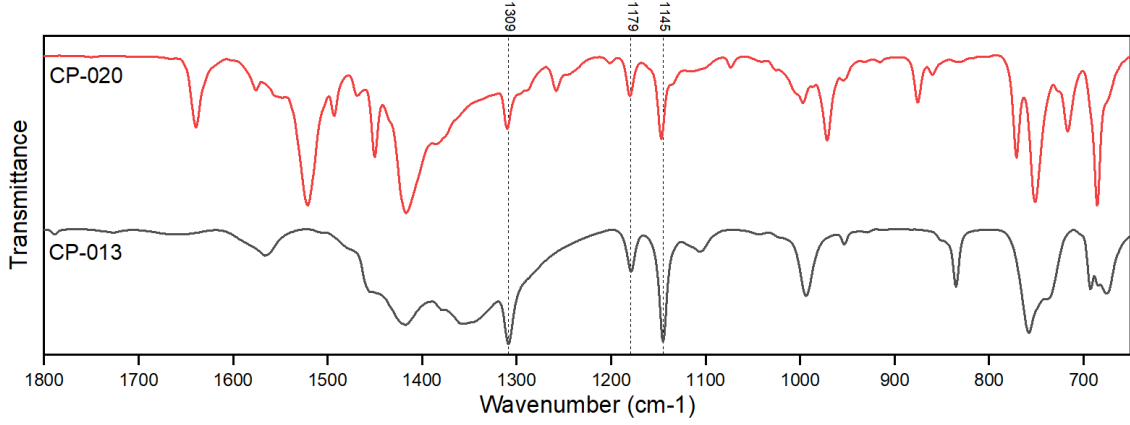


Figure 26. Fourier transform infrared spectroscopy of samples CP-20 (red) and CP-013 (black), showing similar peaks at 1309, 1179, and 1145 cm^{-1} .

to different non-centrosymmetric space groups. CP-020 is indexed in the $C2$ space group, while CP-028 is indexed in the $P2_1$ space group. This distinction in space groups is crucial as it influences the symmetry and potential physical properties of the materials, particularly their piezoelectric characteristics.

For CP-020, the initial lattice indexing provided the parameters: a , b , c , and β with the unit cell volume (V) detailed in **Table 13**. The quality of this indexing, indicated by FoM , suggests reliable results despite the presence of one spurious reflection line. The Le Bail refinement, as shown in **Table 14**, adjusted the lattice parameters to more precise values and offered additional statistical indicators such as χ^2 , goodness of fit (GoF), weighted profile R-factor (R_{wp}), and profile R-factor (R_p), confirming a reasonably good fit between the observed and calculated patterns.

For CP-028, the initial lattice parameters and V are listed in **Table 13**, demonstrating high-quality indexing despite one spurious reflection line. The Le Bail refinement results, detailed in **Table 14**, provided more accurate lattice parameters and high statistical metrics, indicating a high degree of accuracy and reliability in the refined lattice parameters.

Table 13. Initial lattice indexing parameters and space groups for CP-020 and CP-028.

Parameter	CP-020	CP-028
Space Group	$C2$	$P2_1$
a (\AA)	4.68	4.87
b (\AA)	10.10	10.06
c (\AA)	13.88	13.90
β ($^\circ$)	92.14	91.51
V (\AA^3)	1304.00	680.20
FoM	95.50	331.60

Table 14. Le Bail refinement parameters for CP-020 and CP-028.

Parameter	CP-020	CP-028
a (\AA)	4.56	4.64
b (\AA)	19.67	9.66
c (\AA)	13.58	13.29
β ($^\circ$)	92.55	90.71
χ^2	2.70×10^5	1.07×10^5
GoF	1.28×10^3	6.94×10^2
R_{wp}	0.25	0.21
R_p	0.17	0.18

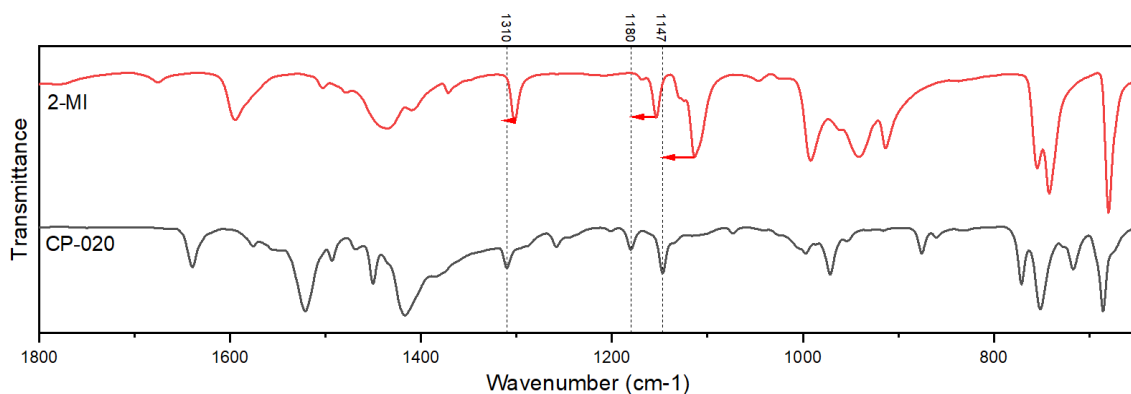


Figure 28. Fourier transform infrared spectroscopy of 2-methylimidazole (red) and sample CP-020 (black), showing similar peaks at 1310, 1180, and 1147 cm^{-1} , but displaced to the right (lower wavenumber values).

The non-centrosymmetric nature of the $C2$ and $P2_1$ space groups is particularly significant as it indicates that both CP-020 and CP-028 exhibit piezoelectric properties. Non-centrosymmetric structures lack a center of symmetry, which is a prerequisite for piezoelectricity. The monoclinic crystalline systems with their respective non-centrosymmetric space groups and refined lattice parameters provide a solid foundation for further structural and functional studies of these materials. The FoM, along with other statistical indicators from the Le Bail refinement, underscore the high quality and reliability of the indexed data, paving the way for potential applications and deeper insights into the material properties, including their piezoelectric capabilities.

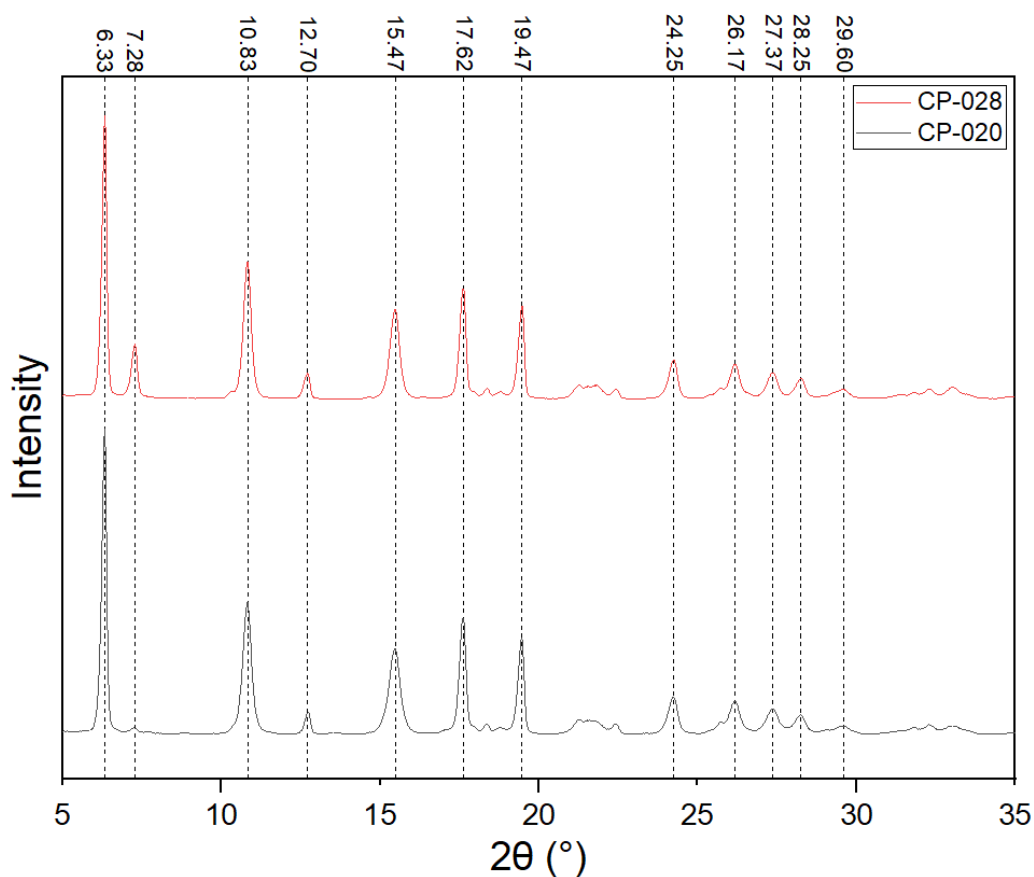


Figure 27. X-ray diffraction pattern of samples CP-013 (red) and CP-012 (black), showing similar peaks, with a change in intensity for peak at 7.28 2θ .

4.2 Composite Formation

4.2.1 Evaluation of Piezoelectric Measurement System

Figure 30 presents the piezoelectric response of a PZT sample under varying force levels, specifically at 11, 23, 42, and 60 N. Each graph plots the charge in microcoulombs (μC) as a function of time in seconds (s), offering a detailed insight into the dynamic behavior of the sample when subjected to mechanical stress. The investigation of these responses is crucial for understanding the efficiency and reliability of the piezoelectric coefficient measurement system. Given that PZT has been extensively studied, there are numerous piezoelectric coefficients available for reference to compare with the values obtained using this system.

At a force level of 11 N, the initial application of force results in a significant negative charge, peaking at $-1535 \mu\text{C}$. This negative peak indicates the immediate generation of a negative charge within the PZT sample due to the compressive stress applied. The subsequent neutralization phase, where the charge returns to zero, reflects the dissipation of the induced charge. After 2 seconds, when the force is removed, there is a sharp rise in charge, reaching a positive peak of $599 \mu\text{C}$. This sudden shift from negative to positive charge is characteristic of the piezoelectric effect, where the removal of the mechanical load results in an opposite electrical response. The total charge change (ΔQ) is calculated to be $2135 \mu\text{C}$.

For the 23 N force application, a similar pattern is observed. The initial negative peak reaches $-1794 \mu\text{C}$, followed by a neutralization phase. Upon removal of the force, the charge rapidly increases to a positive peak of $736 \mu\text{C}$. The ΔQ in this case is $2530 \mu\text{C}$, demonstrating a higher piezoelectric response compared to the 11 N force level. This increased charge difference

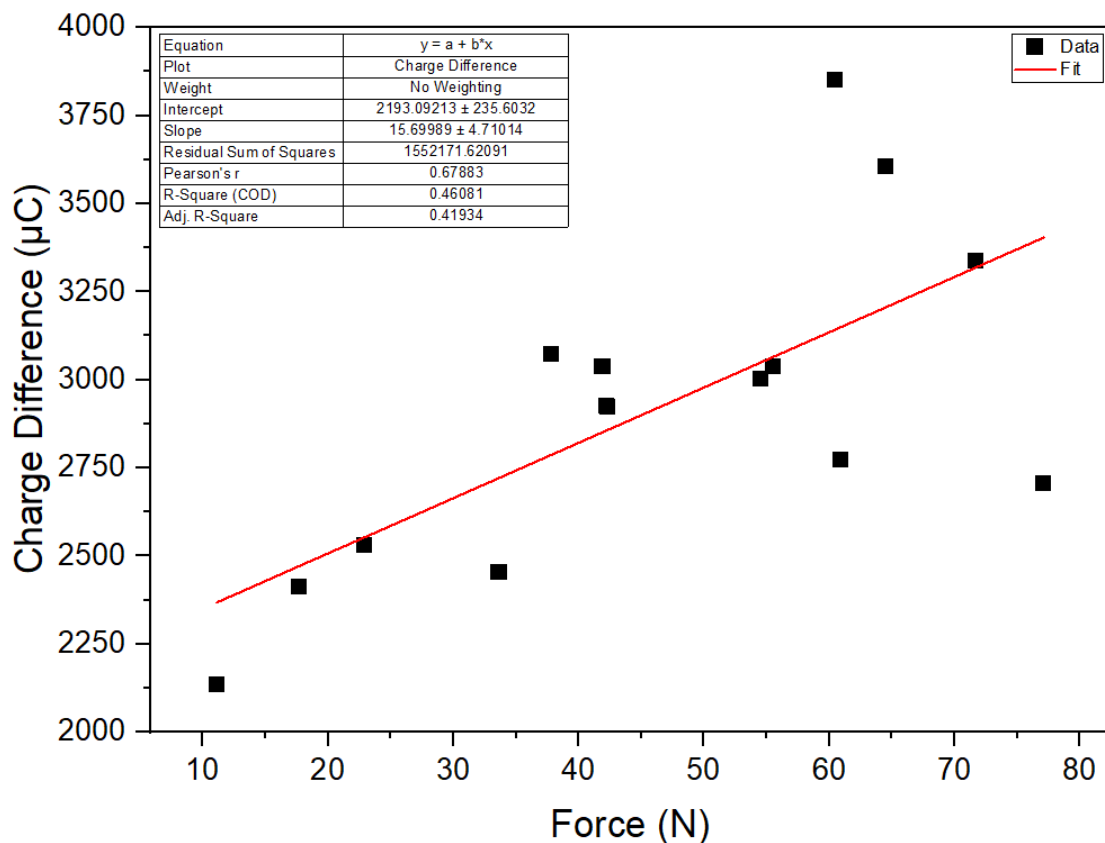


Figure 29. The electric charge difference from multiple tests under various forces is plotted, with a linear regression fitted to assess the linearity of the piezoelectric reference material (PZT).

highlights the material's capacity to generate greater electrical responses under higher mechanical stresses, confirming the direct proportionality between applied force and induced charge.

At 42 N, the piezoelectric response becomes even more pronounced. The negative charge peak is observed at $-1989 \mu\text{C}$, and the subsequent positive peak upon force removal reaches $1048 \mu\text{C}$. The ΔQ here is $3038 \mu\text{C}$. The increasing force continues to elicit a stronger piezoelectric response, illustrating the efficiency of the PZT material in converting mechanical stress into electrical energy.

When subjected to the maximum force level of 60 N, the PZT sample exhibits the highest piezoelectric response among the tested levels. The initial negative peak is $-2510 \mu\text{C}$, and the positive peak upon force removal is $1341 \mu\text{C}$. The ΔQ is $3851 \mu\text{C}$, reflecting a substantial piezoelectric effect. The progressively increasing charge differences with higher forces illustrate the material's robust performance in generating electrical responses to mechanical inputs.

The relationship between the applied force and the generated charge is evidently linear, as demonstrated by the progressively increasing charge differences with higher forces. This linearity is a key characteristic of piezoelectric materials and is crucial for their predictable and reliable performance in real-world applications. This trend is further corroborated by additional data points at more force levels shown in **Figure 29**, which clearly indicate a linear relationship between force and charge difference.

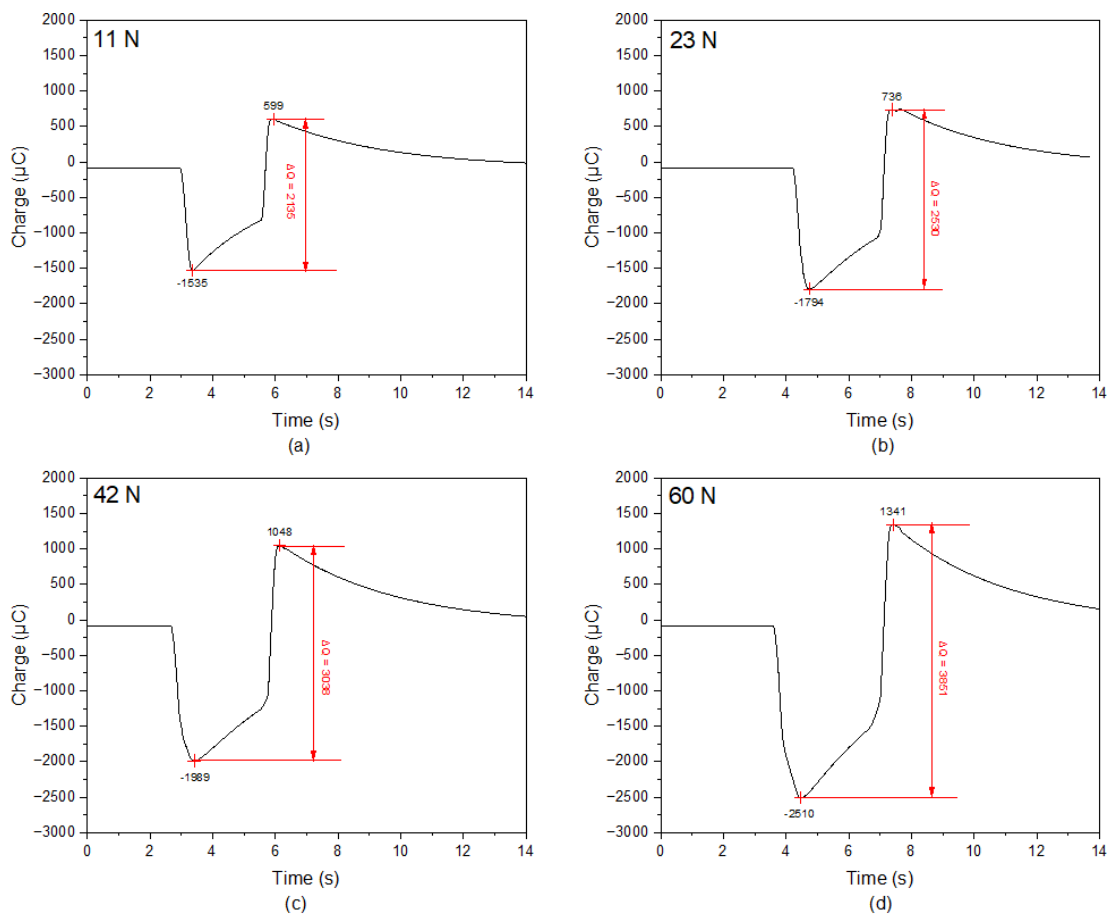


Figure 30. Electric charge change measured for the piezoelectric reference element PZT under different applied forces: 11, 23, 42, and 60N. The data shows an increase in charge difference between the upper and lower peak with higher applied forces. The charge difference is indicated by red arrows; larger arrows denote greater changes. The corresponding value changes are also shown in red.

The piezoelectric charge coefficient (d) can be determined from the linear relationship between charge and force depicted in **Figure 29**, as follows:

$$d = \left(\frac{\partial D}{\partial \sigma} \right)_E \quad (2)$$

where, D represents the electric displacement, σ represents the applied stress and E is constant the electric field strength³³. Additionally, **Equation 2** can be simplified as follows:

$$d = \frac{\Delta Q}{\Delta F} \quad (3)$$

where ΔQ is the change in electric charge and ΔF is the change in applied force.

Given that the slope of this linear relationship has already been calculated during the linearization of the data points in **Figure 29**, it represents the piezoelectric charge coefficient for this material, the resulting coefficient being $15.70 \mu\text{CN}^{-1}$.

However, it is important to note that the piezoelectric coefficients obtained with this system, is significantly higher than those reported in the literature for PZT, which typically range between 33 to 750 pCN^{-1} (**Table 2**). These discrepancies, about three orders of magnitude larger, can likely

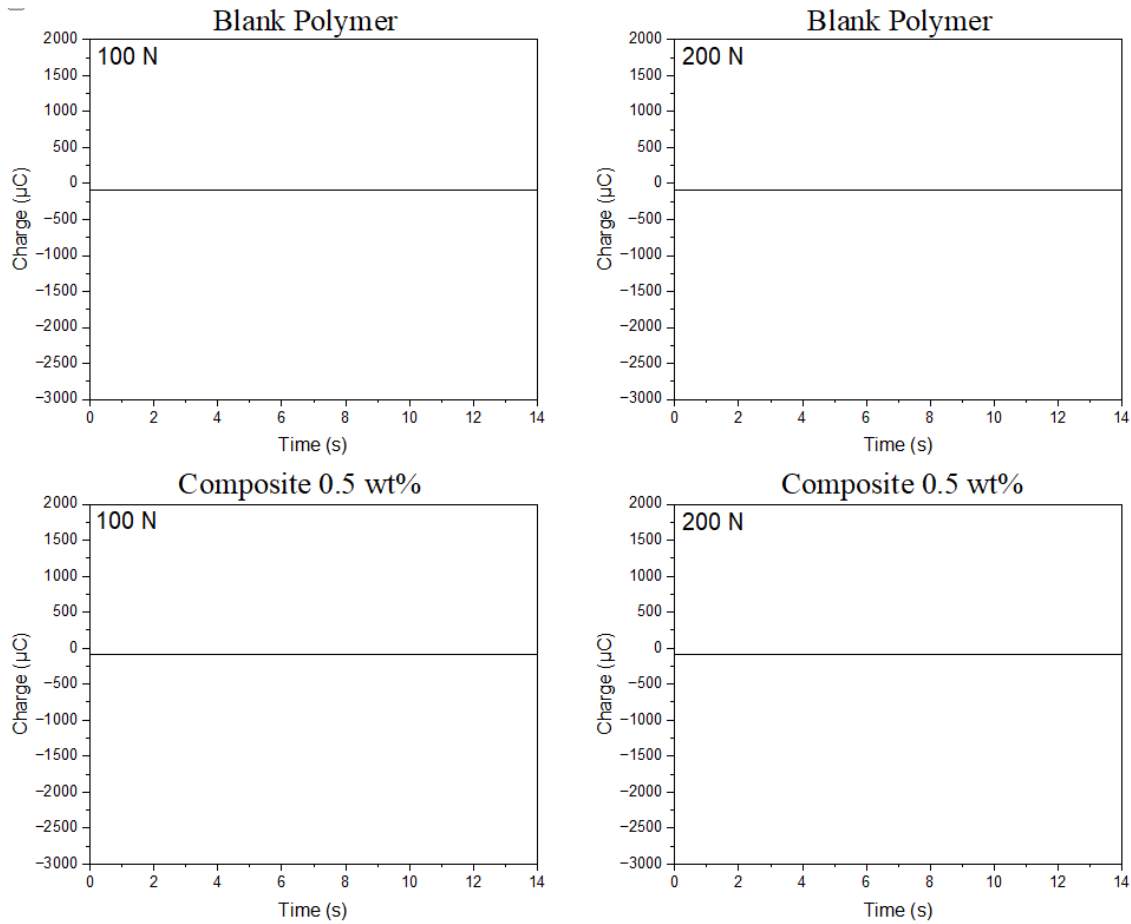


Figure 31. Electric charge change measured for the blank polymer (top) under different applied forces: 100 and 200 N. The data shows no change in electric charge regardless of the applied force. Additionally, the charge change measured for the composite material (bottom) indicates no change in electric charge regardless of the applied force.

be attributed to the amplification factor of the Op-Amp used in the measurement system. If we assume that the amplification factor of the Op-Amp is approximately three orders of magnitude, then the highest piezoelectric coefficient would be 15.70 pC/N , falling behind the reported literature values. This assumption emphasizes the need for careful calibration and consideration of the amplification effects in piezoelectric measurements.

The data obtained from these experiments provide valuable insights into the operational limits and capabilities of the piezoelectric measurement system, underscoring its effectiveness in accurately measuring the piezoelectric coefficients of materials.

4.2.2 Piezoelectric Property Measurement of Composite Samples

Figure 31 presents the piezoelectric response of both a blank polymer and a composite containing 0.5 wt.% of a coordination polymer embedded inside. Each graph plots the charge as a function of time under different force levels: 100 and 200 N. The goal of this experiment was to evaluate the piezoelectric properties of these materials and compare them to those observed in the PZT sample. However, the results indicate that neither the blank polymer nor the composite exhibit any noticeable piezoelectric effect.

In the top two graphs, the blank polymer is subjected to forces of 100 and 200 N. Despite the substantial forces applied, the charge remains constant at around $0 \text{ }\mu\text{C}$ throughout the duration of the tests. This lack of charge generation suggests that the blank polymer does not possess piezoelectric properties, as it fails to convert mechanical stress into electrical charge.

According to literature, PLA can exhibit piezoelectric properties when certain treatments, such as poling, are applied. Poling involves applying strong electric fields to align the dipoles within the material, thus making it piezoelectric. Additionally, the piezoelectric response of PLA depends on its enantiomeric composition. PLA has two enantiomers, PLLA and PDLA, with only PLLA demonstrating piezoelectric properties. In this case, the lack of piezoelectric response can be attributed to the absence of poling treatment and the use of a mix of both enantiomers instead of pure PLLA.

Similarly, the bottom two graphs display the piezoelectric response of the composite containing 0.5 wt.% of the coordination polymer under the same force levels. Like the blank polymer, the composite shows no change in charge, maintaining a steady $0 \text{ }\mu\text{C}$ regardless of the applied force. This result indicates that the inclusion of 0.5 wt.% coordination polymer is insufficient to impart any measurable piezoelectric properties to the composite material.

The experiments were conducted across different force levels to thoroughly investigate the piezoelectric potential of both materials. However, since neither the blank polymer nor the composite exhibited any charge generation, only the results for the highest force levels (100 and 200 N) are shown in **Figure 31**. These force levels are significantly higher than those applied to the PZT sample, yet the materials still did not produce any piezoelectric response.

The absence of any detectable piezoelectric effect in both the blank polymer and the composite, even under high forces, highlights a stark contrast to the PZT sample's behavior. The PZT sample demonstrated a clear and measurable piezoelectric response at much lower forces, emphasizing its superior piezoelectric properties. The results suggest that further modifications or higher concentrations of the coordination polymer may be necessary to induce piezoelectricity in the composite material.

Chapter 5: Conclusion

5.1 Findings Summary

In this thesis, extensive research was conducted on the synthesis, characterization, and evaluation of piezoelectric properties in coordination polymers and their composites. The study focused on designing coordination polymers using zinc nitrate as the metal ion source, 2-MI for its dual coordination ability, and CA as a bridging ligand. Ethanol was employed as the solvent due to its ability to dissolve CA and 2-MI under mild conditions, facilitating a one-pot solution method for synthesis. pH control using NaOH was crucial for regulating ligand coordination during the process.

Characterization techniques included powder XRD for crystal phase identification and FTIR for analyzing functional groups. The synthesized coordination polymers were then incorporated into PLA composites via solution casting with THF as the solvent. The resulting composites were subjected to comprehensive piezoelectric property testing using a NI MyDAQ data acquisition system and custom charge amplifier, alongside a universal testing machine for mechanical load application.

Key findings indicated that the coordination polymers exhibited diverse crystallographic structures dependent on synthesis methods and pH conditions. While basic pH environments favored effective coordination of 2-MI with zinc, neutral to slightly acidic conditions favoring the coordination of both ligands, influencing crystalline phase outcomes. FTIR analysis confirmed the bidentate coordination of CA and the presence of 2-MI within the samples CP-020 and CP-028.

Additionally, the study critically assessed a piezoelectric measurement system using a PZT sample. The system demonstrated a linear relationship between applied force and generated charge, with a recorded piezoelectric coefficient of $15.70 \mu\text{CN}^{-1}$. Discrepancies between these measurements and typical literature values were attributed to the amplification factor of the Op-Amp used in the system, emphasizing the importance of calibration in accurate piezoelectric measurements.

In evaluating the piezoelectric properties, the composites containing 0.5 wt.% of the coordination polymers showed no measurable piezoelectric effect under applied forces of 100 and 200 N. This suggested that the concentration of the coordination polymer was insufficient to induce significant piezoelectric behavior in the composite material.

Overall, this thesis provides valuable insights into the synthesis, characterization, and piezoelectric evaluation of coordination polymers and their composites, highlighting avenues for future research and applications in materials science and engineering.

5.2 Limitations

Despite these valuable findings, several limitations were identified. First, the concentration of coordination polymers in the composite materials may have been too low to observe substantial piezoelectric effects, limiting the conclusions about their effectiveness in composite applications. Second, the use of one-pot synthesis method, while practical, may have constrained the range of coordination polymers formed, potentially reducing their piezoelectric properties. Additionally, the piezoelectric measurement system's reliance on a custom-built charge amplifier may have introduced uncertainties due to amplification factors, underscoring the need for precise calibration and verification of the measurement setup. Future research should address these limitations by

exploring alternative synthesis methods, higher polymer concentrations, and optimized piezoelectric measurement techniques.

5.3 Future Research Directions

To advance the understanding and application of piezoelectric coordination polymers and composites, several avenues for future research are proposed. Firstly, synthesizing highly crystalline samples and characterizing them using single crystal X-ray diffraction will provide precise unit cell parameters. This approach aims to confirm the absence of a center of symmetry, a prerequisite for intrinsic piezoelectricity. By obtaining accurate structural data, the piezoelectric potential of these materials can be further elucidated with confidence.

Another critical direction involves exploring the piezoelectric properties of films composed solely of coordination polymers. This investigation will help validate and understand the intrinsic piezoelectric capabilities of the coordination polymers themselves, independent of any polymeric matrix. Furthermore, by systematically varying the concentration of the coordination polymer in composites, particularly increasing it beyond 0.5 wt.%, the performance in terms of piezoelectricity can be thoroughly evaluated. This exploration aims to identify optimal compositions that maximize piezoelectric response while maintaining structural integrity.

Additionally, experimenting with different polymeric matrices beyond PLA could uncover potential influences on the piezoelectric properties of the composites. Comparative studies involving various matrices will provide insights into how matrix materials interact with embedded coordination polymers, potentially affecting overall piezoelectric performance and mechanical properties such as Young's modulus, tensile stress, and strain.

Moreover, a broader exploration into synthesizing diverse coordination polymers using alternative ligands and metal ions is proposed. By varying these components, the structure-property relationships governing piezoelectric and mechanical behaviors can be systematically investigated. This comparative approach will help identify optimal combinations that exhibit superior piezoelectric properties suitable for practical applications.

Each of these research directions aims to deepen the understanding of piezoelectric coordination polymers and their composites, paving the way for enhanced materials design and application in fields requiring high piezoelectric coefficients. These advancements are crucial for achieving better efficiency and flexibility, specifically in applications such as robotic musculoskeletal systems.

References

- (1) Biddiss, E.; Chau, T. Dielectric Elastomers as Actuators for Upper Limb Prosthetics: Challenges and Opportunities. *Med. Eng. Phys.* **2008**, *30* (4), 403–418. <https://doi.org/10.1016/j.medengphy.2007.05.011>.
- (2) Zhang, J.; Sheng, J.; O'Neill, C. T.; Walsh, C. J.; Wood, R. J.; Ryu, J.-H.; Desai, J. P.; Yip, M. C. Robotic Artificial Muscles: Current Progress and Future Perspectives. *IEEE Trans. Robot.* **2019**, *35* (3), 761–781. <https://doi.org/10.1109/TRO.2019.2894371>.
- (3) Mirvakili, S. M.; Hunter, I. W. Artificial Muscles: Mechanisms, Applications, and Challenges. *Adv. Mater.* **2018**, *30* (6), 1704407. <https://doi.org/10.1002/adma.201704407>.
- (4) Copaci, D.-S.; Blanco, D.; Martin-Clemente, A.; Moreno, L. Flexible Shape Memory Alloy Actuators for Soft Robotics: Modelling and Control. *Int. J. Adv. Robot. Syst.* **2020**, *17* (1), 172988141988674. <https://doi.org/10.1177/1729881419886747>.
- (5) Antonelli, M. G.; Beomonte Zobel, P.; Durante, F.; Raparelli, T. Additive Manufacturing Applications on Flexible Actuators for Active Orthoses and Medical Devices. *J. Healthc. Eng.* **2019**, *2019*, 1–11. <https://doi.org/10.1155/2019/5659801>.
- (6) Mohd Ghazali, F. A.; Hasan, M. N.; Rehman, T.; Nafea, M.; Mohamed Ali, M. S.; Takahata, K. MEMS Actuators for Biomedical Applications: A Review. *J. Micromechanics Microengineering* **2020**, *30* (7), 073001. <https://doi.org/10.1088/1361-6439/ab8832>.
- (7) Novelli, G. L.; Vargas, G. G.; Andrade, R. M. Dielectric Elastomer Actuators as Artificial Muscles for Wearable Robots. *J. Intell. Mater. Syst. Struct.* **2022**, 1045389X2211285. <https://doi.org/10.1177/1045389X221128567>.
- (8) Shi, M.; Yeatman, E. M. A Comparative Review of Artificial Muscles for Microsystem Applications. *Microsyst. Nanoeng.* **2021**, *7* (1), 95. <https://doi.org/10.1038/s41378-021-00323-5>.
- (9) Bauer, S.; Bauer, F. Piezoelectric Polymers and Their Applications. In *Piezoelectricity*; Hull, R., Osgood, R. M., Parisi, J., Warlimont, H., Series Eds.; Springer Series in Materials Science; Springer Berlin Heidelberg: Berlin, Heidelberg, 2008; Vol. 114, pp 157–177. https://doi.org/10.1007/978-3-540-68683-5_6.
- (10) Zhang, T.-Y.; Zhao, M.; Tong, P. Fracture of Piezoelectric Ceramics. In *Advances in Applied Mechanics*; Elsevier, 2002; Vol. 38, pp 147–289. [https://doi.org/10.1016/S0065-2156\(02\)80104-1](https://doi.org/10.1016/S0065-2156(02)80104-1).
- (11) Rupitsch, S. J. Piezoelectricity; 2019; pp 43–81. https://doi.org/10.1007/978-3-662-57534-5_3.
- (12) Smith, M.; Kar-Narayan, S. Piezoelectric Polymers: Theory, Challenges and Opportunities. *Int. Mater. Rev.* **2022**, *67* (1), 65–88. <https://doi.org/10.1080/09506608.2021.1915935>.
- (13) Li, K.; Qin, Y.; Li, Z.-G.; Guo, T.-M.; An, L.-C.; Li, W.; Li, N.; Bu, X.-H. Elastic Properties Related Energy Conversions of Coordination Polymers and Metal–Organic Frameworks. *Coord. Chem. Rev.* **2022**, *470*, 214692. <https://doi.org/10.1016/j.ccr.2022.214692>.
- (14) Mohd Jani, J.; Leary, M.; Subic, A.; Gibson, M. A. A Review of Shape Memory Alloy Research, Applications and Opportunities. *Mater. Des. 1980-2015* **2014**, *56*, 1078–1113. <https://doi.org/10.1016/j.matdes.2013.11.084>.
- (15) Damjanovic, D. A Morphotropic Phase Boundary System Based on Polarization Rotation and Polarization Extension. *Appl. Phys. Lett.* **2010**, *97* (6), 062906. <https://doi.org/10.1063/1.3479479>.
- (16) Rödel, J.; Webber, K. G.; Dittmer, R.; Jo, W.; Kimura, M.; Damjanovic, D. Transferring Lead-Free Piezoelectric Ceramics into Application. *J. Eur. Ceram. Soc.* **2015**, *35* (6), 1659–1681. <https://doi.org/10.1016/j.jeurceramsoc.2014.12.013>.
- (17) Zhang, Y.; Li, H.-L.; Zhou, J.-J.; Liu, H.; Fang, J.-Z. Enhanced Piezoelectric Coefficient and Mechanical Performance of Pb(Ni_{1/3}Nb_{2/3})O₃–PbZrO₃–PbTiO₃ Ferroelectric Ceramics by Pb(Mn_{1/3}Sb_{2/3})O₃ Modification. *Ceram. Int.* **2015**, *41* (10), 14101–14107. <https://doi.org/10.1016/j.ceramint.2015.07.030>.

- (18) Zhan, K.; Zheng, X. J.; Peng, J. F.; Zhu, Y. K.; Cheng, H. B. Effects of Potassium Content on the Electrical and Mechanical Properties of $(\text{Na}_{1-x}\text{K}_x)_0.5\text{Bi}_0.5\text{TiO}_3$ Thin Films. *Ceram. Int.* **2015**, *41* (3), 3474–3480. <https://doi.org/10.1016/j.ceramint.2014.10.173>.
- (19) Habib, M.; Lantgios, I.; Hornbostel, K. A Review of Ceramic, Polymer and Composite Piezoelectric Materials. *J. Phys. Appl. Phys.* **2022**, *55* (42), 423002. <https://doi.org/10.1088/1361-6463/ac8687>.
- (20) Salazar, R.; Serrano, M.; Abdelkefi, A. Fatigue in Piezoelectric Ceramic Vibrational Energy Harvesting: A Review. *Appl. Energy* **2020**, *270*, 115161. <https://doi.org/10.1016/j.apenergy.2020.115161>.
- (21) Mishra, A. K.; Janani Kavi Priya, V. S.; Pradeep, K.; Sai Vaishnav, J.; Kabhilesh, G. Smart Materials for Ultrasonic Piezoelectric Composite Transducer: A Short Review. *Mater. Today Proc.* **2022**, *62*, 2064–2069. <https://doi.org/10.1016/j.matpr.2022.02.514>.
- (22) Nazeer, H.; Nguyen, M. D.; Sukas, O. S.; Rijnders, G.; Abelmann, L.; Elwenspoek, M. C. Compositional Dependence of the Young's Modulus and Piezoelectric Coefficient of (110)-Oriented Pulsed Laser Deposited PZT Thin Films. *J. Microelectromechanical Syst.* **2015**, *24* (1), 166–173. <https://doi.org/10.1109/JMEMS.2014.2323476>.
- (23) Tou, T.; Hamaguti, Y.; Maida, Y.; Yamamori, H.; Takahashi, K.; Terashima, Y. Properties of $(\text{Bi}_{0.5}\text{Na}_{0.5})\text{TiO}_3 - \text{BaTiO}_3 - (\text{Bi}_{0.5}\text{Na}_{0.5})(\text{Mn}_{1/3}\text{Nb}_{2/3})\text{O}_3$ Lead-Free Piezoelectric Ceramics and Its Application to Ultrasonic Cleaner. *Jpn. J. Appl. Phys.* **2009**, *48* (7), 07GM03. <https://doi.org/10.1143/JJAP.48.07GM03>.
- (24) Banerjee, S.; Du, W.; Sundar, U.; Cook-Chennault, K. A. Piezoelectric and Dielectric Characterization of Mwcnt-Based Nanocomposite Flexible Films. *Journal of Nanomaterials*, 2018, 2018. <https://doi.org/10.1155/2018/6939621>.
- (25) Wang, W.; Jiang, Y.; Thomas, P. J. Structural Design and Physical Mechanism of Axial and Radial Sandwich Resonators with Piezoelectric Ceramics: A Review. *Sensors* **2021**, *21* (4), 1112. <https://doi.org/10.3390/s21041112>.
- (26) Thakur, V. N.; Singh, B. P.; Yadav, S.; Kumar, A. Giant Pressure Sensitivity in Piezo/Ferro-Electric Ceramics. *RSC Adv.* **2020**, *10* (15), 9140–9145. <https://doi.org/10.1039/D0RA00484G>.
- (27) Tan, Z.; Xie, S.; Jiang, L.; Xing, J.; Chen, Y.; Zhu, J.; Xiao, D.; Wang, Q. Oxygen Octahedron Tilting, Electrical Properties and Mechanical Behaviors in Alkali Niobate-Based Lead-Free Piezoelectric Ceramics. *J. Materiomics* **2019**, *5* (3), 372–384. <https://doi.org/10.1016/j.jmat.2019.02.001>.
- (28) Pandey, R.; Sb, G.; Grover, S.; Singh, S. K.; Kadam, A.; Ogale, S.; Waghmare, U. V.; Rao, V. R.; Kabra, D. Microscopic Origin of Piezoelectricity in Lead-Free Halide Perovskite: Application in Nanogenerator Design. *ACS Energy Lett.* **2019**, *4* (5), 1004–1011. <https://doi.org/10.1021/acseenergylett.9b00323>.
- (29) Hayati, R.; Fayazi, M.; Diargar, H.; Kaveh, M.; Tayebi, L. Electrical and Mechanical Properties of BZT – x BCT Lead-free Piezoceramics. *Int. J. Appl. Ceram. Technol.* **2020**, *17* (4), 1891–1898. <https://doi.org/10.1111/ijac.13494>.
- (30) Chen, K.-H.; Cheng, C.-M.; Chen, Y.-J.; Chen, M.-L. Lead-Free Piezoelectric Ceramic Micro-Pressure Thick Films. *Crystals* **2023**, *13* (2), 201. <https://doi.org/10.3390/cryst13020201>.
- (31) Chen, N.; Yao, W.; Liang, C.; Xiao, S.; Hao, J.; Xu, Z.; Chu, R. Phase Structure, Ferroelectric Properties, and Electric Field-Induced Large Strain in Lead-Free $0.99[(1-x)(\text{Bi}_{0.5}\text{Na}_{0.5})\text{TiO}_3 - x(\text{Bi}_{0.5}\text{K}_{0.5})\text{TiO}_3] - 0.01\text{Ta}$ Piezoelectric Ceramics. *Ceram. Int.* **2016**, *42* (8), 9660–9666. <https://doi.org/10.1016/j.ceramint.2016.03.053>.
- (32) Yusoff, N. H.; Osman, R. A. M.; Idris, M. S.; Muhsen, K. N. D. K.; Nor, N. I. M. Dielectric and Structural Analysis of Hexagonal and Tetragonal Phase BaTiO_3 ; Putrajaya, Malaysia, 2020; p 020038. <https://doi.org/10.1063/1.5142130>.
- (33) Smith, M.; Kar-Narayan, S. Piezoelectric Polymers: Theory, Challenges and Opportunities. *Int. Mater. Rev.* **2022**, *67* (1), 65–88. <https://doi.org/10.1080/09506608.2021.1915935>.
- (34) Kaczmarek, H.; Królikowski, B.; Klimiec, E.; Kowalonek, J. New Piezoelectric Composites Based on Isotactic Polypropylene Filled with Silicate. *J. Mater. Sci. Mater. Electron.* **2017**, *28* (9), 6435–6447. <https://doi.org/10.1007/s10854-016-6329-9>.

- (35) Zhang, X.; Wu, L.; Sessler, G. M. Energy Harvesting from Vibration with Cross-Linked Polypropylene Piezoelectrets. *AIP Adv.* **2015**, *5* (7), 077185. <https://doi.org/10.1063/1.4928039>.
- (36) Ma, X.; Zhukov, S.; Von Seggern, H.; Sessler, G. M.; Ben Dali, O.; Kupnik, M.; Dai, Y.; He, P.; Zhang, X. Biodegradable and Bioabsorbable Polylactic Acid Ferroelectrets with Prominent Piezoelectric Activity. *Adv. Electron. Mater.* **2023**, *9* (3), 2201070. <https://doi.org/10.1002/aelm.202201070>.
- (37) Dali, O. B.; Zhukov, S.; Hartman, C.; Von Seggern, H.; Sessler, G. M.; Kupnik, M. Biodegradable Additive Manufactured Ferroelectret as Mechanical Sensor. In *2021 IEEE Sensors*; IEEE: Sydney, Australia, 2021; pp 1–4. <https://doi.org/10.1109/SENSOR47087.2021.9639709>.
- (38) Wang, J.-J.; Hsu, T.-H.; Yeh, C.-N.; Tsai, J.-W.; Su, Y.-C. Piezoelectric Polydimethylsiloxane Films for MEMS Transducers. *J. Micromechanics Microengineering* **2012**, *22* (1), 015013. <https://doi.org/10.1088/0960-1317/22/1/015013>.
- (39) Wang, J. J.; Hsieh, J. M.; Tsai, R. W.; Su, Y. C. Piezoelectric PDMS Films for Power MEMS. In *2011 16th International Solid-State Sensors, Actuators and Microsystems Conference*; IEEE: Beijing, China, 2011; pp 2622–2625. <https://doi.org/10.1109/TRANSDUCERS.2011.5969868>.
- (40) Lam, T.-N.; Ma, C.-Y.; Hsiao, P.-H.; Ko, W.-C.; Huang, Y.-J.; Lee, S.-Y.; Jain, J.; Huang, E.-W. Tunable Mechanical and Electrical Properties of Coaxial Electrospun Composite Nanofibers of P(VDF-TrFE) and P(VDF-TrFE-CTFE). *Int. J. Mol. Sci.* **2021**, *22* (9), 4639. <https://doi.org/10.3390/ijms22094639>.
- (41) Su, Y. P.; Sim, L. N.; Coster, H. G. L.; Chong, T. H. Incorporation of Barium Titanate Nanoparticles in Piezoelectric PVDF Membrane. *J. Membr. Sci.* **2021**, *640*, 119861. <https://doi.org/10.1016/j.memsci.2021.119861>.
- (42) Wu, C. M.; Chou, M. H. Polymorphism, Piezoelectricity and Sound Absorption of Electrospun PVDF Membranes with and without Carbon Nanotubes. *Compos. Sci. Technol.* **2016**, *127*, 127–133. <https://doi.org/10.1016/j.compscitech.2016.03.001>.
- (43) Fu, R.; Tu, L.; Zhou, Y.; Fan, L.; Zhang, F.; Wang, Z.; Xing, J.; Chen, D.; Deng, C.; Tan, G.; Yu, P.; Zhou, L.; Ning, C. A Tough and Self-Powered Hydrogel for Artificial Skin. *Chem. Mater.* **2019**, *31* (23), 9850–9860. <https://doi.org/10.1021/acs.chemmater.9b04041>.
- (44) Prokhorov, E.; Luna-Bárcenas, G.; Yáñez Limón, J. M.; Gómez Sánchez, A.; Kovalenko, Y. Chitosan-ZnO Nanocomposites Assessed by Dielectric, Mechanical, and Piezoelectric Properties. *Polymers* **2020**, *12* (9), 1991. <https://doi.org/10.3390/polym12091991>.
- (45) Racles, C.; Dascalu, M.; Bele, A.; Tiron, V.; Asandulesa, M.; Tugui, C.; Vasiliu, A.-L.; Cazacu, M. All-Silicone Elastic Composites with Counter-Intuitive Piezoelectric Response, Designed for Electromechanical Applications. *J. Mater. Chem. C* **2017**, *5* (28), 6997–7010. <https://doi.org/10.1039/C7TC02201H>.
- (46) Li, J.; Zhu, Z.; Fang, L.; Guo, S.; Erturun, U.; Zhu, Z.; West, J. E.; Ghosh, S.; Kang, S. H. Analytical, Numerical, and Experimental Studies of Viscoelastic Effects on the Performance of Soft Piezoelectric Nanocomposites. *Nanoscale* **2017**, *9* (37), 14215–14228. <https://doi.org/10.1039/C7NR05163H>.
- (47) Hsu, T.-H.; Yeh, C.-N.; Su, Y.-C. Piezoelectric PDMS Electrets for MEMS Transducers. In *2010 IEEE 23rd International Conference on Micro Electro Mechanical Systems (MEMS)*; IEEE: Wanchai, Hong Kong, China, 2010; pp 388–391. <https://doi.org/10.1109/MEMSYS.2010.5442485>.
- (48) Racles, C.; Asandulesa, M.; Tiron, V.; Tugui, C.; Vornicu, N.; Ciubotaru, B.-I.; Mičušík, M.; Omastová, M.; Vasiliu, A.-L.; Ciomaga, C. Elastic Composites with PDMS Matrix and Polysulfone-Supported Silver Nanoparticles as Filler. *Polymer* **2021**, *217*, 123480. <https://doi.org/10.1016/j.polymer.2021.123480>.
- (49) Wang, A.; Hu, M.; Zhou, L.; Qiang, X. Self-Powered Wearable Pressure Sensors with Enhanced Piezoelectric Properties of Aligned P(VDF-TrFE)/MWCNT Composites for Monitoring Human Physiological and Muscle Motion Signs. *Nanomaterials* **2018**, *8* (12), 1021. <https://doi.org/10.3390/nano8121021>.

- (50) Haghiashtiani, G.; Greminger, M. A. Fabrication, Polarization, and Characterization of PVDF Matrix Composites for Integrated Structural Load Sensing. *Smart Mater. Struct.* **2015**, *24* (4), 045038. <https://doi.org/10.1088/0964-1726/24/4/045038>.
- (51) Li, K.; Qin, Y.; Li, Z.-G.; Guo, T.-M.; An, L.-C.; Li, W.; Li, N.; Bu, X.-H. Elastic Properties Related Energy Conversions of Coordination Polymers and Metal–Organic Frameworks. *Coord. Chem. Rev.* **2022**, *470*, 214692. <https://doi.org/10.1016/j.ccr.2022.214692>.
- (52) Yang, P.; He, X.; Li, M.-X.; Ye, Q.; Ge, J.-Z.; Wang, Z.-X.; Zhu, S.-R.; Shao, M.; Cai, H.-L. The First Homochiral Coordination Polymer with Temperature-Independent Piezoelectric and Dielectric Properties. *J. Mater. Chem.* **2012**, *22* (6), 2398. <https://doi.org/10.1039/c2jm14961c>.
- (53) Prajesh, N.; Sharma, V. B.; Rajput, S. S.; Singh, C. K.; Dixit, P.; Praveenkumar, B.; Zaręba, J. K.; Kabra, D.; Ogale, S.; Boomishankar, R. Flexible Piezoelectric Nanogenerators Based on One-Dimensional Neutral Coordination Network Composites. *ACS Sustain. Chem. Eng.* **2022**, *10* (30), 9911–9920. <https://doi.org/10.1021/acssuschemeng.2c02296>.
- (54) Anton, S. R.; Erturk, A.; Inman, D. J. Bending Strength of Piezoelectric Ceramics and Single Crystals for Multifunctional Load-Bearing Applications. *IEEE Trans. Ultrason. Ferroelectr. Freq. Control* **2012**, *59* (6), 1085–1092. <https://doi.org/10.1109/TUFFC.2012.2299>.
- (55) Rupitsch, S. J. *Piezoelectric Sensors and Actuators: Fundamentals and Applications*; Topics in Mining, Metallurgy and Materials Engineering; Springer Berlin Heidelberg: Berlin, Heidelberg, 2019. <https://doi.org/10.1007/978-3-662-57534-5>.
- (56) Sherman, J. D.; Elloian, J.; Jadwiszczak, J.; Shepard, K. L. On the Temperature Dependence of the Piezoelectric Response of Prepoled Poly(Vinylidene Fluoride) Films. *ACS Appl. Polym. Mater.* **2020**, *2* (11), 5110–5120. <https://doi.org/10.1021/acsapm.0c00902>.
- (57) Chen, R.; Yao, J.; Gu, Q.; Smeets, S.; Baerlocher, C.; Gu, H.; Zhu, D.; Morris, W.; Yaghi, O. M.; Wang, H. A Two-Dimensional Zeolitic Imidazolate Framework with a Cushion-Shaped Cavity for CO₂ Adsorption. *Chem. Commun.* **2013**, *49* (82), 9500. <https://doi.org/10.1039/c3cc44342f>.
- (58) Fujie, K.; Ikeda, R.; Otsubo, K.; Yamada, T.; Kitagawa, H. Lithium Ion Diffusion in a Metal–Organic Framework Mediated by an Ionic Liquid. *Chem. Mater.* **2015**, *27* (21), 7355–7361. <https://doi.org/10.1021/acs.chemmater.5b02986>.
- (59) Demir, S.; Kantar, G. K.; Topcu, Y.; Li, Q. Solvothermal Synthesis and Characterization of Coordination Polymers of Cobalt(II) and Zinc(II) with Succinic Acid. *Transit. Met. Chem.* **2012**, *37* (3), 257–263. <https://doi.org/10.1007/s11243-012-9581-8>.
- (60) Zeleňák, V.; Čísařová, I.; Llewellyn, P. Diversity of Carboxylate Coordination in Two Novel Zinc(II) Cinnamate Complexes. *Inorg. Chem. Commun.* **2007**, *10* (1), 27–32. <https://doi.org/10.1016/j.inoche.2006.08.021>.
- (61) Motta, F. L.; Melo, B. A. G.; Santana, M. H. A. Deprotonation and Protonation of Humic Acids as a Strategy for the Technological Development of pH-Responsive Nanoparticles with Fungicidal Potential. *New Biotechnol.* **2016**, *33* (6), 773–780. <https://doi.org/10.1016/j.nbt.2016.07.003>.
- (62) Tong, M.-L.; Chen, X.-M. Synthesis of Coordination Compounds and Coordination Polymers. In *Modern Inorganic Synthetic Chemistry*; Elsevier, 2017; pp 189–217. <https://doi.org/10.1016/B978-0-444-63591-4.00008-2>.
- (63) Batten, S. R.; Neville, S. M.; Turner, D. R. *Coordination Polymers: Design, Analysis and Application*; Royal Society of Chemistry: Cambridge, UK, 2009.
- (64) Boultif, A.; Louër, D. Powder Pattern Indexing with the Dichotomy Method. *J. Appl. Crystallogr.* **2004**, *37* (5), 724–731. <https://doi.org/10.1107/S0021889804014876>.
- (65) De Wolff, P. M. A Simplified Criterion for the Reliability of a Powder Pattern Indexing. *J. Appl. Crystallogr.* **1968**, *1* (2), 108–113. <https://doi.org/10.1107/S002188986800508X>.
- (66) Le Bail, A. Whole Powder Pattern Decomposition Methods and Applications: A Retrospection. *Powder Diffr.* **2005**, *20* (4), 316–326. <https://doi.org/10.1154/1.2135315>.

- (67) Tsai, J.-W.; Wang, J.-J.; Su, Y.-C. Piezoelectric Rubber Films for Autonomous Physiological Monitoring Systems. *Sens. Actuators Phys.* **2014**, *215*, 176–183. <https://doi.org/10.1016/j.sna.2013.08.044>.
- (68) Hosomi, H.; Ohba, S.; Ito, Y. *Cis* -Diaquabis(*Trans* -Cinnamato- *O* , *O* ')Zinc(II). *Acta Crystallogr. C* **2000**, *56* (4), e123–e123. <https://doi.org/10.1107/S0108270100003358>.